ANALYTE EXCITATION AND IONIZATION

IN THE

ARGON INDUCTIVELY COUPLED PLASMA

by

BRENDA LEA CAUGHLIN

B.Sc. (Hons.), Queen's University, 1977

A THESIS SUBMITTED IN PARTIAL FULFILLMENT OF

THE REQUIREMENTS FOR THE DEGREE OF

DOCTOR OF PHILOSOPHY

in

THE FACULTY OF GRADUATE STUDIES

Department of Chemistry

We accept this thesis as conforming

to the required standard

THE UNIVERSITY OF BRITISH COLUMBIA

July 1986

In presenting this thesis in partial fulfilment of the requirements for an advanced degree at the University of British Columbia, I agree that the Library shall make it freely available for reference and study. I further agree that permission for extensive copying of this thesis for scholarly purposes may be granted by the head of my department or by his or her representatives. It is understood that copying or publication of this thesis for financial gain shall not be allowed without my written permission.

Department of CHEMISTRY

The University of British Columbia
1956 Main Mall
Vancouver, Canada
V6T 1Y3

Date August 14, 1986

Abstract

A new approach to evaluating departures from local thermal equilibrium (LTE) in the inductively coupled plasma (ICP) is described. Experimentally evaluated electron density (n_e) is used as the basis for an LTE framework.

Spatially resolved, radial electron density profiles were measured under a variety of plasma operating conditions. The variation of n_e with spatial position, aerosol flow rate, input power and presence of easily ionizable elements was determined. The measured n_e was used to calculate an LTE temperature, $T_{e,LTE}$. This temperature was higher than most spectroscopically measured temperatures in the plasma.

LTE ion-atom emission intensity ratios for Sr, Ca, Mg, Cd and Zn were calculated from n_e and $T_{e,LTE}$ and compared to experimental values. Ion-atom ratios were within an order of magnitude of LTE values and, in most cases, less than the LTE values. The infrathermal ion-atom ratios were interpreted as being due to an overpopulation of the atom levels relative to LTE populations.

Experimental degree of ionization was evaluated for a number of elements and compared to LTE values. Elements were underionized relative to LTE values. Degree of ionization and departure from LTE were correlated with ionization potential of the element. Elements with a high ionization potential had lower degrees of ionization and exhibited greater departures from LTE than elements of lower ionization potential.

The underionization and infrathermal ion-atom intensity ratios are attributed to overpopulation of atom levels. The

experimental observations and results of other plasma diagnostic studies are discussed in terms of a partial LTE (p-LTE) model for the ICP. The ion ground state and upper energy levels of atoms are in Saha equilibrium. Lower atomic levels are overpopulated with respect to these levels. The overpopulation of the lower levels is a consequence of radiative depopulating processes, such as radiative decay and radiative recombination, not being balanced by their inverse absorption processes. For low lying atomic levels where radiative processes make significant contribution to the total depopulation rates this improper balance causes deviations from LTE populations. The atom ground state is the most overpopulated level and overpopulation decreases with increasing energy of the level until p-LTE is reached for the upper atomic levels.

TABLE OF CONTENTS

LIST OF TABLES

LIST OF FIGURES

ACKNOWLEDGEMENTS

I would like to thank my husband, Jeff, for his love, support and almost infinite patience during the preparation of this thesis.

A special thanks to Mike Blades, my supervisor, for his help and guidance during the past four years.

I would also like to acknowledge the financial support of three organizations, the Natural Sciences and Engineering Research Council of Canada, the Izaak Walton Killam Fellowship Committee and the Analytical Division of the American Chemical Society for a Fellowship sponsored by E.I.Dupont and deNemours & Co.,Inc.

Chapter 1

INTRODUCTION

1.1 OBJECT OF THESIS

In the evolution of any successful new analytical concept, detailed studies of principles and mechanisms play a special and important role. These studies enrich the general understanding of the processes encountered during analysis and thus further the development of the technique and related new methods.

This thesis is a study of the mechanisms involved in excitation and ionization of analyte species in the inductively coupled plasma (ICP). The objective of the work undertaken and reported was a better understanding of the nature of the interaction between the plasma and the analyte. Plasma diagnostic studies of the various zones of the plasma provided the data base from which a model explaining observed analyte emission behavior and characteristics was developed.

1.2 HISTORICAL

A series of publications by Reed [1,2] on improvements in forming and stabilizing atmospheric pressure argon plasmas inspired Greenfield [3] and Wendt and Fassel [4] to independently initiate analytical studies of inductively coupled plasmas. The analytical performance of these early instruments was not particularly encouraging and they offered no real advantage over existing elemental analysis techniques. Over the next ten years work proceeded on the fine tuning of ICP optical emission spectroscopy instrumentation and optimization of operational

parameters for analytical performance [5-9]. At the beginning of the 70's the ICP was still very much only a research tool, however it exhibited superior detection limits compared to flame techniques. It was also a multielement technique and apparently free from many of the chemical interference effects which plagued atomic absorption spectroscopy.

In 1975 the first commercial analytical ICP spectrometer was manufactured and, in the years following, the technique's progress has been truly amazing. In the 10 years since the commercial introduction of the inductively coupled plasma instrument, ICP optical emission spectroscopy (OES) has developed into one the most widely used new analytical tools of the decade. Application areas are diverse, ranging from metallurgy, geological studies, water analyses, and effluent monitoring, to biological and clinical applications [10]. There are approximately 15 vendors internationally, the number of operating facilities is close to 5000 and increasing at a rate of about 400/year [11]. Its remarkable success can be attributed to the ICP being a nearly ideal source for elemental analysis. ICP-OES is a rapid, multielement technique, capable of determinations over a wide concentration range, varying from major to minor to trace levels, with few chemical interelement interferences.

The success of ICP-OES as an analytical method and the attractive physical properties of the ICP as a vaporization, atomization , ionization, excitation cell led to investigation of the ICP as an excitation source for other analytical methods. In 1976 Montaser and Fassel [12] published a paper on using the ICP as an atomization cell for atomic fluorescence spectroscopy. More

recently, the high degree of ionization of analyte species in the ICP has led to its application as an ion source for mass spectrometry (ICP-MS) [13]. Both of these new developments are now being manufactured as commercial instruments. The development of both ICP-AFS and ICP-MS will be enhanced by a greater understanding of fundamental processes in the ICP. These techniques require the characterization of the ICP as an atom and an ion source as well as an emission source.

A more complete and personal record of the historical development of the ICP has been published by Fassel [11].

1.3 ICP INSTRUMENTATION

The ICP excitation source is an electrodeless plasma operated at atmospheric pressure. The discharge is generated by inducing a magnetic field in a flowing, conducting gas, usually argon or an argon and nitrogen mixture. The gas flows axially through a quartz confinement tube surrounded by three or four turns of a water-cooled copper induction coil connected to a radio frequency generator. The standard frequency of operation in North America is 27.12 MHz, and the standard power output is one to three kilowatts. The high frequency current flowing in the induction coils generates an oscillating magnetic field whose lines of force are axially oriented inside the quartz tube and follow closed nearly elliptical paths outside the tube. The induced magnetic field causes electrons in the gas to flow in closed annular paths inside the quartz tube space. Since argon is initially neutral and non-conducting, theplasma must be initiated by "seed electrons" most commonly generated by a brief

Tesla discharge. The plasma forms almost instantaneously and is subsequently self-sustaining. The rate of ioniziation of argon by the moving electrons is equal to the rate of recombination of argon ions. The result is an approximately 1 eV, about 1% ionized argon plasma.

The arrangement, design and fabrication of the plasma tube (torch or burner) is one of the most critical components of the entire ICP instrument. Basically, the ICP torch consists of a container through which the discharge gases flow, a container in which the discharge is created and maintained and in which a means of introducing analyte species into the plasma is provided. An actual plasma torch will generally consist of three concentric quartz tubes. Exact dimensions and details of design differ among different users. The length of the tubes must be sufficient to prevent the discharge from arcing to the induction coil and still allow for viewing the desired radiation. Typically two or three separate gas flows are employed to sustain the high temperature discharge. The gas flows act to thermally isolate the plasma, preventing melting of the confinement tube, to stabilize and center the plasma, and to form the discharge in an annular shape through which sample aerosol can be introduced. Even in essentially identical tube configurations, gas flows can vary considerably as the result of variation in positions of the tubes relative to the induction coil and in the coupling efficiency with the magnetic field. The orifice diameter of the aerosol injection tube has been optimized empirically so as to provide sufficient linear velocity from the injector to penetrate the base of the discharge, but not to transport the aerosol

through the discharge too rapidly. Figure 1 is a schematic diagram of a typical plasma torch tube arrangement with the appropriate gas flows indicated.

The sample, most commonly in solution form, is aspirated by a nebulizer system and a fine liquid aerosol is transported up through the central tube and into the plasma. The aerosol gas "punches a hole" through the base of the plasma forming an analyte channel. The processes of desolvation, molecular dissociation, ionization equilibration and excitation take place during the analyte's progress up the channel. The processes of excitation and subsequent radiative emission creates a "plume" of analyte emission approximately 30 mm high in the area above the load coil.

A nomenclature system for the plasma zones has been suggested by Koirtyohann et al. [14]. These zones are marked on Figure 1. The "induction zone" is the doughnut shaped region close to the load coils where energy is coupled into the plasma. This is a region of intense argon emission. The "initial radiation zone" (IRZ) is a hollow bullet-shaped region of intense atomic emission. The "normal analytical zone" (NAZ), which is the usual viewing zone for analytical purposes, is located higher in the plasma about 14-20 mm above the load coils. Here the intense continuum radiation from argon-ion recombination is greatly diminished, and the plasma is more optically transparent. Emission in this region is predominantly ionic. Higher in the "tail plume" the temperature begins to decrease, and atomic and molecular emission will be seen. It is apparent from the description of these zones that there is a high degree of spatial

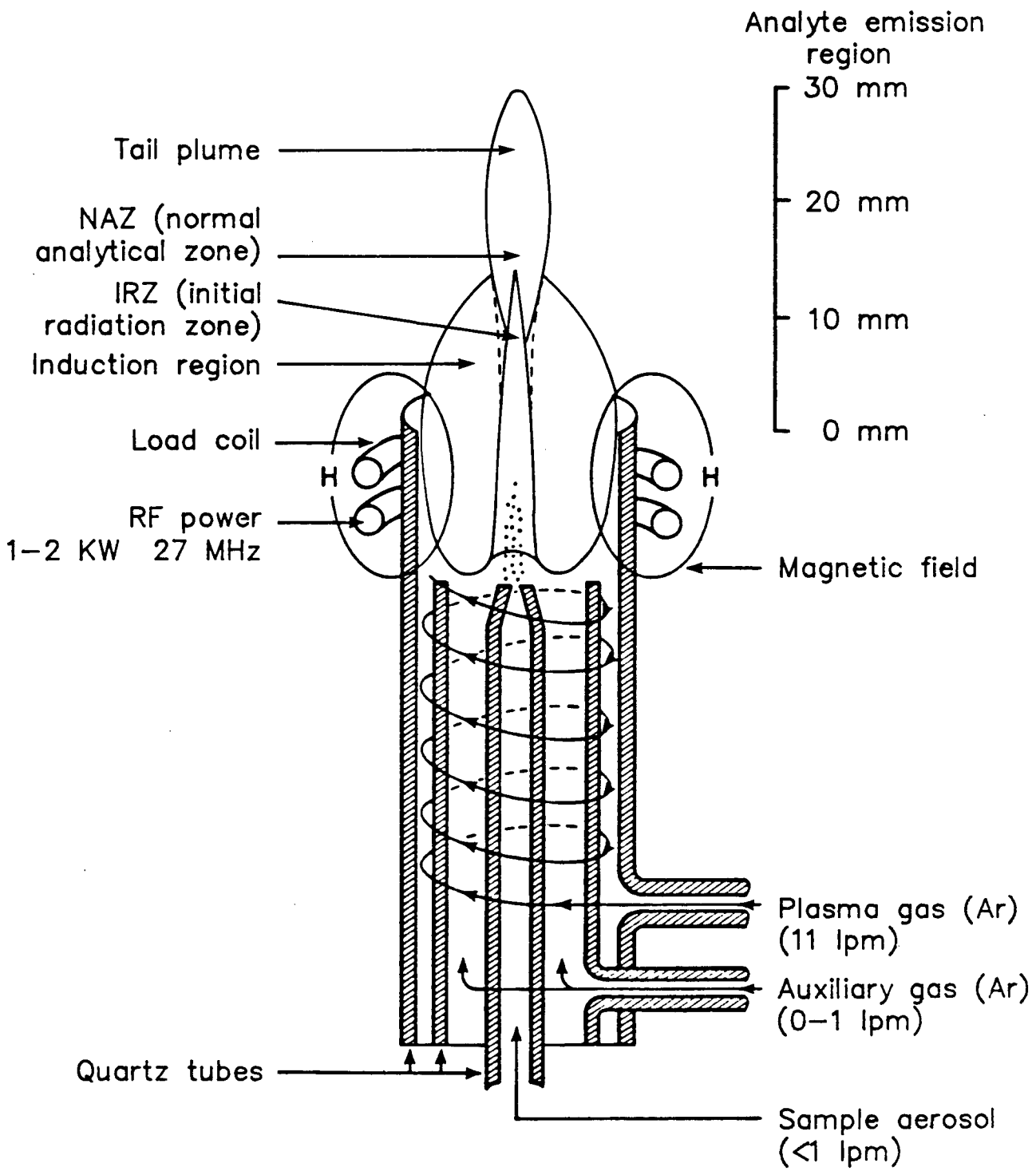

Figure 1 Schematic of inductively coupled plasma torch.

inhomogeneity in the emission from the plasma.

A more detailed account of inductively coupled plasma emission spectroscopy instrumentation and analytical procedures is available in an extensive review by Barnes [15] and in an excellent book by Thompson and Walsh [16].

1.4 EXCITATION STUDIES IN THE ICP

Characterization of the physical properties of the ICP began shortly after its conception and has proceeded parallel to its development as a mature analytical technique. Detailed fundamental studies of the plasma are still being vigorously pursued by several research groups. With the sophisticated diagnostic tools and resources presently available, it is predicted the ICP will become one of the best characterized analytical spectroscopic sources developed [10]. Spectroscopic and physical measurements provide information necessary for the determination of plasma parameters such as electron number densities, plasma and analyte velocities, temperatures, and number densities. In turn, these parameters are the basis for descriptions of the fundamental processes occurring in the discharge and interactions of plasma with analyte.

In a recent publication deGalan [17] discusses the current state of understanding of plasma excitation mechanisms. He critically evaluates four prominent plasma excitation models: Penning ionization, radiation trapping, detailed rate calculations and ambipolar diffusion. None of the models are satisfactory due to inconsistencies in their formulation and the fact that they do not adequately account for observed plasma

characteristics. DeGalan in fact establishes the validity criteria for an ICP plasma excitation model as the ability to explain three observations. They are in brief: 1) measured electron density and argon ion density do not agree with measured excitation temperatures, 2) excitation temperatures vary with the energy levels used to measure them and 3) ion-atom emission intensities for an element are higher than expected from LTE expressions using an excitation temperature.

In this work the plasma was characterized by the emission intensity of spectral lines and spectral line profiles. The ultimate object of this study was the interpretation of all spectroscopic observations in terms of a fully consistent plasma model. Because spectra arise from atomic processes, this model will emphasize the particulate nature of the plasma rather than the fluid aspects that characterize many of the properties of a plasma. Thus, there was no attempt to describe the plasma in terms of its power balances [18] or gas flow velocities [19] as has been done by other researchers. The emission studied originated from analyte species introduced into the plasma and modeling attempts were directed towards an explanation of analyte behavior rather than a description of the argon plasma itself.

Spectral lines originate from transitions of electrons between energy levels of atoms or ions. The intensity of a spectral transition from a higher level p to a lower level q , I_{pq}, is related to the population n_p of the higher energy level through

$$I_{pq} \propto A_{pq}\, h\nu_{pq}\, n_p\, \beta_{pq} \qquad (1.1)$$

The observed intensity thus depends on

a) probability of there being an electron in the upper level of the transition, n_p,

b) atomic probability of the transition in question, A_{pq}, and

c) probability of the photons thus produced escaping from the volume of the plasma without being reabsorbed, β_{pq}.

One of the favorable characteristics of the ICP as an analytical source is that the analyte emission escapes without being reabsorbed. For analyte emission the plasma can be considered to be optically thin, i.e. β_{pq} is equal to one. Transition probabilities areavailable in atomic physics data bases. Thus, emission intensity can be directly related to level population.

The distribution of electrons among the various energy levels available is determined by collisions with other particles and by radiative processes. Therefore, the object of an excitation model for the ICP is a description of level populations for analyte species and identification of the plasma processes important in establishing this distribution.

1.5 MECHANISMS: COLLISIONAL AND RADIATIVE PROCESSES

One of the goals of a descriptive model of plasma processes is to identify the pertinent mechanisms through which energy is exchanged between various species in the plasma discharge. In this section, the collisional and radiative processes believed important in plasmas are introduced. More detailed discussions of atomic processes are available in the comprehensive reviews

published by Hasted [20], Bates [21] and Elton [22].

Hasted [20] lists six types of particles present in a plasma and over one hundred possible atomic processes for these particles. The ICP is even more complex because, in addition to the argon gas, analyte species and solvent dissociation products are present. To limit the problem, this discussion will only be concerned with the processes determining analyte excitation and ionization.

The important species in the ICP are: Analyte atoms (M); singly charged analyte ions (M^+); in some cases doubly charged analyte ions (M^{+2}); argon atoms (Ar); and argon ions (Ar^+); free electrons (e); and photons, both continuum ($h\nu_{cont}$) and line ($h\nu_{line}$). The atoms and ions are distributed between the ground state and the various excited state energy levels available to them.

A number of possible interactions may occur between these particles. When two particles approach one another they interact in some manner, if after the interaction some measurable change has occurred, a collision has taken place. Collisions are classified into two basic types, elastic and inelastic collisions. In an elastic collision the particles change their directions of motion, but the total initial momentum and kinetic energy of the particles is conserved. All other types of collisions are called inelastic. In inelastic collisions kinetic energy may be lost to excite or ionize one of the particles, or conversely, energy "stored" in an excited state may be transferred to kinetic energy imparted to the colliding partners. Stored energy may also be released radiatively in the form of a

photon.

The inelastic collisions and radiative processes believed to be important in maintaining ICP analyte level populations are outlined below.

(1) Collisional excitation and de-excitation by electrons:

Collisional excitation is the transition of a bound orbital electron in an atom (or ion) of analyte species M to a higher bound state by the absorption of kinetic energy by an inelastic collision with a free electron. When the transition is between levels p and q it may be shown by

$$M_q + e \rightarrow M_p + e \qquad \text{where } E_p > E_q$$

E_p and E_q are the excitation energies with respect to the ground state of the two states p and q. The corresponding inverse process is de-excitation shown by

$$M_p + e \rightarrow M_q + e \qquad \text{where } E_p > E_q$$

In the first reaction kinetic energy is taken up from the electron by the analyte atom or ion to produce an excited state. In the reverse process excitation energy is carried away by the colliding electron in a radiationless transition. For the forward process the energy of the electron must be equal to, or exceed the transition energy involved. The forward process is a populating process for level p, whereas the reverse is a depopulating process for that level.

(2) Radiative Decay

De-excitation of species M_p (or M^+_p) can also proceed by spontaneous radiative decay, with the emission of a photon of energy $h\nu_{line}$ according to

$$M_p \rightarrow M_q + h\nu_{line} \qquad \text{where } E_p > E_q$$

Spontaneous radiative decay is likely to be the primary depopulating process when there are large energy differences between bound levels and relatively low electron densities. The corresponding inverse reaction of photoexcitation need not be considered for analyte species in the ICP because of the low density of the radiation field. The same argument applies to the process of stimulated emission.

(3) Collisional ionization and three body recombination

A neutral atom or an ion of species M may become further ionized by the impact of a colliding electron whose kinetic energy is greater than the binding energy of a particular orbital electron, i.e., the threshold energy for ionization. This process may be written as

$$M_p + e \rightarrow M^+ + 2e$$

The inverse of this process is three body recombination shown as

$$M^+ + 2e \rightarrow M_p + e$$

The excess energy released in the inelastic process is carried off by the free electron.

(4) Radiative Recombination

Recombination of a free electron with a positive ion of analyte species M^+ may proceed by radiative recombination described by

$$M^+ + e \rightarrow M_q + h\nu_{cont}$$

The reverse process of photoionization need not be considered because both the "photon" density and the cross section for continuum absorption are low at the photoionization threshold [22]. Recombination can proceed by both radiative and three body recombination. The first process is always present regardless of plasma density while the second process becomes significant (and perhaps dominant) at high electron densities [21].

(5) Charge transfer

The transfer of charge between heavy particles may occur through several processes. In the ICP charge transfer between argon ions and analyte atoms is shown by

$$Ar^+ + M_q \rightarrow Ar + M^+_p$$

The result of the reaction is an excited state analyte ion. The energy difference between the argon ion and the resulting analyte ion should not be too large for there to be favorable cross sections. The role of charge transfer in the ICP has been evaluated by a number of researchers [23,24].

(6) Penning Ionization and Excitation

The role of the argon metastable species, Ar_m, in ICP

processes has been investigated and speculated upon by a large number of researchers [25-31]. The process can be shown by

$$Ar_m + M \rightarrow Ar + M^+ + e \qquad \text{or}$$

$$Ar_m + M \rightarrow Ar + M^+_p + e$$

The production of an analyte ion or excited analyte ion depends on the energy involved. Excess energy is carried away by the electron. At atmospheric pressure the lifetimes of the metastable levels are short [29,30] making an overpopulation of these levels unlikely. Therefore, there is little reason to attribute a special role to argon metastable-analyte collisions over other heavy particle collisions.

Reaction rates for each of the above atomic processes are necessary to assess the role each process plays in determining plasma level populations. For spontaneous transitions, reaction rates are given simply by the product of the transition probability and the level population. For collisional processes, the rates are dependent upon the densities of the colliding species, the relative velocity of the colliding particles and the cross section for the particular reaction at that relative velocity. When a distribution of relative velocities is present, the product of the differential cross section and relative velocity must be averaged over all velocities, and the result is known as the rate coefficient for the process. For a process and its inverse, the cross sections, which are atomic properties, are equal. The forward and reverse reaction rates, which are macroscopic kinetic properties, need not be equal. The

calculation of rate coefficients depends on a knowledge of the velocity distribution, generally assumed to be Maxwellian, and the cross section for the process. Although the volume of experimental cross section data is large, it is still only a small fraction of what is needed. Approximate general formulae exist which permit quick estimates for a large number of cases. Elton [22] provides a review of empirical formulae for the calculation of cross sections and rate coefficients for many atomic processes.

One approach to determining level populations from these microscopic processes is to use the collisional-radiative model as described by Bates et al. [32,33]. For every bound level an equation describing the rate the level is populated at is written. All populating and depopulating processes for the level are included. Some form of cutoff procedure is used to prevent an infinitely large number of bound levels. Assuming quasi-steady-state, the rate of change of the population of all states except the ground level is set equal to zero. If n levels are being considered, the result is (n-1) linear simultaneous equations in n variables and one rate equation for the ground state. Details and results of this method are available from a number of sources [32-34].

Several workers have used the collisional-radiative rate model to study the ICP phenomena. Hasegawa and coworkers [26,35] have calculated the level populations of argon and examined the mechanisms responsible. Lovett [36] has applied the model to the calculation of analyte level populations in the ICP. As an example of the number of calculations required in this kind of

treatment, Lovett employed 148 energy levels for the calculations for barium resulting in 148 X 147 possible transitions between energy levels. All of these transitions must be given reaction rates and the rates may be the result of more than one type of process. The real shortcoming of this method though is not the massive calculations involved but the tremendous uncertainties in the rate coefficients. Integration of the results of these calculations with experimental observations will be discussed in detail later.

1.6 Thermodynamic Equilibrium

Characterization of a plasma and level populations using the above mechanisms requires a detailed knowledge of rate constants of both forward and reverse reaction rates for all processes. A special situation exists when each process is counterbalanced by its inverse and these processes occur at equal rates by the principle of detailed balance. If this condition applies to all processes important in populating each level and populating processes take place with sufficient rapidity that the distribution responds instantaneously to any change in the plasma conditions, then this principle leads to the model of thermal equilibrium. The population distribution is determined by the statistical mechanical law of equipartition among energy levels and does not require knowledge of atomic cross sections for its calculation. The macroscopic thermodynamic state of the plasma can be described by a few variables such as pressure, concentration and temperature. Using statistical methods the microscopic thermodynamic state of the plasma is described by

macroscopic variables without any detailed knowledge of the interaction between plasma particles.

The microscopic state is characterized by a number of functions which are sensitive functions of the temperature T. These are the following:

(1) Velocity of particles/ Maxwell Distribution

If the free particles are distributed among the discrete energy levels available to them according to statistical mechanics, their continuous velocities have a Maxwellian distribution. For the state of complete thermodynamic equilibrium, the velocity distribution of all kinds of free particles (molecules, atoms, ions and electrons) in all energy levels satisfy Maxwell's distribution law, and the temperature T in the distribution function is the same for all particles and energy levels. This temperature is the kinetic or translational temperature. The electron temperature, T_e, refers to the kinetic temperature of the electrons and the gas temperature, T_{gas}, to the kinetic temperature of the neutral atoms [37].

(2)Population distribution of bound states/Boltzmann distribution.

The ratio of the number of particles of a species in two different bound states p and q is given by the Boltzmann distribution

$$n_p / n_q = (g_p/g_q) \exp [-(E_p - E_q)/kT_{exc}] \qquad (1.2)$$

where n_p, n_q = population of particles in state p and q respectively

g_p, g_q = statistical weights of the two states p and q

E_p, E_q = excitation energies with respect to the ground state of the two states p and q

T_{exc} = the excitation (population) temperature of the species

The number density of particles in excited state p (n_p) relative to the total number density (n_T) of all particles of the species in a particular ionization stage is given by

$$n_p / n_T = (g_p / Q(T)) \exp(-E_p / kT_{exc}) \quad (1.3)$$

where Q(T) = the internal partition function of the species. For complete thermodynamic equilibrium $T_{exc} = T$, the plasma temperature, for each separate kind of particle and all energy levels.

(3) Population distribution of ionization products / Saha-Eggert distribution

For each species, the number density of singly ionized positive ions in the ground state and the corresponding number density of neutral particles in a level p are related to the free electron number density by the Saha equation.

$$n_e n^+_1 / n_p = 2 (g^+_1 / g_p) (2\pi m_e kT/h^2)^{3/2} \exp(-E_{p\lambda}/kT) \quad (1.4)$$

where n^+_1, n_p = number density of the ground state ion and excited atom level p, respectively

n_e = free electron number density, the initial factor of two is the electron statistical weight

g^+_1, g_p = statistical weights of the two levels

m_e = electron mass

h = Planck's constant

$E_{p\lambda}$ = ionization energy from the level p

$T = T_{ion}$, ionization temperature

The Saha equilibrium can be viewed as a statement of the law of mass action. Equation 1.4 applies independently to each species present in the plasma. By introducing the partition functions for the neutral species, $Q_a(T)$, and for the ion, $Q_i(T)$,and employing equation 1.3, the Saha equation may be written in the form

$$n_e n_i / n_T = 2\,(Q_i(T)/Q_a(T))\,(2\pi m_e kT/h^2)^{3/2}\,\exp(-E_{ion}/kT) \quad (1.5)$$

where n_i = the total number density of ions of the species

E_{ion} = ionization energy of the species

The Saha relation may also be generalized to the case of successive ionization stages of a multiply ionized species. The temperature described by the Saha equilibrium is referred to as the ionization temperature, T_{ion}. For complete thermal equilibrium $T_{ion} = T$, the plasma temperature for all successive ionization stages of a species and for all species.

(4) Distribution of dissociation products / Guldberg-Waage distribution

The dissociation of molecules and radicals is described by the Guldberg-Waage law for dissociation-recombination. This law is only another statement of the law of mass action and has a form very similiar to the Saha equation. For thermal equilibrium

the reaction temperature, T_{react}, must be equal to the plasma temperature for all species.

(5) Distribution of radiation / Planck's law

When the photons (or radiation field) are in thermal equilibrium, the photons have an equilibrium distribution analogous to the Maxwellian function. The equilibrium value of the specific intensity is given by the Planck function and all radiation is consistent with Planck's law. The Planck function defines the radiation temperature, T_{rad}, and for thermal equilibrium this is equal to the plasma temperature, T.

The description of a plasma in thermal equilibrium (TE) is relatively simple. Macroscopic properties are interrelated by the equation of state which greatly reduces the number of independent macroscopic parameters. The state of the plasma is fully described by the mass density, temperature and chemical composition. Information about the particles can be obtained from the above laws of statistical mechanics. If TE is present all these distribution functions for different types of particles are characterized by the same temperature. Although the presence of TE implies that there are no changes on the macroscopic level, this is certainly not the case on the microscopic level. However, in TE every detailed microscopic process is balanced by its inverse.

1.7 DEPARTURES FROM THERMAL EQUILIBRIUM

1.7.1 Local Thermal Equilibrium (LTE)

For laboratory plasmas, which are limited in dimension,

thermal equilibrium is often not established. Matter escapes the plasma boundaries because of strong temperature and density gradients. Since photons are more likely to escape than other particles, it follows that the radiation field can deviate strongly from the equilibrium radiation described by the Planck function. However, the energy exchange between particles can remain locally effective so that Boltzmann, Saha and Maxwell equilibrium are retained and atoms, ions and electrons have the same temperature. The collisional rates that populate and depopulate the various energy levels of the plasma exceed the corresponding radiative rates. This phase of equilibrium is known as local thermal equilibrium (LTE). Thermodynamic properties like temperature and pressure have to be specified locally (and instantaneously). An essential feature of LTE is that matter and radiation can not be described by the same temperature, matter and radiation are "decoupled". As well there may also be spatial decoupling leading to possibly different plasma temperatures at different locations.

1.7.2 Partial Local Thermal Equilibrium (p-LTE)

Further departures from LTE can occur if gradients are so large that electrons are decoupled from the heavy particles. Because of the small mass ratio between electrons and heavy particles the heating of electrons is much faster than transfer of energy from electrons to heavy particles. Essentially a two temperature plasma is established, electrons with one Maxwellian distribution temperature and heavy particles with another.

Another consequence of the small electron mass is that they

are very effective for maintaining Saha equilibrium, at least for atomic energy levels close to the ionization limit. Free electrons and bound electrons in these upper atomic levels easily equilibrate. The free electrons impose their temperature on the excited state distribution of the atoms and as a result the T_{exc} and kinetic temperature of atoms may not be the same. In this phase, denoted as partial local thermal equilibrium (p-LTE), the Saha equilibrium is established for bound atomic levels close to the ionization limit. Energy gaps between lower lying levels are usually too large for retaining Boltzmann equilibrium. Thus the atomic energy scheme is decoupled into an upper and lower part. Although this decoupling between lower and higher levels is essentially different from that of electron and heavy particle temperatures, both decoupling phenomena usually accompany one another [38].

The concepts and conditions for local thermal equilibrium and partial LTE have been discussed by a number of authors [34,37-39]. The comprehensive and precise review of Drawin [40] is particularly recommended.

1.7.3 FURTHER DEVIATIONS FROM LOCAL THERMAL EQUILIBRIUM

The more phenomena that are decoupled from one another, the greater the departure from thermal equilibrium, and more information becomes necessary to characterize the plasma. The distribution function of the excited states deviates from its equilibrium value because population and depopulation processes for a level are not the inverse of one another. An improper balance in microscopic processes exists.

Improper balances are associated with activity on the macroscopic level due to the absence of ionization-recombination equilibrium. This results from significant transport contributions to the balance equations involving the neutral or ion ground levels. A relationship exists between the transport phenomena and the improper excitation balances. Depending on the direction of the transport contribution plasmas can be classified as ionizing or recombining plasmas.

For an ionizing plasma, there is an inward flow of ground state atoms into a volume element and an outward flow of ions. The upward ionization flow dominates over the downward recombination flow of electrons in the system of excited levels lying between the ground and continuum states. The resulting net ionization rate balances with the diffusion loss rate of ions. To maintain this upward excitation flow lower excited levels are overpopulated with respect to Saha values. As the energy of an excited level increases the overpopulation factor decreases until p-LTE is reached somewhere in the upper atomic levels.

For recombining plasmas, there is a net recombination flow of electrons. For each volume element, there is an inward transport of ions and outward transport of ground state atoms supported by a downward flow of electrons in the atomic levels. The lower energy states of the atom are underpopulated with respect to Saha equilibrium and the ion ground level. A plasma in ionization equilibrium is a special case in which the ionizing and recombining flows contribute equally.

Figure 2 is a sketch of typical distribution functions for the different types of plasmas. The straight line (curve 2)

represents a plot of an LTE population density distribution. The slope of the line indicates the temperature derived from the Boltzmann relation and gives a single LTE value regardless of energy level. For an ionizing plasma (curve 1) the slope is not constant and a determination of the electron temperature T_e with the help of the Boltzmann factor $\exp(-E/kT_e)$ is not possible, at least not with the densities of the lower excited levels. Attempts to use the Boltzmann distribution to derive temperature from the lower energy levels will result in a temperature less than T_e for an ionizing plasma. Curve 3 is a population distribution for a recombining plasma. Again the slope is not constant and the determination of T_e in the conventional way is not possible with the densities of the lower excited states. The derived temperature, in this case, will be greater than the electron temperature.

The distribution function deviates from its equilibrium shape for the lower lying energy levels due to some improper balance where populating processes are not balanced by their inverse depopulating processes. A particular type of balance will generally dominate a particular limited (lower) part of the atomic levels. Improper balances are typically classified into three possible balances, the corona balance (CB), the capture radiative cascade (CRC) balance and the ionizing and recombining excitation saturation balance (ESB). In contrast with proper balances (LTE), information about the elementary processes of production and destruction of level populations is required in order to to calculate the distribution function. Figure 3 is a schematic illustrating the essentials of these improper balances,

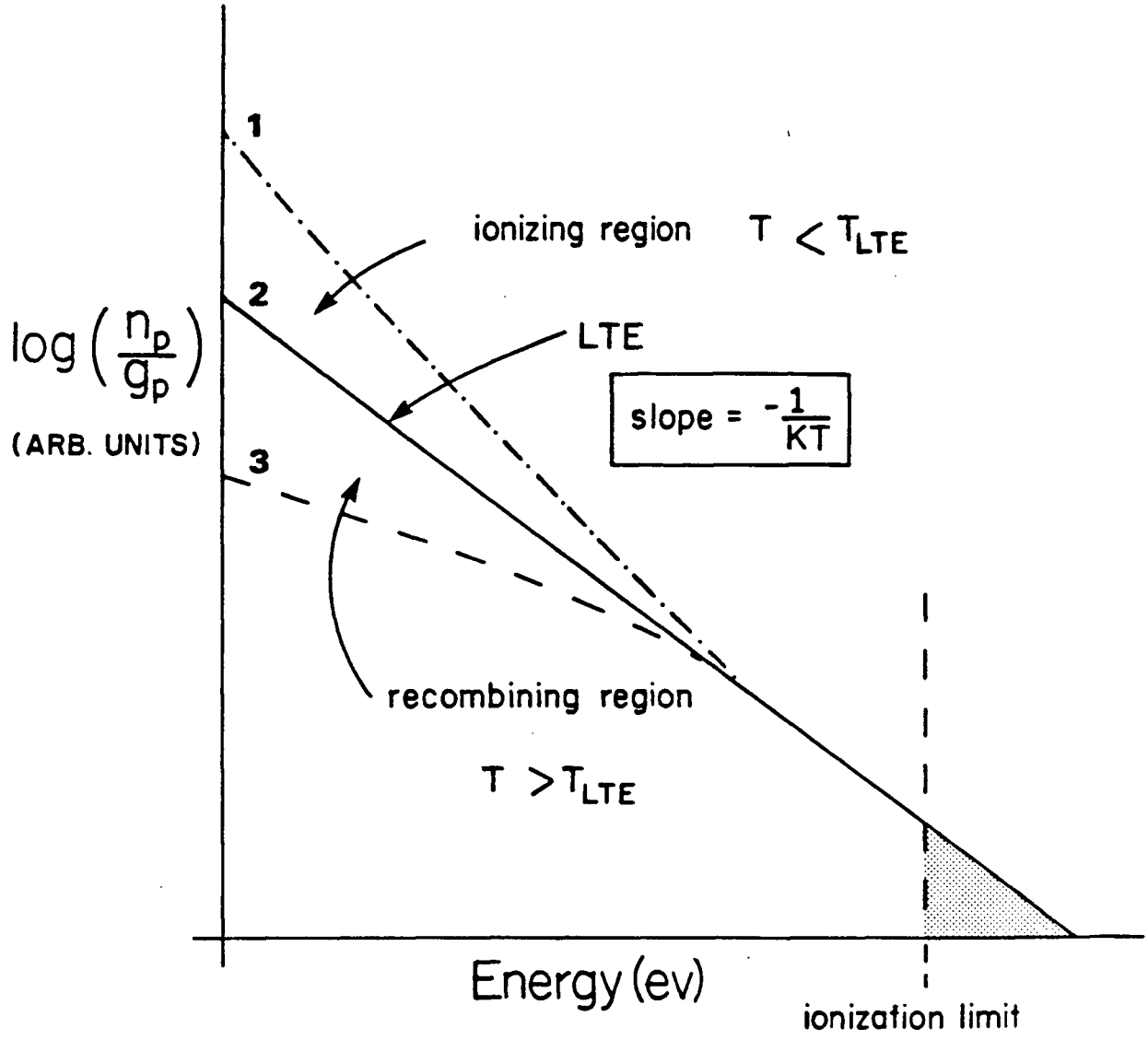

Figure 2 Schematic plot of population distributions:curve 1 - represents an ionizing plasma; curve 2 - LTE; and curve 3 - a recombining plasma.

and a short description of the different domains follows.

(1) Corona Balance (CB)

The population density of a corona level results from production due to excitation of ground state atoms balanced with destruction due to radiative decay. Ionization occurs almost exclusively from the atom ground state via collisional ionization and is balanced by radiative recombination from the ion ground state to the atom ground state. This model was proposed to explain some features of the spectrum of the solar corona and is typical of plasmas with very low electron density.

(2) Capture Radiative Cascade Balance (CRC)

The capture radiative cascade balance is another model applicable to low electron density plasmas and has been discussed by Seaton [41]. Both the population and depopulation processes in the CRC domain are radiative in character. Levels are populated by radiative recombination from the ion level and capture and radiative cascade from higher levels. Depopulation occurs by radiative decay. It is not possible to differentiate between the corona and capture radiative cascade balances on the basis of the population distribution of excited states alone. It is also necessary to have a knowledge of the atom and ion ground state populations.

(3) Excitation Saturation Balance (ESB)

This particular plasma regime has been discussed in detail in series of articles by Fujumoto [42-45] and experimental confirmation of this type of population distribution is provided

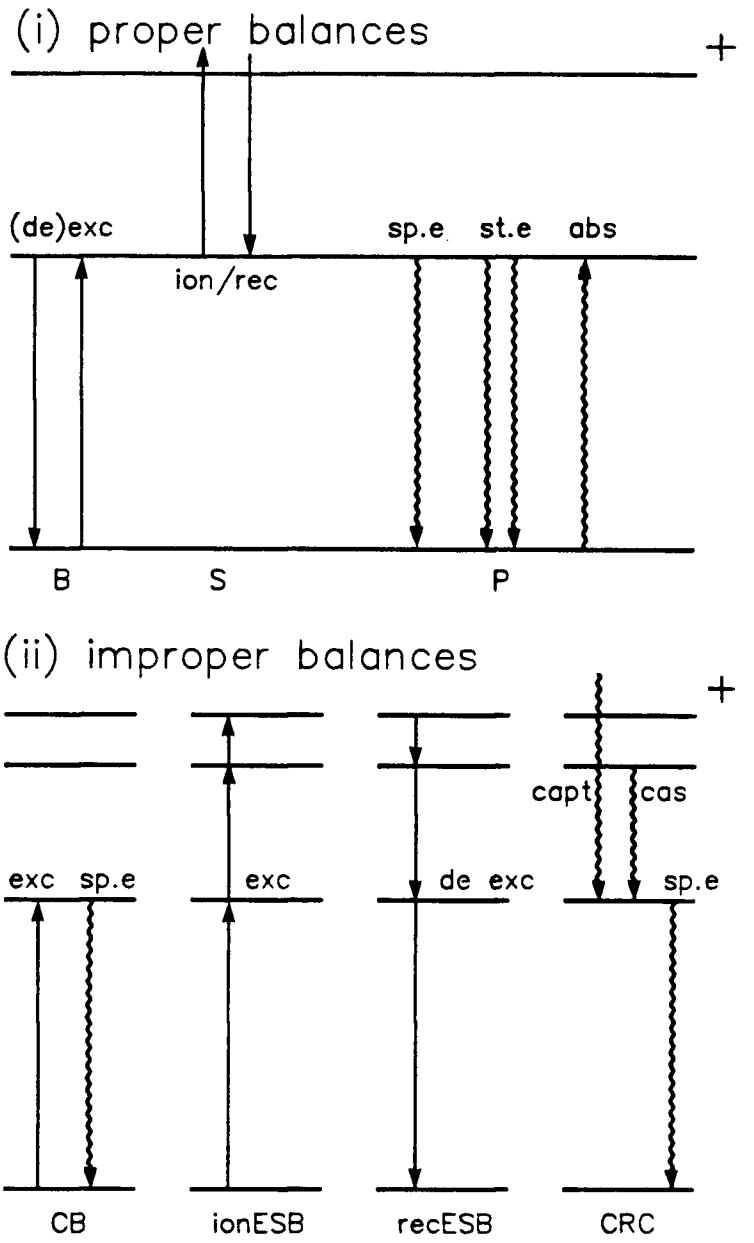

Figure 3 A comparison between (i) the proper balances of Boltzmann (B), Saha (S) and Planck (P) and (ii) the improper balances of the Corona (CB), the ionizing excitation saturation balance (ionESB), the recombining excitation saturation balance (recESB) and the capture radiative cascade (CRC).

Abbreviations: (de)exc = (de)excitation; ion/rec = ionization/recombination; sp.e = spontaneous emission; st.e = stimulated emission; abs = absorption; capt = capture; casc = cascade.

by Tachibana and Fukuda [46] and van der Mullen et al. [47]. The excitation saturation phase is due to the dominance of collisional excitation and de-excitation processes over radiative processes long before the levels under consideration come into Saha-Boltzmann equilibrium [47]. For the ionization excitation saturation balance (ionESB), the dominant populating process is collisional excitation from the adjacent lower level and the depopulating process is collision excitation to the adjacent upper level. In ionizing plasmas this results in an upward flow of ladder-like excitation, there is a ladder-climbing excitation flow from lower to higher excited states, up to the levels which are in p-LTE. The recombining excitation saturation balance (recESB) applies to recombining plasmas. Population is via de-excitation from the higher adjacent level and depopulation by the same mechanism to the adjacent lower level. The result is a ladder-like de-excitation flow from the upper energy levels in p-LTE.

The particular balance controlling the number density of any given excited state is a function of electron density, temperature and atomic structure. Van der Mullen [38] has published an extensive work classifying plasmas into the various domains and the criteria for the divisions between domains. In general, the very upper energy levels are in p-LTE for both ionizing and recombining plasmas. For an ionizing plasma the intermediate levels are controlled by the ionization excitation saturation balance and the lowest energy levels by the corona domain. The capture radiative cascade model applies to the low

energy, low electron density phases of the recombining plasma and the recombining excitation saturation balance to the intermediate levels. The upper limit of the corona and capture radiative cascade balances are when the rate of collisional de-excitation is greater than or equal to the rate of radiative decay. The excitation saturation balance passes into p-LTE when the collisional de-excitation rate is ten times the radiative decay rate. The radiative decay rate is independent of n_e while collisional de-excitation increases with increasing n_e. In plasmas with low electron density, radiative processes control the population of levels; at high electron densities collisional processes dominate. For intermediate values of n_e there will be a boundary in the system which separates lower (radiative) levels from higher (collisional) levels.

1.8 EVALUATING THE ICP FOR LOCAL THERMAL EQUILIBRIUM

The concept of local thermal equilibrium is an extremely powerful one due to the simplicity and generality of the LTE relationships. When a plasma is in local thermal equilibrium only a few macroscopic variables such as electron density, pressure and temperature need be measured to determine all level populations via the Saha and Boltzmann distribution functions.

There are two approaches to establishing whether or not a source is in LTE. One method is to evaluate the criteria relationships which have been determined by authors such as Drawin [38,40] and Griem [39] as necessary conditions for LTE. These criteria are of limited value as they only provide an order of magnitude estimate and in some instances may not be indicating

the boundaries for LTE [45]. The other approach for proof of the existence of LTE is to measure the various distribution temperatures of the plasma using the distribution functions listed in Section 1.5. If all temperatures for all species are equivalent, LTE is indicated.

Spectroscopic methods are the most popular for the measurement of plasma temperature primarily because they do not disturb the plasma and if the temperature is very high may be the only applicable method [48]. The details of spectroscopic temperature measurement have been discussed in a number of publications [37,48-52]. Briefly, the emission intensity of one or more spectral lines are measured, equation 1.1 relating emission intensity to level population is substituted into a distribution function, Boltzmann to determine T_{exc}, Saha for T_{ion}, and a 'temperature' determined. Strictly speaking, the method is valid only for sources in LTE. If the source is not in LTE, the experimental value is an apparent temperature applicable only to the energy levels of the thermometric species used to derive it [48].

Many researchers have measured various spectroscopic temperatures and electron concentrations in the ICP in an effort to clearly demonstrate the presence or absence of LTE. It rapidly became clear that different measurement techniques produced mutually different values. Table I is a listing of various ICP temperatures evaluated by a number of workers. Substantial differences exist between the various types of temperature and even within a particular temperature type a wide range of values is indicated. The range of temperature values

Table I

Spectroscopically Measured Temperatures in the ICP

Investigator	T_{gas}	T_{exc}	T_{ion}	T_e
Abdallah and Mermet [56]	4500	4800		
Alder et al. [53]		5900-7720	7530-8110	
Batal et al. [57]				10000
Blades and Caughlin [58]		4000-7000		
Faires et al. [59]		5600		
Faires and Palmer [60]	6310			
Furuta [61]		5300-6800	6700-7200	
Furuta and Horlick [62]		5000-6000		
Gunter et al. [63]		7800		
Hasegawa and Haraguchi [35,64]	3000-7000			8400
Huang et al. [65]				11600
Human and Scott [66]	5000-7000			
Jarosz et al. [55]		4400-4850	6700-7400	
Kalnicky et al. [54,67]		5500-7000		
Kawaguchi et al. [68]	3000	6500		
Kornblum and deGalan [52,69]	2000-3000	4000-6500	8000	
Nojiri et al. [70]		7000		
Uchida et al. [25]		7000		

could not be attributed to experimental imprecision [53] or errors in transition probabilities [52,54]. These inconsistencies were not removed, when in later studies Abel inversion techniques were employed to resolve the marked radial inhomogeneity of the plasma [52,54,55].

Kornblum and deGalan [52] summarize the results of spectroscopic temperature measurements with the following relations

$$T_{gas} < T_{exc} < T_{ion}$$

$$T_{exc} = f(E_{exc})$$

$$T_{ion} = f(E_{ion})$$

This is considered sufficient evidence that excitation mechanisms in the ICP are not completely thermal.

Alder et al. [53] and Kornblum and Smeyers-Verbeke [71] further explored the relationship between excitation energy and derived temperature. T_{exc} was measured using twenty lines of FeI. Excitation temperature increased with increasing energy of the levels used. Overpopulation of the low energy levels was attributed to radiative depopulating processes dominating over collisional processes. The results of Walker and Blades [72] and Furuta [61] also indicate a correlation of energy level and T_{exc} for FeI.

Kalnicky et al. [67] measured electron density by Stark broadening of the H_β line, broadening of argon lines and the Saha equation. The Saha values were almost two orders of magnitude smaller than the Stark broadening n_e values. Electron density

can be measured by Stark broadening without any assumptions about the plasma temperature, while the Saha method requires LTE to be valid.

The diversity of temperatures makes it readily apparent the ICP is not in local thermal equilibrium. These deviations have been interpreted as overpopulations of analyte ion excited levels and underpopulations of the argon ground level with respect to the LTE values [73]. Excitation mechanisms, such as Penning ionization from metastable argon [25,27,28], radiation trapping [29,30] and charge transfer [23,24], have been proposed to account for these deviations but none have provided a totally consistent explanation.

1.9 DEVIATIONS OF THE ICP FROM LOCAL THERMAL EQUILIBRIUM

If the plasma is not in LTE the production-destruction balance is improper and the shape of the distribution function for bound energy levels will deviate from the equilibrium shape. The magnitude and form of the deviation reflects the unbalanced processes and gives information about the plasma. Determining the deviation from the equilibrium value and its underlying causes was the purpose of this work.

Van der Mullen [38] suggests that even for large deviations from LTE, somewhere close enough to the ionization limit, Saha equilibrium will be valid for the upper atomic energy levels and the ion ground state. Partial LTE exists for the uppermost levels and it is only a matter of determining the distribution function for the lower levels.

It is useful to relate the populations of the lower non-

equilibrium levels with that of the upper p-LTE part by introducing the equilibrium departure factor b(p) for level p

$$b(p) = n(p) / n(p)^S \qquad (1.6)$$

where $n(p)$ = the actual population of level p

$n(p)^S$ = the population of level p according to the Saha equation based on the ion ground state and upper energy levels of the atom

Levels for which $b(p) < 1$ are said to be underpopulated whereas levels for which $b(p) > 1$ are overpopulated. The magnitude and direction of deviation from local thermal equilibrium can be ascertained via this parameter. Before that can be accomplished the input parameters for the Saha equation to calculate $n(p)^S$ must be determined.

In a recent paper, Raaijmakers et al. [73] state a key feature of an LTE plasma. For plasmas in LTE of known pressure, it is possible to determine temperature simultaneously with the electron density, since the two are linked through a system of equations. The measurement of only one of these parameters is necessary and sufficient to characterize the discharge. Plasma electron density can be determined in a manner that does not depend upon the assumption of LTE in the plasma. This makes n_e a convenient and appropriate parameter to characterize the ICP. Measured electron density and the plasma pressure can be used to evaluate a temperature and expected LTE values of other variables. The ICP is not in local thermal equilibrium. However, if the departures from LTE are not large, i.e. $0.1 <$

$b(1) < 10$, this calculation will provide a reasonable estimate of the electron temperature, T_e. Even if the deviations from LTE are substantial this temperature in conjunction with an experimental n_e will at least provide a consistent LTE framework for evaluating deviations from LTE. By comparing experimental measurements to calculated, theoretical, LTE values, deviations from LTE can be quantified.

In this work a complete set of electron densities at a variety of powers and spatially resolved positions have been measured. These values of n_e have been used to calculate the expected LTE temperature, $T_{e,LTE}$. $T_{e,LTE}$ and n_e were further used to calculate LTE ion-atom emission intensity ratios and degrees of ionization. The LTE values were compared to experimental values measured under the same conditions as n_e. The results of these comparisons yield new insight into ICP excitation mechanisms and a model for excitation and ionization of analyte species is proposed.

Chapter 2

INSTRUMENTATION AND DATA TREATMENT

2.1 INTRODUCTION

In this chapter the tools common to all experimental measurements are described. They consisted of the ICP experimental system and a number of data treatment techniques. Spatially resolved experimental measurements were made with the ICP system, the raw data smoothed, a coordinate transformation from lateral to radial coordinates performed and after appropriate calculations the final spatial results presented via contour plots. The descriptions presented here are brief and if more information is required references to more detailed publications are provided.

2.2 INSTRUMENTATION

A schematic of the ICP optical emission system utilized in this study is given in Figure 4. The rf generator, plasma torch assembly, torch and diode array spectrometer used have been previously described [74-76]. The complete experimental system is summarized in Table II. With the exception of the photodiode array detection system and translation stage, the components used were standard ICP instrumentation and the reader is referred to the reviews of Barnes [15] and Thompson and Walsh [16] for more details about ICP instrumentation.

The system described above was used to perform all experimental measurements except for those presented in Chapter 6. For this series of experiments the detection system was changed. A Schoeffel-McPherson (Acton, MA) Model 2061, 1 meter,

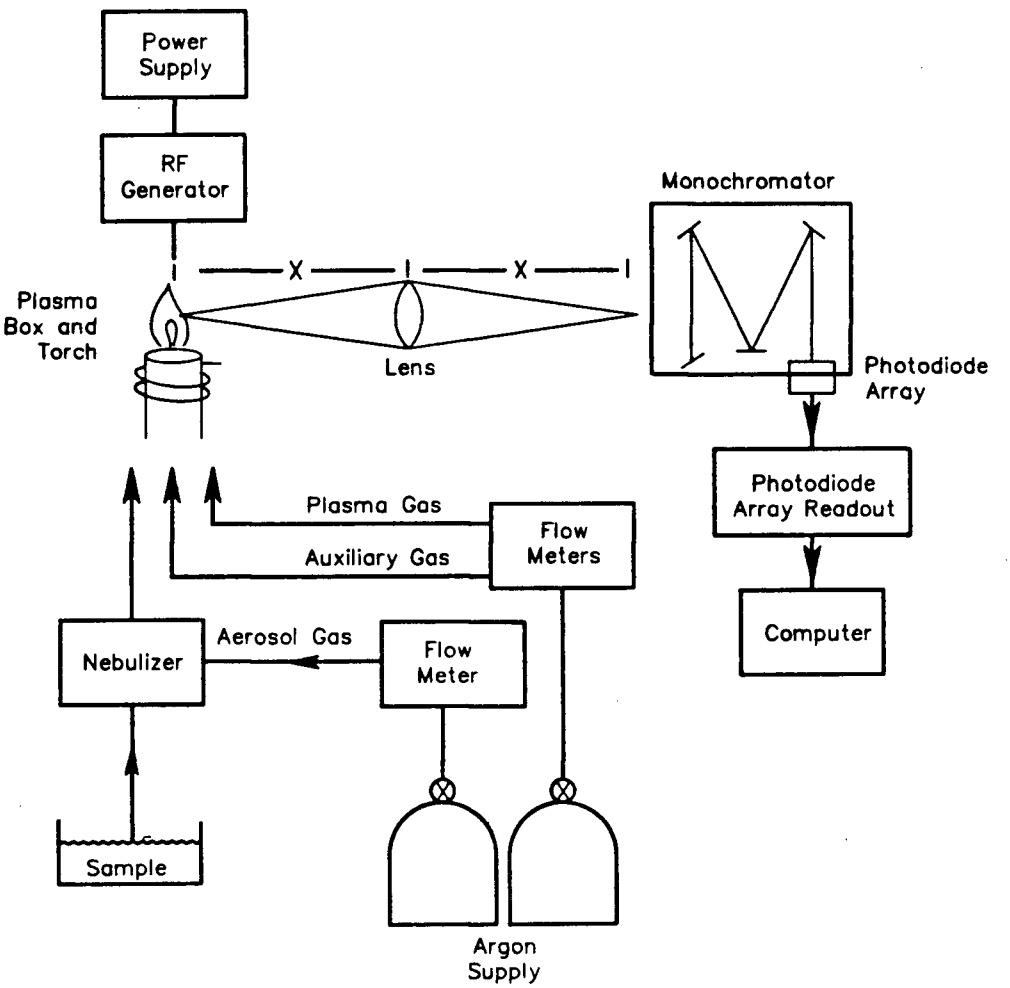

Figure 4 Schematic of inductively coupled plasma optical emission spectrometer.

Table II

Experimental System

ICP	Plasma-Therm (Kresson, NJ) HFP-2500E r.f. generator, AMN-2500E automatic matching network, APCS-1 automatic power control unit.

Torch	Quartz torch constructed by U.B.C. glass shop
	outer tube - o.d. = 20 mm, i.d = 17 mm;
	intermediate tube - o.d. = 15 mm, i.d.= 13 mm;
	aerosol tube - o.d. = 6 mm, i.d.= 1.5 mm.

Nebulizer	Plasma-Therm Model GN5601 glass concentric
Argon flows	Plasma - 11 1 m^{-1} Auxiliary - 0.2 1 m^{-1} Nebulizer - 0.9 1 m^{-1} unless otherwise indicated
Translation stage	Stepper-motor driven linear stage (Daedal, Model 4979, Harrison, PA)
Optics	1:1 magnification achieved with 150 mm focal length, 50 mm diameter, plano-convex fused silica lens, (focal length corrected for achromatic response).
Monochromator	GCA-McPherson model 270(Acton, MA), 0.35 m focal length, Czerny-Turner.
Grating	2400 line/mm holographic (1.0 nm/mm reciprocal linear dispersion).
Detector	Reticon RL-1024S linear photodiode array (Reticon, Sunnyvale, CA), with RL-1024S-3 evaluation board.
Entrance slit	50μm wide, with a 1.0 mm aperture.
Data system	Apple II-plus computer with an Interactive Structures (Bala-Cynwyd, PA) AI13, 12-bit ADC.

Czerny-Turner monochromator was used as a dispersive system. The grating used was a Schoeffel-McPherson Model AH-3264, 120 x 140 mm, holographic grating with 1200 lines/mm. The reciprocal linear dispersion of this spectrometer was 0.833 nm/mm. The detector used was a Reticon (Sunnyvale, Ca) Model RL-4096 linear photodiode array (LPDA). This LPDA has 4096 discrete photodiodes. Details of the system are available in reference [72].

The experimental systems used had tremendous data collection capabilities due to the combination of the photodiode array detection system and computer controlled translation stage. A schematic of the photodiode array data acquisition system is given in Figure 5. The linear photodiode array, was mounted horizontally in the exit focal plane of the monochromator, such that, when read out, it provided a simultaneous measure of the emission spectrum over a wavelength range of approximately 20.0 nm. The mounting of the ICP torch enclosure on a stepper-motor-driven linear translation stage allowed horizontal translation of the torch enclosure in precise multiples of 0.0127 mm steps. The diode array signal acquisition and source translation functions were supervised by a microcomputer (an Apple II^+ or Compupro 816). This combination allowed the simultaneous acquisition of lateral profiles at a number of wavelengths and made possible the rapid measurement of spatially resolved plasma emission characteristics. Vertical resolution was achieved by raising or lowering the monochromator.

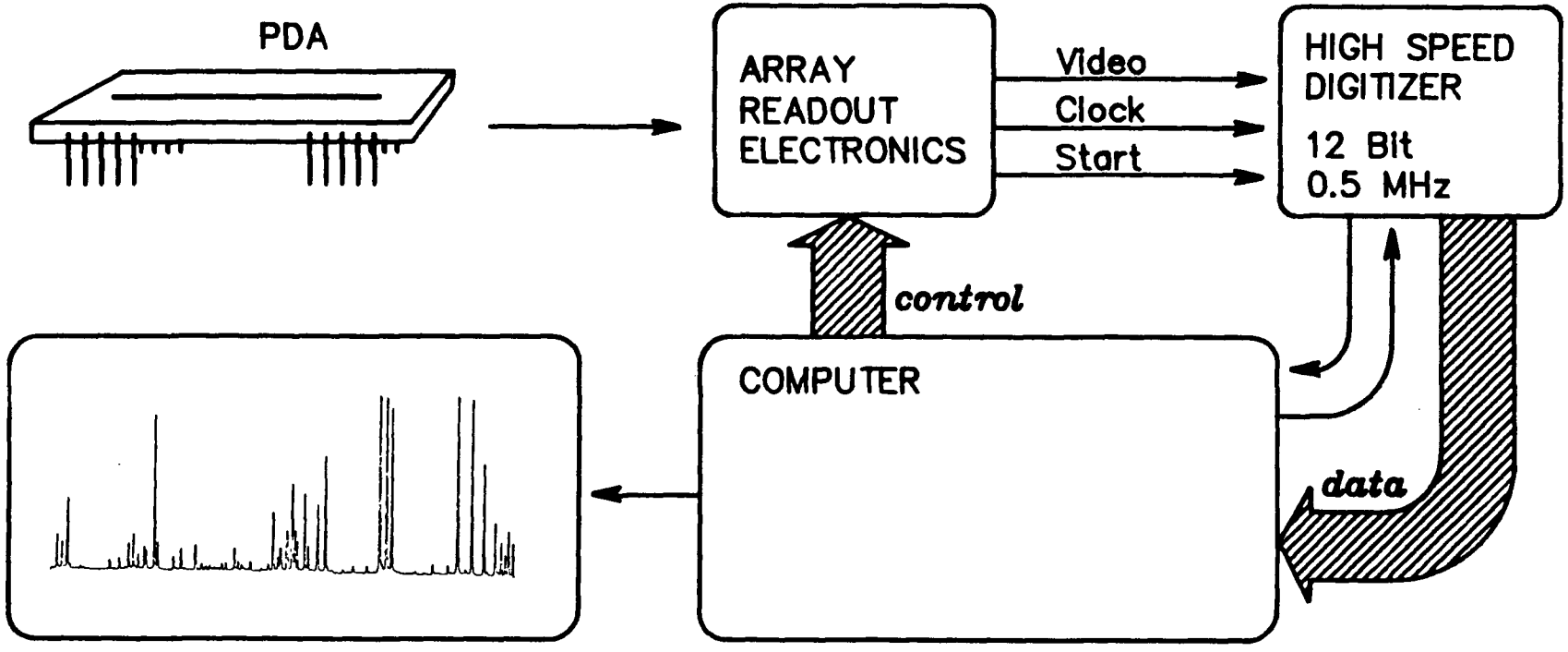

Figure 5 Schematic of photodiode array detector system.

2.2 DATA SMOOTHING

Before performing the coordinate transformation some experimental noise was removed from the experimental lateral wavelength profiles by smoothing the data. Two different approaches were used to accomplish this, one involved fitting the experimental data to a number of polynomials and then interpolating. The other was data smoothing by a simplified least squares procedure.

The algorithm for calculating an n th degree polynomial from experimental data was taken from reference [77]. The lateral wavelength profiles were divided into a number of segments and each segment fit to a polynomial. An interpolation was performed to obtain smooth lateral wavelength profiles. The number of segments, typically 3 to 15, and degree of polynomial, 3 rd to 6 th order, were determined by the amount of noise in the experimental data and the shape of the lateral profile. The best fit was chosen by minimizing the sum of the squares of differences between experimental and smoothed data.

The other approach was to use a simplified least squares procedure as described by Savitzky and Golay [78]. A 13-point smoothing function was applied. On raw data with a moderate noise level, the Savitzky-Golay method was superior for lateral profiles with an off-axis maximum and in other cases performed equally as well as the polynomial fit. If the raw data was extremely noisy a polynomial fit was required.

2.3 ABEL INVERSION

When dealing with a spatially unhomogeneous source, such as the ICP, it is necessary to perform Abel inversions of lateral data to obtain accurate spatially resolved radial values of diagnostic parameters derived from intensity measurements. The toroidal shape of the intensity distribution observed in the ICP close to the load coil [52,54,67,69] make this transformation particularly important in this region.

The Abel integral equation was used to obtain radial distributions from side on spectroscopic observations. In Figure 6 the relationship between the measured lateral radiance, I(x), and the desired radial value, I(r), is illustrated. The figure is a slice of plasma, in which the view is down the central plasma axis, the z' axis, and intensity measurements are made in the y' direction. The problem is given I(x) find I(r) where I(x) denotes radiance (or intensity) in the y direction at a distance x from the y'z' plane and I(r) is the emissive power per unit volume per unit solid angle at a distance r from the z' axis. On any line of sight parallel to the y' axis, the intensity I(x) is recorded as an integral of I(r) taken over the depth of the plasma. The intensity I(x) can be written as

$$I(x) = 2 \int_x^R \frac{I(r)\, r\, dr}{(r^2-x^2)^{1/2}} \qquad (2.1)$$

I(r) is the unknown function and can be removed from the integrand by inverting Eq. 2.1. This yields

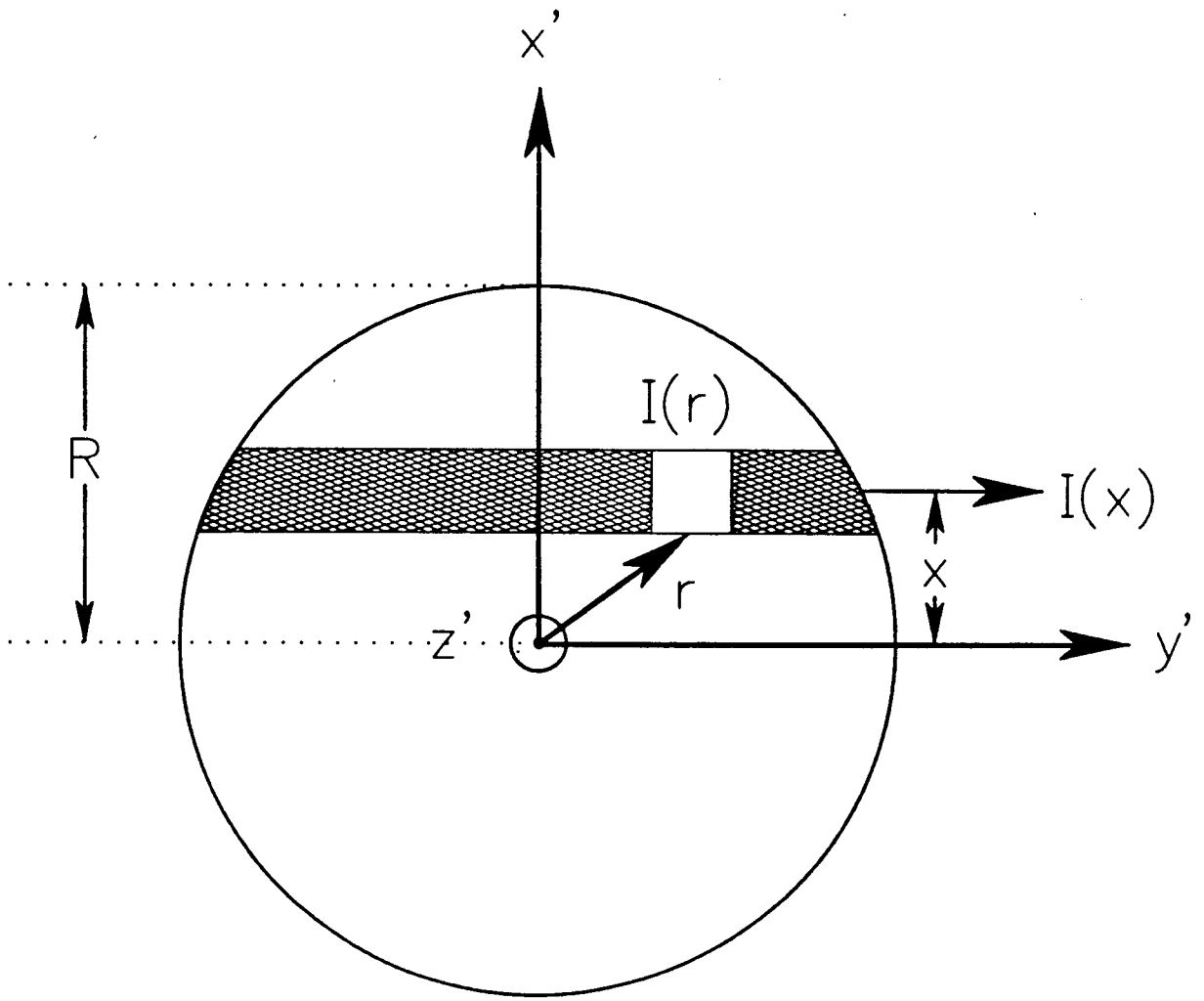

Figure 6 Top view of slice of plasma, showing relationship of variables involved in Abel inversion.

$$I(r) = -1/\pi \int_r^R \frac{I'(x)\ dx}{(x^2-r^2)^{1/2}} \qquad (2.2)$$

where I'(x) is the first derivative of the radiance function with respect to the lateral coordinate x.

Generally, there are two approaches to solving these equations: numerical techniques and data approximation schemes utilizing curve fitting or other mathematical approximations. In this work the numerical technique of Nestor and Olsen [79] has been used. It was assumed that I'(x) was constant over each small interval $\Delta x = a$. The emission coefficient at a radius of $(k-1)\Delta x$ is

$$I_k(r) = -2/\pi a \sum_{n=k}^{N-1} I_n(x)\ B_{k,n} \qquad (2.3)$$

where

$$B_{k,n} = -A_{k,k} \quad \text{for } n = k$$

$$B_{k,n} = A_{k,n-1} - A_{k,n} \quad \text{for } n \geq k + 1$$

$$A_{k,n} = \frac{[n^2 - (k-1)^2]^{1/2} - [(n-1)^2 - (k-1)^2]^{1/2}}{2n - 1}$$

Here k and n represent the respective radial and lateral points under consideration and $I_n(x)$ is the measured radiance at a distance $(n-1)\Delta x$ from the center. k = 1 at the center, a is the interval width (the same for all intervals) and N is the number of points used. The emission coefficient at the outer edge is taken to be zero. The modification of this technique described by Blades [74] for performing asymmetric Abel inversions was used.

For reliable radial intensity calculations a number of conditions must be fulfilled [54]. First, the analyte emission intensity distribution must be circularly symmetric about the plasma axis. A slight asymmetry is introduced by the load coil geometry of the ICP and the asymmetric Abel inversion is an attempt to deal with this problem. Secondly, the depth-of-field of the optical transfer system must extend beyond the plasma boundaries so all emission points within the source volume are transferred with the same efficiency. This is accomplished with a low aperture optical system. In addition to these requirements, the plasma source must be optically thin i.e., there must be negligible self-absorption of the emission lines of interest.

The accuracy of the technique used to perform the Abel inversion is important. Cremers and Birkebak [80] evaluate six different methods of Abel inversion for three functions representing typical lateral intensity distributions observed in the plasma. The exact solution to the Abel integral is known for these functions and the difference between the Abel inverted data and exact solution evaluated. The Nestor and Olsen method rates last if exact values of I(x) are used. However, when the input data have as little as 0.5 % noise added the method of Nestor and Olsen is found second only to curve fitting techniques. For 50 point Abel inversions the standard deviation of the difference between exact and calculated solutions was 0.0164 to 0.0194. Algeo and Denton [81] also observe that as the noise in input data increases the accuracy of different methods change.

The error in the Abel inversion procedure used in this work

was calculated for a set of test data for which both the lateral and radial intensities are explicitly known [74]. The relative error varies from 0.3% at the center, 0.13% off center and 3% at the edges where the lateral intensity is low. Larger errors were introduced if the Abel was not carried right to the edge of the data where I(x) equaled zero or if the center was improperly chosen. Abel inverting over only 70 of the 75 lateral points resulted in a difference of 5.5% between Abel and actual radial values. Choosing a center 2 positions off center for a 75 point Abel caused errors of 15% at the center, 5% off center and 20% or greater at the edges. Based on these results, errors of the order of 5 to 15 per cent can be expected when Abel inverting real experimental data where the center is not precisely known and the lateral intensity at the plasma edge is not always zero.

2.4 CONTOUR PLOTTING

In order to present the volume of spatial data collected in a concise and easily understandable form contour plots of plasma parameters illustrating variation with spatial position were used. The contour plots presented in this work were generated by computer. In general, computer contour plotting routines are very complex and time consuming, however, an innovative algorithm developed by Simon Jr. [82] permits computer generation and plotting of contour plots by microcomputers. Instead of attempting to find and follow contour lines, it looks through the data array and draws a dot whenever it crosses a contour line. With sufficiently fine interpolation, the dots run together and result in contour lines. The routine is quick,

simple to program and removes the possibility of bias in the positioning of contour lines.

Chapter 3

ELECTRON NUMBER DENSITY DISTRIBUTION IN THE ICP

3.1 INTRODUCTION

The key defining parameter in the LTE description of the plasma presented in this work is the electron density (n_e). Therefore, spatially resolved electron densities were measured under a variety of plasma conditions to provide a complete n_e description of the ICP itself.

Many authors have measured electron densities or concentrations in the ICP [25,52,53,55,63,67,69,83-85]. The general result of these studies is that the plasma electron density is in the range of $1.0 \times 10^{14} cm^{-3}$ to $5 \times 10^{15} cm^{-3}$. Typically, these measurements represent effective electron densities or, if radially resolved, are only for one vertical height above the load coil. Recent literature on plasma excitation mechanisms has pointed out the need for comprehensive electron concentration maps of the ICP [17,73]. Electrons are most likely the species responsible for excitation in the plasma and a number of papers [61,73] have advocated the use of n_e as the basis of an LTE model of the ICP. In addition, rate model calculations, such as those of Lovett [36] and Haraguchi [35], require an accurate value for electron density to enable the calculation of rate constants for most collisional-radiative processes. The need for accurate and precise experimental measurements of electron density over a wide range of ICP operating conditions is obvious. Comprehensive spatially resolved electron density maps of the ICP have been presented by only a

few authors [35,86,87] and then only very recently.

Several spectroscopic approaches to the measurement of electron density in the ICP are commonly utilized. The Saha-Eggert ionization equilibrium method is based on measurements of relative intensities of neutral atom and single ionized species of the same species and substitution of this ratio into a Saha equation along with a temperature. The question that immediately arises is which of the many temperatures measured in the ICP is to be used for this calculation. Typically, an excitation temperature is used and the resulting electron densities differ from values determined from other methods by one to two orders of magnitude [67,88]. This method is based on the assumption of LTE in the source. The errors introduced in the derived n_e from inaccuracies in transition probabilities or experimental error in temperature determination are negligible compared to the error in using an LTE method to determine a parameter in a source that has been clearly shown not to be in LTE. A second method is based on the measurement of the absolute continuum intensity. There is only a weak dependence on the assumed electron temperature ($n_e \sim T_e^{1/4}$) and electron density values obtained are consistent with those from other methods [35,69,88]. Montaser and co-workers [83,84] use series limit line merging to measure n_e. The technique is based on the fact that as the principal quantum number increases, the wings of the Stark-broadened lines start to overlap each other until finally, before reaching the series limit, the lines merge completely, forming a continuum. The principal quantum number at which this merging occurs, depends on n_e. The chief objection to this technique is that the "last

discernible" line is not precisely defined [89,90].

By far the most widely utilized method is Stark broadening of spectral lines, particularly those emitted by argon or hydrogen. Electron densities determined in this manner are largely independent of the temperature of the plasma and of any assumptions about the existence of LTE. Stark broadening theory is well developed and extensive tabulations of Stark parameters exist for a number of lines [91,92]. Atomic hydrogen lines are most frequently used because of availability of data and the fact that the theory is more accurate than for multielectron atomic species [93,94]. The line of choice in a dense plasma containing hydrogen is H_β [95]. It is a strong, distinctive line in an easily accessible region of the spectrum (486.13 nm) which is relatively free from spectral interference from other plasma components. The range of half-widths ($\sim$ 0.1 to 0.5 nm) for typical electron densities in the ICP is sufficiently large to allow precise measurements of n_e. The experimental procedure can be somewhat laborious since a measurement of the intensity distribution over the line profile and the determination of the background level of the adjacent continuum is necessary. In order to achieve radial measurements via an Abel inversion this procedure must be carried out at a number of lateral positions across the plasma. Furthermore, the experimental line profiles must be deconvoluted from other sources of line broadening.

Electron densities were measured by Stark broadening of the H_β line and in a later chapter by broadening of argon lines. The results presented have appeared in previous publications [75,76,96]. The measurement of the electron density represents a

major portion of this thesis. As such, a brief review of line broadening in plasmas, line profiles, and deconvolution of line profiles follows.

3.2 Theoretical Concepts

3.2.1 Line Broadening in Plasmas

The broadening of spectral lines is a complicated function of the environment of the radiating atoms or ions, and depends on both pressure and temperature. The measurement of line profiles combined with an adequate theory represents therefore an attractive non-invasive probe for plasma diagnostics [95].

A spectral line emitted by a source is not a quantum of sharply defined frequency, but exhibits both breadth and shape. The mechanisms which contribute to the line shape may be broadly classified:

1)Natural line broadening is a consequence of spontaneous emission. It is linked to the radiative lifetime through the Heisenberg uncertainty principle. Its contribution to the half width of a line is normally of the order of 0.0001 nm and can be ignored in comparison with other contributions.

2)Pressure broadening is due to the effects of interactions with neighboring particles. It can be divided into three types-

i) Lorentz or Van der Waals broadening that results from collisions with unlike neutrals.

ii) Holtzmark broadening that results from collisions with like atoms.

iii)Stark broadening which is due to interactions with charged particles.

3)Doppler broadening is the result of random thermal motion of the emitting atoms. For a purely Doppler broadened line the full width half maximum, (FWHM) which is the width between the two half-maximum intensity points, is

$$\Delta\lambda_{1/2}{}^{D} = 7.16 \times 10^{-7} \lambda (T/M)^{1/2} \qquad (3.1)$$

where λ is wavelength in nm, T temperature in K and M molecular weight. The $\Delta\lambda_{1/2}{}^{D}$ is in nm. Thermal Doppler broadening is most pronounced for lines of light elements at high temperatures.

The two dominant causes of line broadening in plasmas are the Doppler effect and the interatomic Stark effect. Line profiles emitted by atoms or ions, embedded in a dense gas or plasma, will be predominantly determined by interactions of the emitter with surrounding particles, i.e. pressure broadening. In plasmas which are sufficiently ionized, about 1 %, the long range Coulomb forces are dominant, and only broadening caused by charged particles is important [95].

Stark broadening arises from the perturbation of the energy levels of an emitting (or absorbing) species by an electric field. The electric field is a consequence of the motions and concentration of surrounding charged particles. Stark broadening theory has been developed from two very different points of view, which are extreme approximations of a more general theory. In the impact theory the wave train of light emitted from an atom is perturbed by fast impacts. Whereas, in the quasi-static approximation, the perturbing particles are assumed to move so

slowly during the time of emission that the perturbing field may be thought of as quasi-static. These two extreme approximations may each be appropriate for the two different kinds of perturbers in a plasma - the impact approximation with its sudden encounters for the fast moving electrons and the quasi-static theory for the heavy, slowly moving ions [95]. The Stark broadening theory developed by Griem and co-workers [93,94,97,98] simultaneously takes into account the broadening by ion and electrons. On the basis of this theory extensive tabulations of line profiles for hydrogen lines and Stark half-width and shift parameters for the heavier elements have been published [91,92]. Refinements to the theory for hydrogen by Kepple and Griem [98] and Smith et al. [99] have led to significant improvements in agreement between experimental and theoretical line profiles. Stark broadening theory has been developed to a level of sophistication where the measurement of the half-width of a Stark broadened line is now one of the most accurate ways to determine electron density in a plasma [95].

The theory and application of Stark broadening methods for the determination of n_e in plasmas has been reviewed in a number of publications [91,92,95,100] and a more detailed discussion is beyond the scope of this work.

3.2.2 Line Profile

The observed optical profile of a line is the result of the superimposing of the instrumental line contour on the physical line contour. The physical profile is the shape the line has due

to the physical conditions in the source of excitation and is the product of several simultaneously acting line broadening mechanisms. The instrumental profile is the pattern that results from the influence of spectrographic equipment on a uniform intensity distribution. From the standpoint of a particular line broadening theory, i.e. Stark broadening, the experimental profile appears distorted by these other broadening mechanisms. Their contribution to the line profile must be removed before plasma parameters can be calculated from the theory in question.

Line broadening mechanisms typically act independently so they can be considered to be superimposed on one another. The combination is given by a 'folding' or convolution integral over the line profile. The application of this folding process in its general form to corrections of line profiles and widths is complex. Fortunately, line profiles resulting from most broadening mechanisms can be described by analytical functions without any significant loss of precision. The natural and Lorentz profiles can be represented mathematically by a dispersion function, $1/(1+x^2)$, while the Doppler profiles follow a Gaussian distribution, $\exp(-x^2)$. Except for hydrogen and some helium lines the line shape factor resulting from Stark broadening is approximately Lorentzian. The Gaussian and Lorentz profiles combine to form an intensity distribution given by the Voigt function. These are available in tabular and graphical form. The evaluation of electron density is concerned only with the half-width of the profile and the table of Davies and Vaughan [101] provides a convenient means of converting the experimental Voigt half-width into its Doppler and Gaussian components.

Simple relations also exist for the combination of two Lorentzian profiles or two Gaussians. The folding of two Lorentzian shapes produces a Lorentzian profile with a half width equal to the sum of the two half widths. The folding of two Gaussian shapes results in a Gaussian profile with a half width equal to the root of the sum of the squares of the individual widths [95].

An additional problem encountered in the measurement of line profiles to perform plasma diagnostics is that of significant line broadening due to the finite instrumental resolution. The apparatus function must first be determined experimentally, this is usually done by scanning over a line of negligible width (in comparison to apparatus width). Line emission from low-pressure discharges is very suitable. The instrumental line profile of grating spectrometers is typically Gaussian in the center with a change over to a Lorentzian profile only in the far wings [102]. Thus for most applications the Gaussian function is a good approximation to the instrumental line profile.

3.3 EXPERIMENTAL PROCEDURE FOR MEASUREMENT OF ELECTRON DENSITY

The gas flows used for all measurements were 11 1 m^{-1} plasma gas, 0.3 1 m^{-1} auxiliary gas and 0.9 1 m^{-1} aerosol flow unless otherwise indicated.

Electron densities were evaluated from the Stark broadening of the H_β line at 486.13 nm. A representativespectrumof the wavelength region from 480 to 490 nm is presented in Figure 7. The H_β line is readily identifiable by its distinctive central dip and significant width. The decomposition of water nebulized

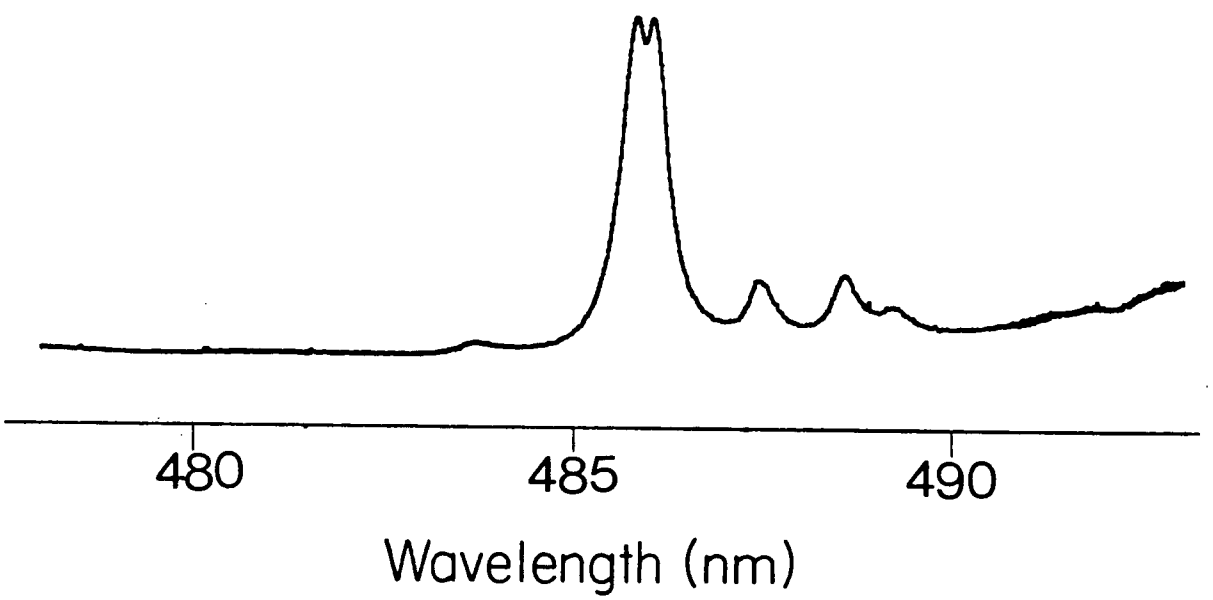

Figure 7 Typical spectrum of H_β line at 486.13 nm.

into the plasma provides a sufficient concentration of hydrogen for the measurement of electron density.

To obtain spatially resolved radial electron density values, at a particular vertical height above the load coil, the H_β line at 486.13 nm was simultaneously sampled at 40 wavelength points across the line profile for 150 lateral positions across the discharge. The acquisition of these 6000 data points took approximately 30-60 minutes, depending of the integration time used. This rapid data acquisition was possible through the combination of the photodiode array detector and translation stage under computer control. At each lateral position, the plasma background was subtracted by interpolating from the continuum emission measured on both sides of the H_β line 3.0 nm from the line center. The 150-point lateral profiles for each wavelength position were fitted with 15 separate, overlapping 3 rd-order polynomials, and an interpolation performed to obtain smooth lateral wavelength profiles. The smoothed lateral data was Abel inverted using the numerical method of Nester and Olsen [79]. This required 40 Abel inversions for each vertical height. For each of the resulting 150 radial points the H_β profile was reconstructed from the Abel inverted wavelength data and the experimental radial full width at half maximum for each radial position evaluated.

The resulting radial experimental half-width was corrected for both Doppler and instrumental line broadening. The instrumental line profile was evaluated by placing a low pressure mercury discharge lamp in the place of the plasma torch and the half widths of the HgI 435.8 and 408.6 nm lines were recorded. An

instrumental line profile halfwidth of 0.114 nm was observed for the 1024 photodiode array and 0.3 m monochromator for entrance-slit dimensions of 50 x 1000 μm. The instrumental function was assumed to be Gaussian.

The Doppler profile should also be deconvoluted from the half width before the calculation of electron density. However, the hydrogen profiles presented in the Stark-Broadening tables of Vidal et. al [103] already contain the Doppler contribution and so $n_e(r)$ can be calculated directly from the following expression

$$n_e(r) = 7.9658 \times 10^{12} \, (\Delta\lambda_{1/2}(r)/\alpha_{1/2})^{3/2} \qquad (3.2)$$

where $\Delta\lambda_{1/2}(r)$ = the radial full half width of the H_β line after deconvolution of the instrumental half-width in angstroms

and $\alpha_{1/2}$ = reduced half width parameter from reference 103

The reduced half width parameter, $\alpha_{1/2}$, is a function of both the temperature and electron density. Thus, the iterative procedure described by Kalnicky et al. [67] was used for calculating final $n_e(r)$ values.

3.4 PRECISION AND ACCURACY OF ELECTRON DENSITY MEASUREMENT

3.4.1 Accuracy of Stark Parameters

A recent publication [102] compares the theoretical line profiles determined for the hydrogen Balmer lines from two advanced Stark broadening theories with experimental results. One theory was the unified theory of Smith, Cooper, and Vidal [99] whose Stark broadening tables [103] were used in this work and the other was the generalized impact approximation of Kepple and

Griem [98]. For H_β, the agreement between measured and experimental intensities was quite good. The chief discrepancy occurs at the line center where both theories overestimate the magnitude of the central minima. Good accuracy and consistency exists for the 1/2, 1/4 and 1/8 widths for the H_β line. The half-width data of Vidal et al. [103] yield electron densities which differ from independently measured values by +9% (at the smallest n_e) to -1% (for the largest n_e) over the range 1.5 - 10 X $10^{16} cm^{-3}$. The profiles of Kepple and Griem slightly underestimate the electron density (-4% to -10%). The authors conclude it is best to use detailed line profile measurements for determinations of n_e by Stark broadening particularly when using hydrogen lines other than H_β. For H_β, the line profile calculations of Vidal et al. [103] are the most accurate and should yield electron densities accurate within 10%.

3.4.2 PRECISION OF ELECTRON DENSITY MEASUREMENT

To test the precision of the measurement of electron density by Stark broadening of the H_β line, ten measurements of the n_e radial profile were done at 12 mm above the load coil for an rf input power of 1.25 kW. The measurements were made on three separate days over a period of a week. The 10 resulting radial electron density profiles are plotted in Figure 8. The calculated n_e have very good agreement off the plasma axis and exhibit somewhat more scatter at the edges of the plasma and in the plasma center. Figure 9 is a plot of the percent relative standard deviation versus radial distance from the plasma center of the 10 measurements. At the plasma center the relative

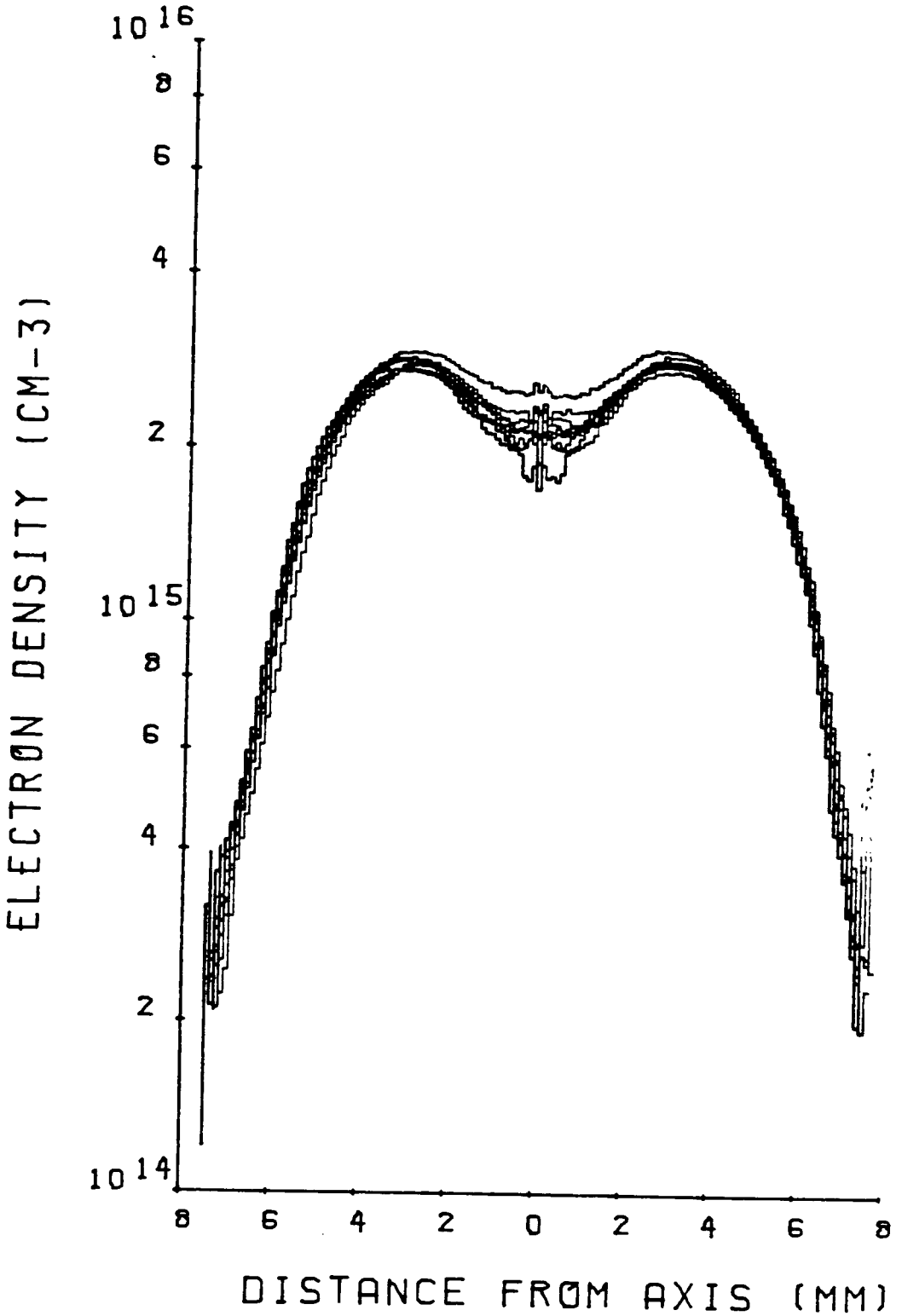

Figure 8 Ten replicate measurements of electron density as function of radial distance. Height 12 mm above load coil, power - 1.25 kW.

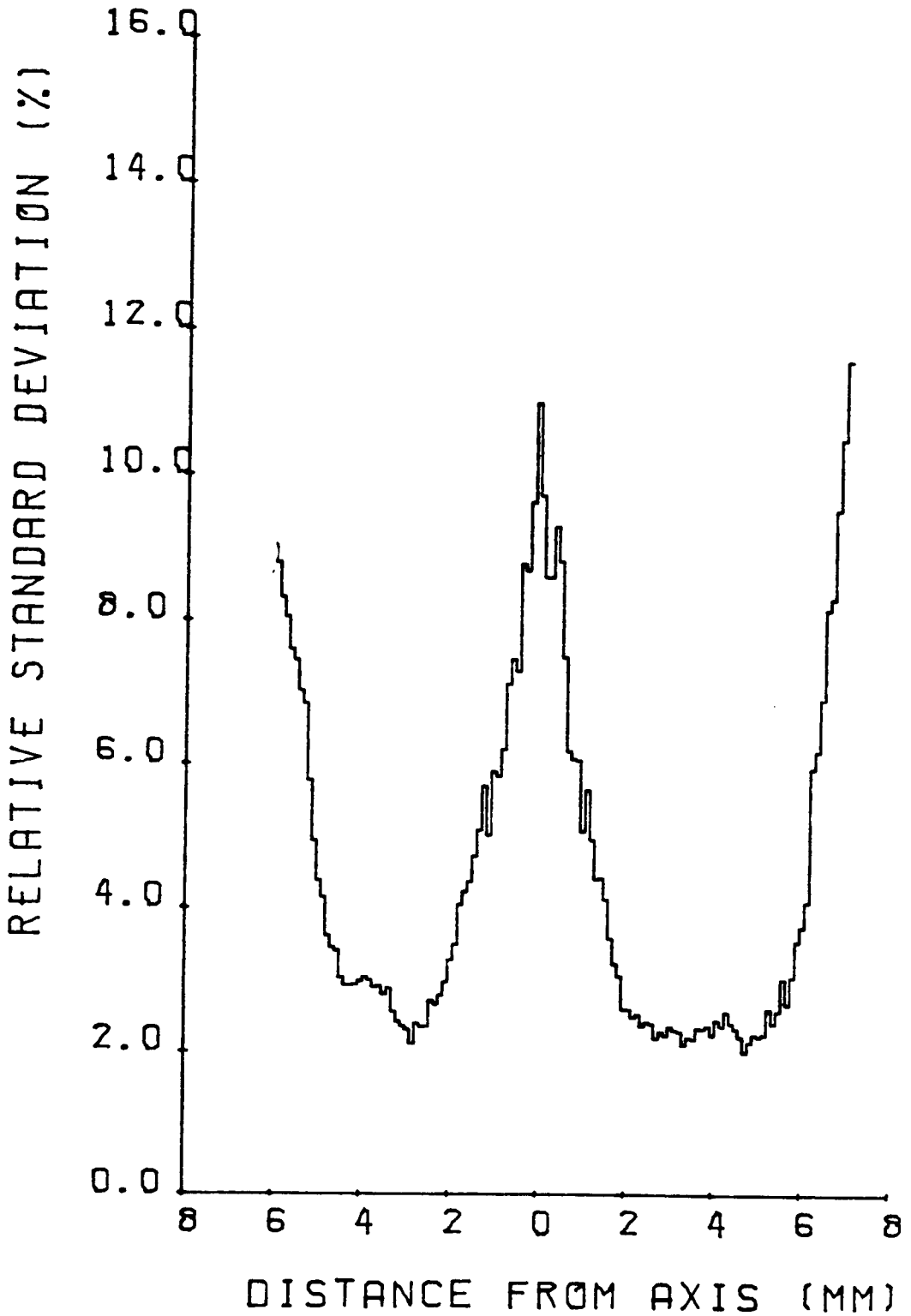

Figure 9 Relative standard deviation for the set of data in Figure 8.

standard deviation (one sigma) is 10%, it decreases to about 2% at 2-5 mm radial distance and increases rapidly at the periphery of the discharge.

The large variance at the center is thought to be due to errors in the Abel inversion, in particular, problems associated with the choice of an appropriate center of the lateral input data. Calculations in Section 2.4 indicate errors of this magnitude are to be expected in the Abel inversion of experimental data.

3.5 RESULTS

3.5.1 SPATIAL DISTRIBUTION OF ELECTRON NUMBER DENSITY

Radially resolved electron density values evaluated from Stark broadening of the H_β 486.13 nm line for five vertical heights above the load coil at an rf input power of 1.25 kW are presented in Figure 10. Figures 10(i), 10(ii), 10(iii), 10(iv) and 10(v) correspond to the vertical heights: 4, 8, 12, 16, and 20 mm above the load coil respectively.

The complexity of the spatial structure of n_e in the ICP is apparent in these figures. The electron concentration exhibited a minimum in the aerosol channel and rose sharply at increased radial distances for a vertical height of 4 mm above the load coil. In fact it was at 4 mm that both the maximum and minimum in electron concentration occurred. At intermediate heights, 8, 12,and 16 mm above the load coil, the magnitude of the off axis maximum decreased while the central channel value increased. The profiles of electron density across the plasma became progressively flatter. At 20 mm above the load coil there was

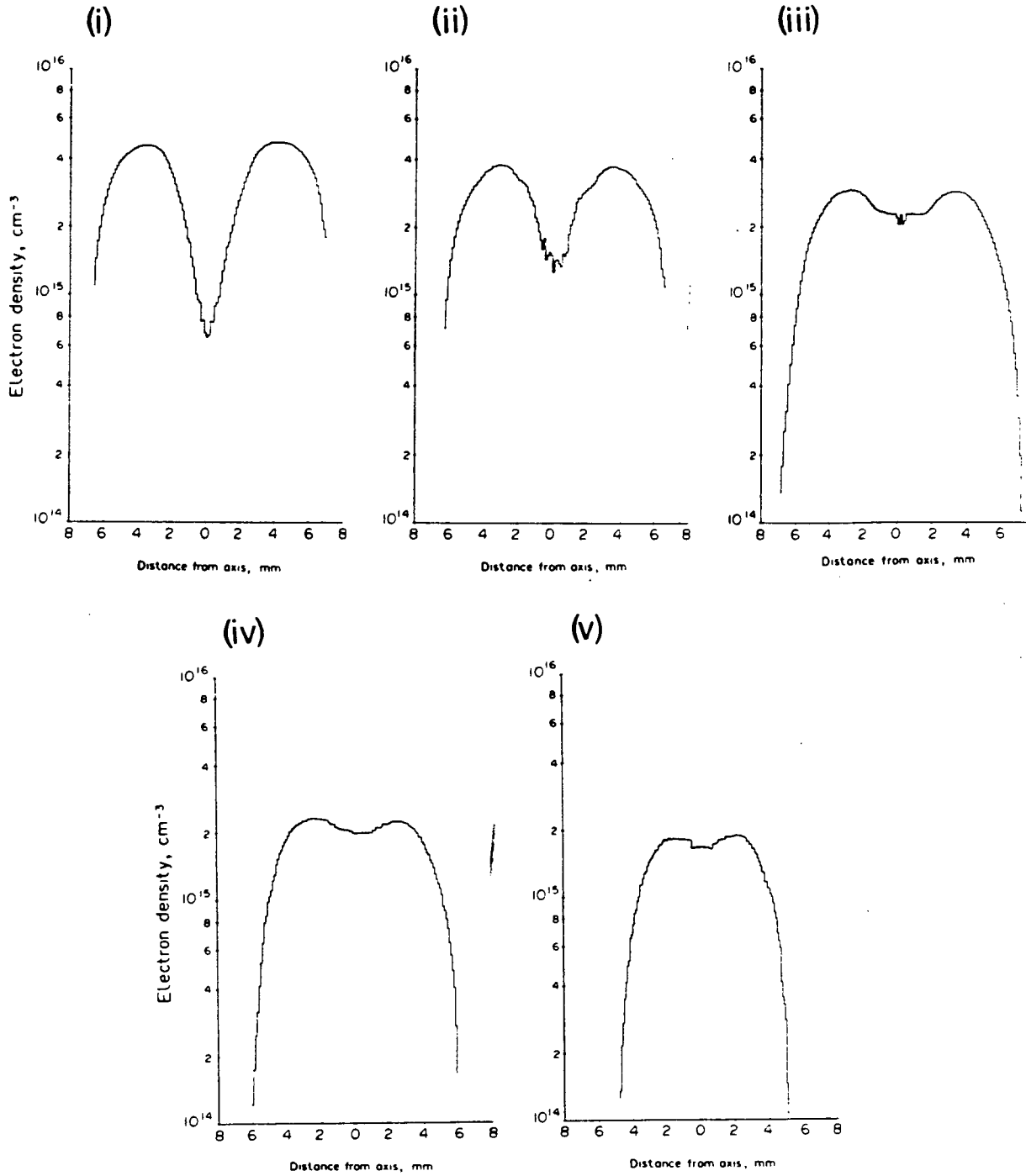

Figure 10 Spatially resolved electron density plot for input power of 1.25 kW at vertical heights of (i) 4 mm, (ii) 8mm, (iii) 12 mm, (iv) 16 mm and (v) 20 mm above the load coil.

almost no central dip in the n_e profile and it was better described as bell shaped with a central maximum.

The electron density distribution follows a distinct pattern. It maximized in the induction region of the plasma where energy is coupled in to the plasma from the load coil. Low in the central channel where the cold aerosol gas is first introduced n_e is at a minimum. As the aerosol gas is heated by contact with the hot annular gas in its passage up the plasma, the electron density increases, until at 12 to 16 mm above the load coil it peaks and decreases after this. This pattern is the same as that shown by analyte emission in the ICP, which in general increases with height above the load coil and shows a peak intensity in the NAZ about 12 to 16 mm above the load coil [62,104].

These radial n_e plots also indicate the need for Abel inverted n_e data to fully understand the plasma. If lateral electron density values are measured, at the low heights one would observe an effective electron density value which would be a sort of average between the high n_e in the annular region and the low n_e in the central channel. At intermediate heights above the load coil the n_e observed would be smaller in magnitude although the electron concentration in the central channel would have actually increased. The result would produce an impression that electron density decreases with increasing height in the plasma. This profile would be very difficult to reconcile in mechanistic terms with the observed profiles of analyte emission.

To aid in visualization of the distribution of electron density in the ICP, an isocontour plot of n_e was prepared. The radial electron densities at the 5 heights were integrated to

produce the isocontour plot presented in Figure 11. This contour plot, and all subsequent ones presented, were computer generated using a contour plotting routine, CONDOT, published by Simons Jr. [82]. The density values of the isocontour lines are given in units of $10^{15} cm^{-3}$. The maximum electron concentration occurred at 4 mm above the load coil in the annular region of the discharge and rapidly decreased toward the center of the plasma or the plasma edge. In the central channel there was a region of very low electron density. A generally similar horizontal pattern was observed at all heights above the load coil but a shift of electron density towards the plasma center with increasing observation height occurs. Along the central axis, the electron number density increased with distance from the load coil until about 12 mm above the load coil. From about 12 to 18 mm above the load coil n_e was rather uniform over a large part of the plasma.

The spatial distribution of electron density observed is very similar to that reported by other workers [35,86,87]. The actual magnitudes of the electron densities agree very well between this work and that of Furuta et al. [86] and Hasegawa and Haraguchi [35]. These researchers used an input power of 1.1 kW and an aerosol flow rate of 1.0 l m^{-1}, plasma conditions similar to those utilized in this work. Furuta et al. [86] observed much lower electron concentrations in the central aerosol channel probably due to the much better resolution of their spectrometer.

3.5.2 EFFECT OF RF INPUT POWER ON ELECTRON DENSITY

Radially resolved electron density profiles were measured for 4, 8, 12, 16, and 20 mm above the load coil at input powers

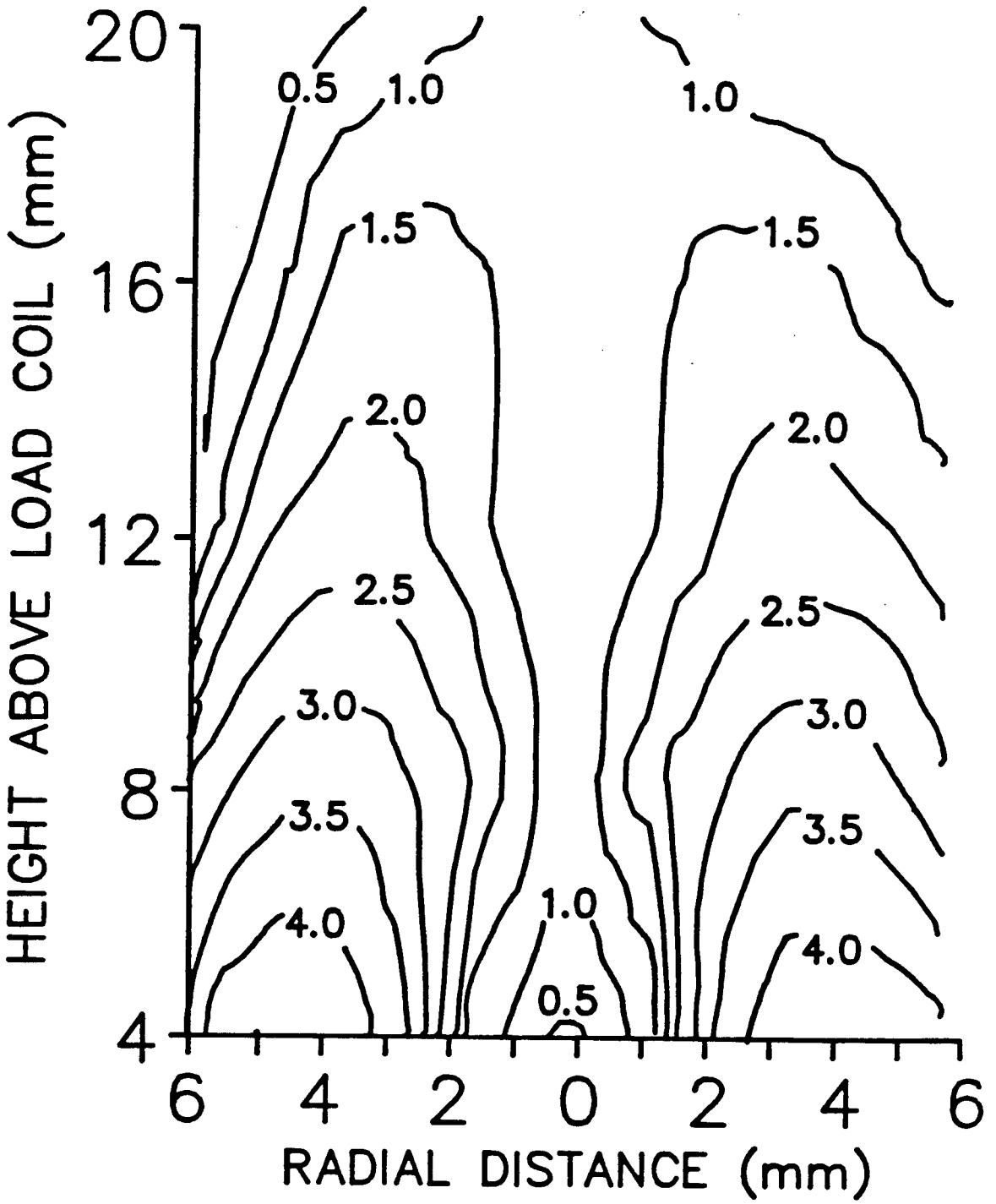

Figure 11 Electron density isocontour plot at an rf input power of 1.25 kw. Density values of the isocontour lines in units of $10^{15}_{cm^{-3}}$.

of 1.00, 1.50, 1.75, and 2.00 kW. The radial electron densities at the 5 heights for each power setting were integrated to produce isocontour plots of electron density. These are presented in Figures 12(i), 12(ii), 12(iii) and 12(iv) for the input powers of 1.00, 1.50, 1.75 and 2.00 kW, respectively.

The change of n_e with spatial position is similar for all input powers. There was a tongue about 2 mm wide of low electron density in the central aerosol channel that extended from 4 mm above the load coil up to about 12 mm. The highest electron density was ± 4 mm from the center, just above the load coil and decreased with increasing height.

Increasing the input power resulted in a corresponding increase in electron concentration at all vertical heights observed. The electron density at 1.00 kW differs from that a 2.00 kW by almost an order of magnitude. Aeschbach [105] has demonstrated that rf power is one of the key factors in determining the magnitude of electron concentrations.

Choot and Horlick [87] report spatially resolved electron density for rf input powers of 1.5 kW and 2.0 kW. The agreement between their results and the ones presented in this thesis is truly remarkable. At any given spatial position in the discharge there is less than 10% difference between the two sets of measurements.

3.5.3 EFFECT OF AEROSOL FLOW RATE ON ELECTRON DENSITY

Another parameter judged to have an important effect on electron density is aerosol flow rate. Spatially resolved measurements of electron density at three different aerosol flow

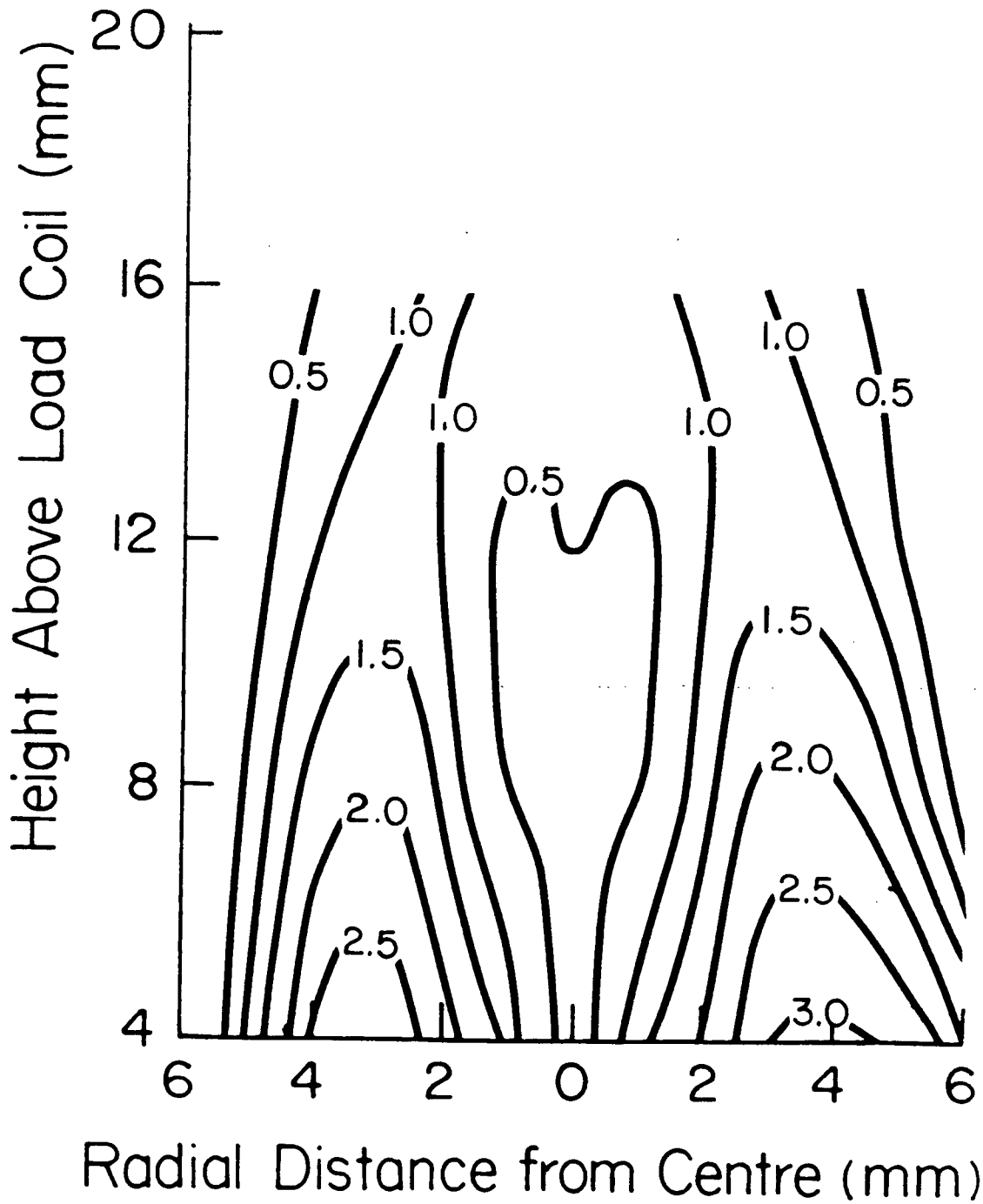

Figure 12(i) Electron density isocontour plot at rf input powers of 1.00 kW. Density values of the isocontour lines in units of 10^{15} cm-3.

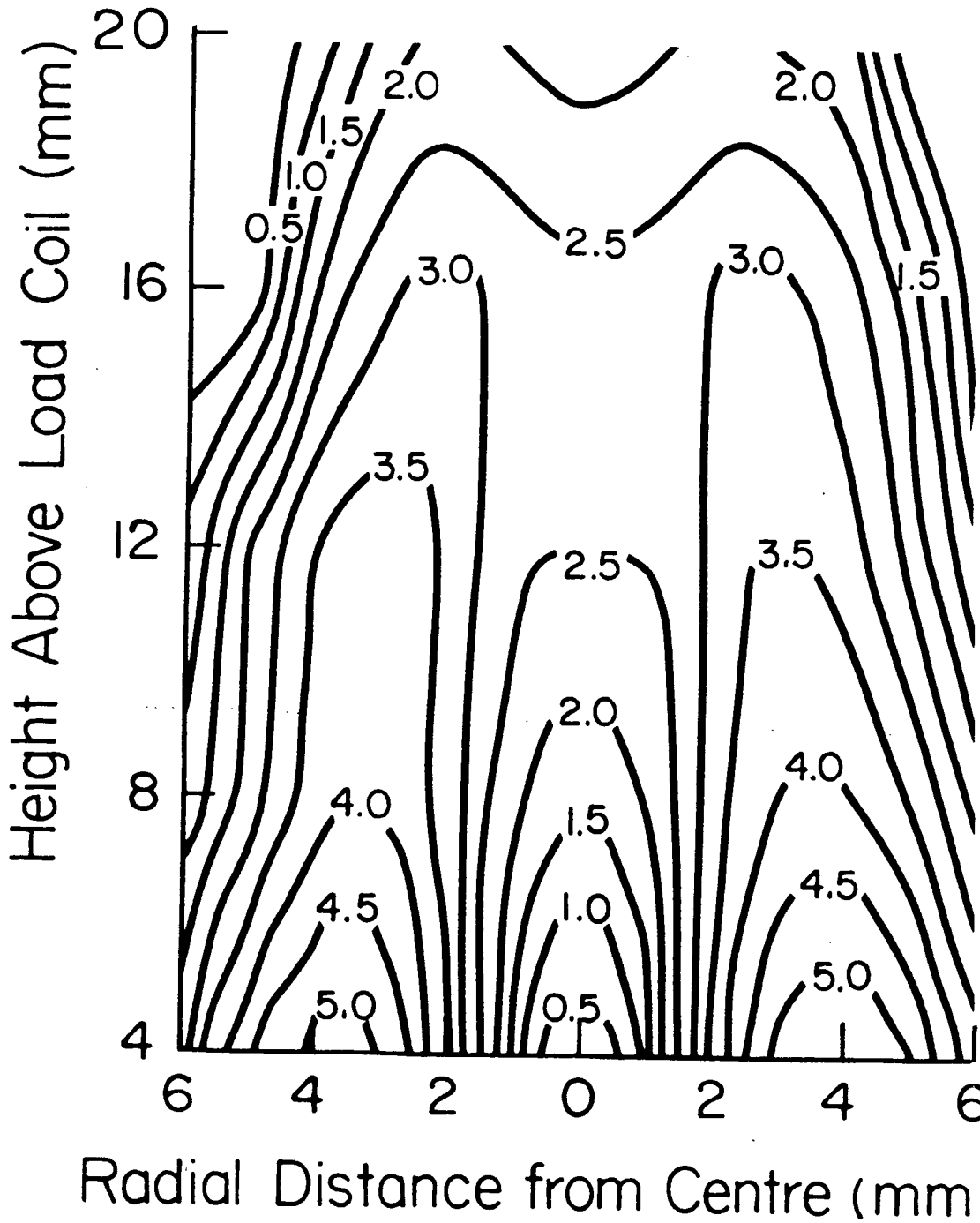

Figure 12(ii) Electron density isocontour plot at rf input powers of 1.50 kW. Density values of the isocontour lines in units of 10^{15}_{cm-3}.

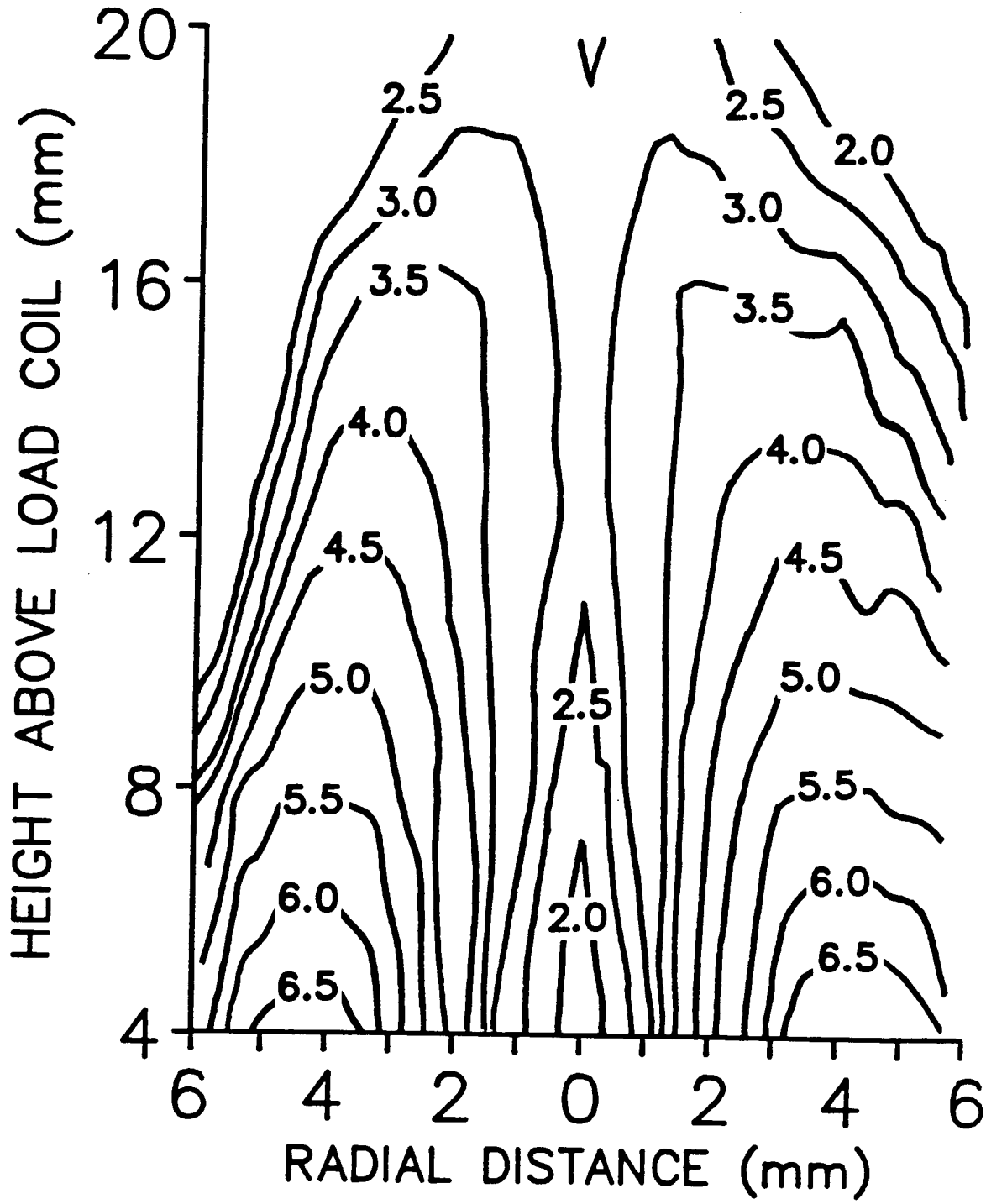

Figure 12(iii) Electron density isocontour plot at rf input powers of 1.75 kW. Density values of the isocontour lines in units of 10^{15} cm-3.

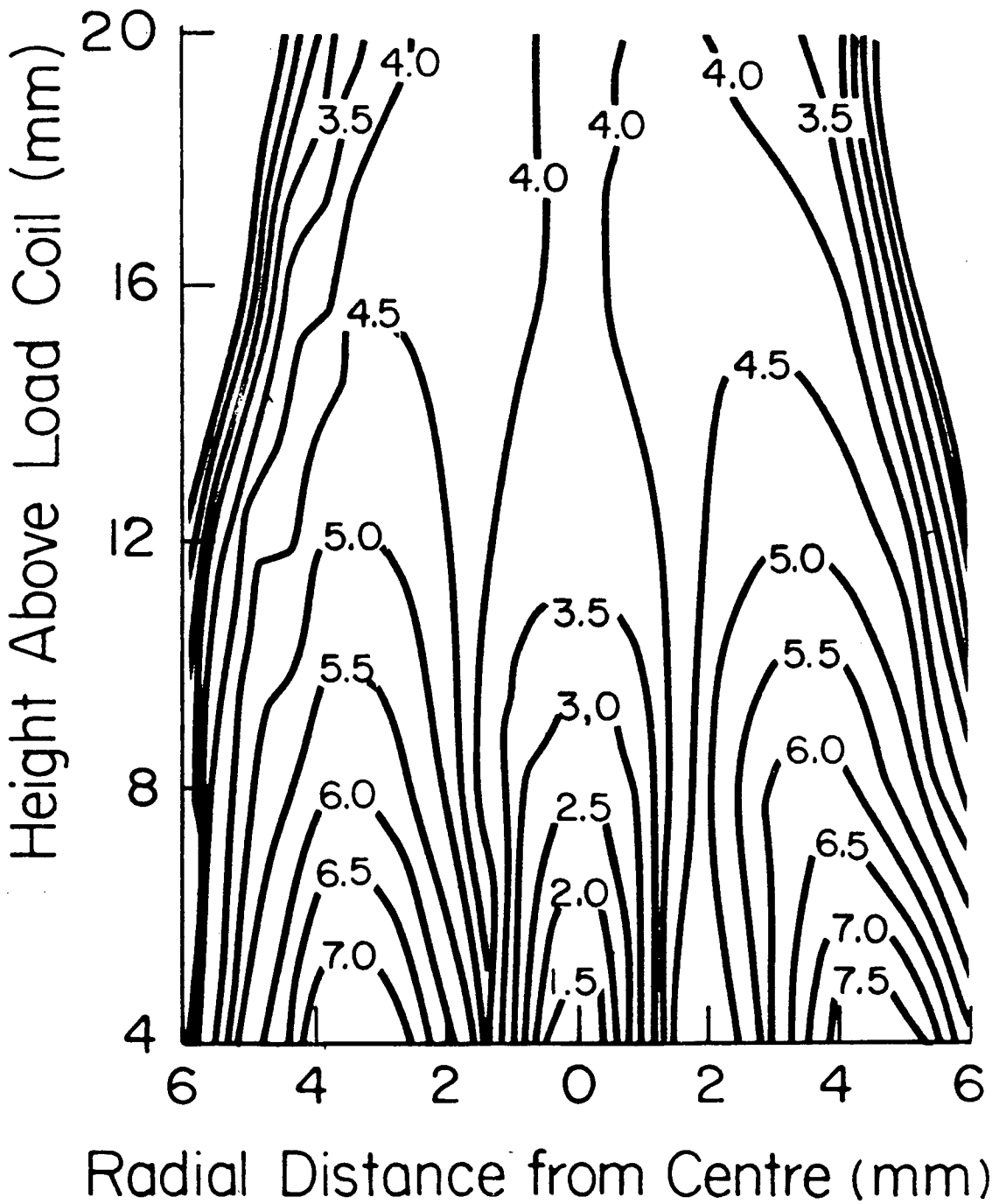

Figure 12(iv) Electron density isocontour plot at rf input powers of 2.00 kW. Density values of the isocontour lines in units of 10^{15} cm-3.

rates were made. Figures 13(i), 13(ii) and 13(iii) are the electron density contour plots at an rf input power of 1.25 kW for aerosol flow rates of 0.6, 0.8 and 1.2 1 m^{-1} respectively.

The n_e contour plots at the high and low flow rates have some interesting features. At 0.6 1 m^{-1} there was a large region of moderately high electron density - between 3.5 and 3.0 x $10^{15} cm^{-3}$ extending from ± 3 mm from the plasma center from 4 to 14 mm above the load coil. The electron density in the central channel decreased with increasing height above the load coil.

For 0.8 1 m^{-1} the electron density distribution had the pattern shown in the previous contour plots of n_e. The electron density profile in Figure 13(ii) is very similar to Figure 11. The input power of 1.25 kW was the same and the flow rates used, 0.8 1 m^{-1} and 0.9 1 m^{-1}, respectively, are very similar so this result is to be expected.

At an aerosol flow rate of 1.2 1 m^{-1} there was a large region in the aerosol channel, ± 2 mm from the central axis, characterized by low values of electron density, less than 0.5 x $10^{15} cm^{-3}$. The instrumental line width of this system prevented the measurement of n_e below 0.5 x $10^{15} cm^{-3}$. In essence the relatively high aerosol flow rate blew a hole through the center of the plasma.

Since all three electron density contour maps were collected at the same rf power one would expect the lower annular region to have more or less similar values [105]. The plots provided in Figure 13 confirm this, the maximum electron density observed in the annular region of the plasma is very similar for all three aerosol flow rates. The vertical spatial distribution of n_e can

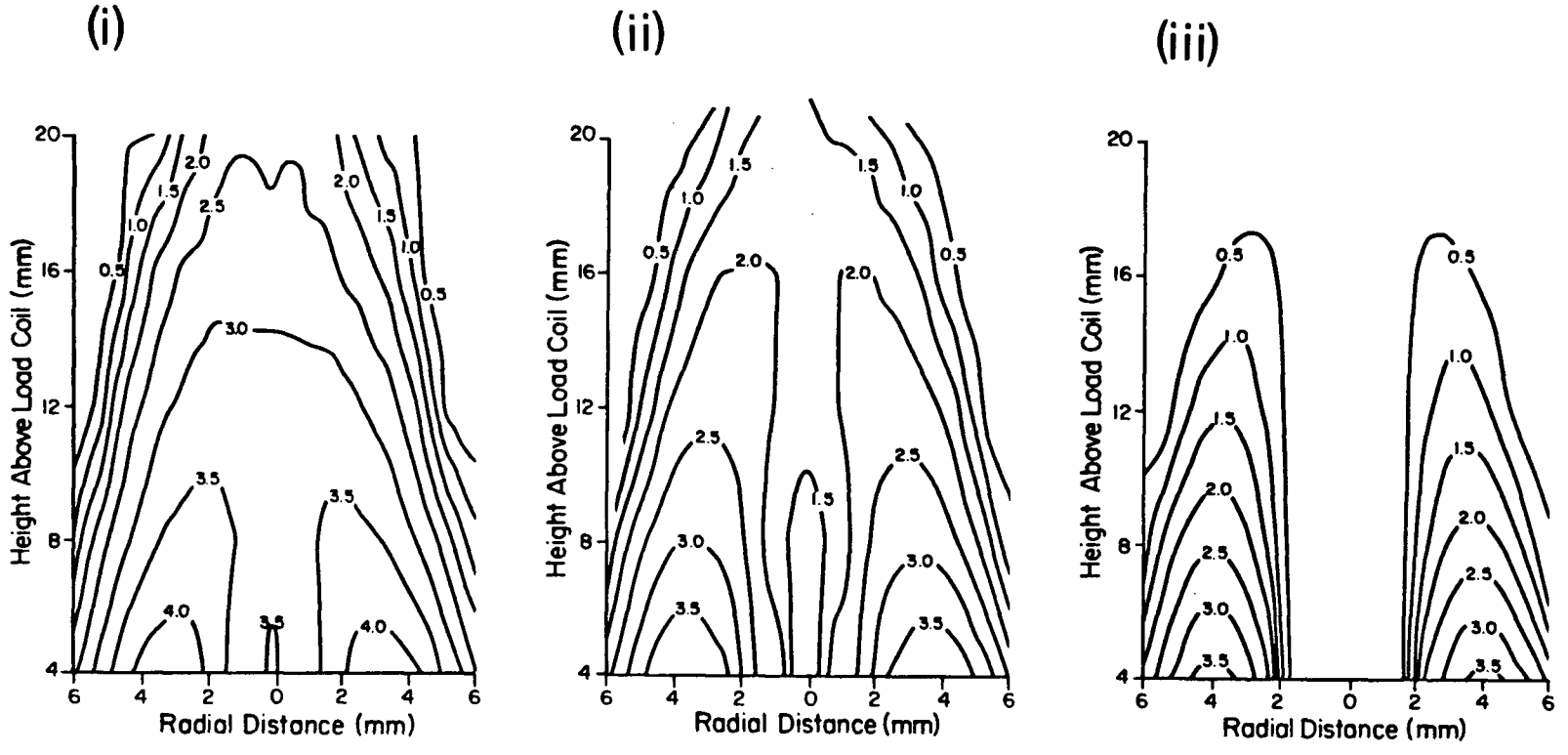

Figure 13 Electron density isocontour plots for an rf input power of 1.25 kW. Aerosol flow rate - (i) 0.6 l m^{-1}, (ii) 0.8 l m^{-1} and (iii) 1.2 l m^{-1}. Density values of the isocontour lines in units of $10^{15} cm^{-3}$.

be understood in terms of a simple vector model of electron diffusion in from the annular region and transport up the plasma due to the aerosol flow rate. Electrons from the annular region diffuse toward the analyte channel essentially horizontally. At the interface between the aerosol channel and annular region they experience a vertical force caused by the aerosol gas flow, which acts to carry them in the vertical direction preventing mixing with the aerosol channel. The addition of the horizontal and vertical components yield a net rate of electron migration from the annular region into the center of the channel, i.e. the resultant vector has an angle with respect to the horizontal. The greater the aerosol flow rate the larger this angle is, and this moves the vertical position where electron concentration maximizes along the central axis of the plasma.

3.5.4 EFFECT OF EASILY IONIZABLE ELEMENTS ON ELECTRON DENSITY

Several possible mechanisms have been postulated for the effect of easily ionizable elements (EIE) on analyte emission intensity [104,106-109]. In a recent paper Faires et al. [107] found that for equimolar concentrations of matrix elements, the EIE of lowest ionization potential produces the largest enhancement effect on the analyte emission. This suggests the interference mechanism may be related to an increased electron concentration from the easily ionizable element in the plasma.

Electron density has previously been measured in the plasma with and without the addition of an EIE [67]. The reported results show no appreciable change in n_e with the addition of EIE when the measurement is made by Stark broadening of either H_β

or argon. However, the radial measurement was made at 15 mm above the load coil where the effect of an EIE is at a minimum [104]. The reported measurements at 2 and 5 mm above the load coil are from effective half widths of the Stark broadened lines, thus changes in the central channel could have been masked by off-axis emission. The measurements in a recent paper by Prell et al. [109] indicating an increase in electron density with the addition of an EIE are flawed. The presence of easily ionizable elements could affect ion-atom emission intensity ratios without changing the electron density. Thus the substitution of a changed ion-atom ratio into the Saha equation does not indicate an change in electron density.

To investigate the effect of an EIE on radial profiles of electron density, n_e was measured at 4 mm above the load coil for a distilled water solution containing 0.5 M Cs (6250 mg l^{-1}). The results are presented in Figure 14 for an input power of 1.25 kW and an aerosol flow rate of 0.9 l m^{-1}. The solid line is the electron density from the Cs solution. The dashed lines represent the $\pm 2\sigma$ limits of the electron density without any Cs present. No significant difference was found at all radial positions. Measurements at heights of 8, 12, 16, and 20 mm above the load coil with and without Cs also showed no difference in the n_e profile.

This is not definitive proof that easily ionizable elements do not effect the electron density. The resolution of the measurement system was such that evaluation of electron concentrations below $5.0 \times 10^{14} cm^{-3}$ was not possible. EIE could cause changes in n_e low in the central aerosol channel where the

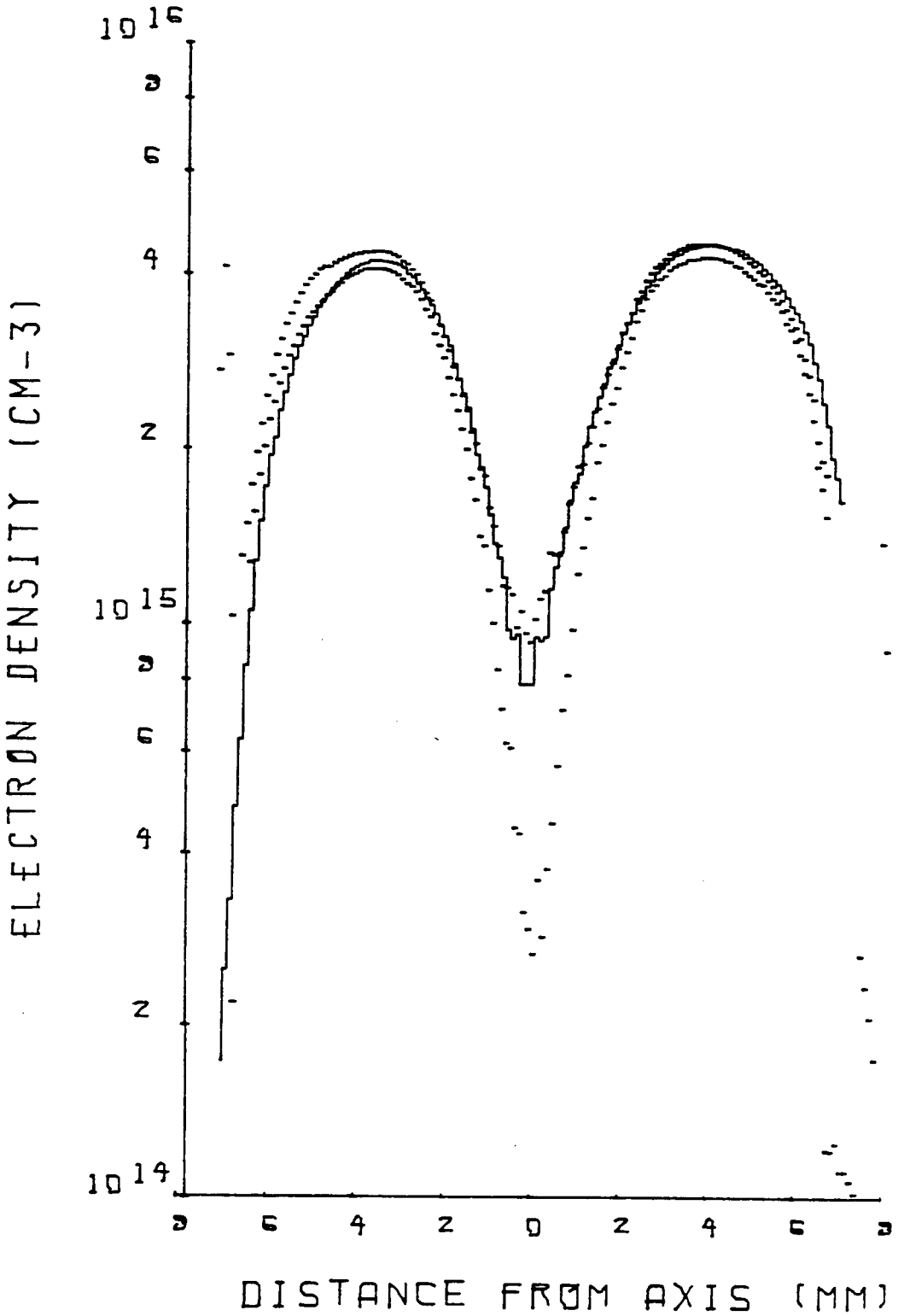

Figure 14 Electron density profile at 4 mm above the load coil and 1.25 kW rf input power. Solid line - with 0.5 M Cs nebulized; dotted line - ± 2σ limits for distilled water nebulized.

overall electron density is below the instrument detection limit. As well, the effect of easily ionizable elements on electron concentration may be less than the precision of the measurement.

3.5.5 EFFECT OF HYDROGEN IN THE PLASMA GAS ON ELECTRON DENSITY

Measurements of electron density in the ICP by Stark broadening of hydrogen lines typically utilize the aspirated water as a source of hydrogen. This is a near ideal situation because the evaluation of n_e can be done under normal operating conditions. Often, though, it is desirable to determine electron densities for cases in which water is not being aspirated into the plasma in order to understand the effect of variables such as aerosol gas or water in the aerosol gas. In these cases, if the convenient and reliable method of determining n_e by Stark broadening of H_β is to be used, an alternative source of hydrogen must be found. One approach is to admix a small amount of hydrogen with the argon plasma gas [95]. Ideally this small amount of hydrogen will behave only as a probe and not alter plasma conditions. Unfortunately, this goal is often not realized in practice.

Batal et al. [57] assessed the effect of a binary mixture of argon-hydrogen (0.3% in H) on plasma excitation conditions for a 40 MHz plasma. The substantial increase in n_e over that observed in a pure argon plasma was attributed to the thermal pinch effect. There are often considerable differences in behavior between 40 and 27 MHz plasmas [110] and for this reason the effect of a small amount of hydrogen on electron density in the 27 MHz ICP was measured.

For this study argon gas containing 0.5% (w/v) hydrogen was used as both the plasma and auxiliary gas. The 0.5% mixture was chosen because this is approximately the ratio of hydrogen to argon supplied to the plasma by conventional nebulization. This concentration of hydrogen was also necessary to provide sufficient intensity of the H_β line for half width measurements.

Even this very low concentration of hydrogen resulted in a substantially different plasma from a pure argon plasma. The plasma was extremely difficult to ignite and under normal ICP operating conditions produced a visibly smaller plasma.

To evaluate electron density radially resolved electron density profiles were measured for 4, 8, 12, 16 and 20 mm above the load coil at an input power of 1.25 kW. The radial electron densities at the 5 heights were integrated to produce an isocontour plot of electron density. Figure 15 is the electron density contour plot for an rf input power of 1.25 kW and a plasma gas containing 0.5% hydrogen weight by volume.

There is a substantial difference between this figure and Figure 11 representing electron density in a pure argon plasma under the same operating conditions. Electron density was much higher when hydrogen was present in the plasma gas, virtually all spatial regions in the plasma had electron densities greater than $3.0 \times 10^{15} cm^{-3}$. The region of low electron density observed in the central aerosol channel under most plasma conditions was almost totally absent. A somewhat more subtle difference was observed in the n_e distribution at the plasma edges. The mixed gas ICP had slightly lower values of n_e at the edge than the corresponding region in a pure argon plasma. This appeared to be

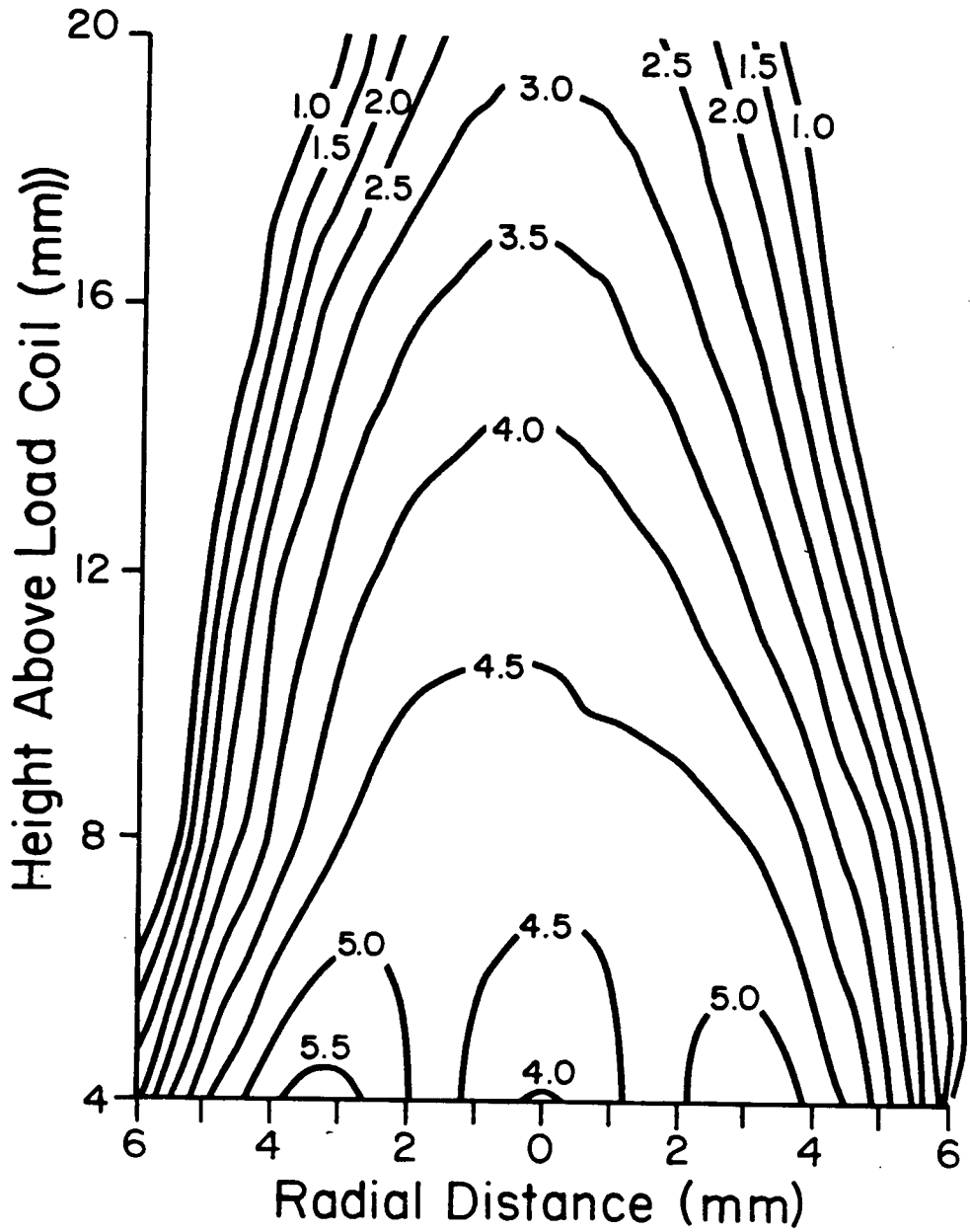

Figure 15 Electron density isocontour plot at an rf input power of 1.25 kW for 0.5% hydrogen w/v in argon plasma gas. Density values of the isocontour lines in units of $10^{15} cm^{-3}$.

a manifestation of the thermal pinch effect reducing the plasma size. Batal et al. [57] also observe lower electron density at the plasma edge for an argon hydrogen plasma.

In a study of electron densities of mixed gas plasmas containing oxygen and argon or nitrogen and argon, Choot and Horlick [87] observe similar results. The electron density increases in the bulk of the plasma and there is a narrowing of the plasma for gas mixtures. Montaser and Fassel [84] also measure increased electron density in an argon-nitrogen ICP. The presence of a molecular species in the plasma gas appears to be an important factor.

The difference in electron density between the argon ICP and the argon-0.5% hydrogen ICP was of the order of $2 \times 10^{15} cm^{-3}$. It is unlikely ionization of hydrogen is the sole source of this increased electron density. The concentration of hydrogen is such that it would have to be almost 100% ionized to cause this difference. It is unreasonable to have hydrogen with an ionization potential of 13.58 eV 100% ionized while argon with an ionization potential of 15.755 eV is less than 1% ionized. The thermal pinch effect is a much more likely cause and a change in coupling of energy from the load coil due to the presence of a molecular species instead of atomic argon alone.

The dramatic changes in n_e when even this small amount of hydrogen was admixed in the plasma indicates that caution is advised in the interpretation of studies where hydrogen has been added to the plasma gas.

3.6 SUMMARY

Complete radially resolved spatial maps of the electron density distribution in the ICP under a variety of conditions have been prepared. The spatial structure of electron density was complex. Overall electron concentration increased with increasing power and decreased with higher aerosol flow rates. The presence of easily ionizable elements had no apparent effect on the measured electron density. Small amounts of hydrogen in the plasma gas significantly affected the electron density.

Chapter 4

ION-ATOM EMISSION INTENSITY RATIOS AND LOCAL THERMAL EQUILIBRIUM

4.1 INTRODUCTION

Two recent publications [17,73] identify the understanding of high analyte ionic line sensitivities as one of the main fundamental problems in inductively coupled plasma spectrometry. The ratio of emission intensity of an ion line (I_i) and an atom line (I_a) of the same element is significantly higher than expected from LTE expressions using excitation temperatures.

A number of researchers has investigated ion-atom emission intensity ratios (I_i/I_a) [28,62,86] and the closely related parameters of ionization temperature [53] and electron density derived from the Saha equation [67]. One of the more significant and perhaps most widely quoted papers is a landmark study by Boumans and deBoer [28]. The observed intensity ratio for ion-atom line pairs differ from values derived from Saha's equation using a spectroscopic excitation temperature of 5850 K and an electron concentration of 10^{16} cm^{-3}. Experimental ratios exceed calculated ratios by one to three orders of magnitude. The result requires an overpopulation of the ion line excited state as compared to the value at 5850 K. To account for this overpopulation, Boumans and deBoer proposed a suprathermal population of metastable argon levels and that metastable argon atoms increase the ion level population through collisional excitation or Penning ionization.

It should be pointed out that the LTE values reported by Boumans and deBoer [28] are not consistent with the postulates of LTE. The linking of electron density to a unique LTE temperature

for a given pressure and plasma composition imposes restrictions on the use of LTE expressions. The temperature of 5850 K and the electron density of 10^{16} cm^{-3} are clearly not a consistent set of parameters for argon at 1 atm. Using these values simultaneously in an equilibrium expression (the Saha equation) to calculate ion-atom ratios will lead to a number, but this is not an LTE value as reported by Boumans and deBoer.

The data presented in this thesis shed new light on the ion-atom emission intensity problem and represent a departure from previous thinking in this area. The essential element of the approach was the temperature used in the calculation of LTE values. The inconsistency between temperature and electron density was removed by using the experimentally measured n_e to evaluate a temperature, $T_{e,LTE}$, for use in calculations of LTE values. For reasons discussed in Section 4.2 it was decided $T_{e,LTE}$ provided a more appropriate temperature to use to describe an LTE system.

In this work, experimental ion-atom intensity ratios are compared to calculated LTE ion-atom intensity ratios by a non-equilibrium parameter b_r, where

$$(I_i/I_a)_{exp} = b_r \quad (I_i/I_a)_{LTE} \tag{4.1}$$

The relationship between b_r as defined in Equation 4.1 and b(p), the equilibrium departure factor, as defined in Equation 1.6 can be derived. First, it is recognized that the LTE population of a level and Saha population in Eq. 1.6 are equivalent by definition. Then, with substitution of equations 1.1 and 1.6, and rearrangement Eqn. 4.1 can be written as

$$b_r = 1/b(p)\ (n^+_p/n^+_{p,s}) \qquad (4.2)$$

Here n^+_p and $n^+_{p,s}$ are the experimental and LTE populations of the excited ion level respectively. The Boltzmann distribution (Eqn 1.2) can be substituted for n^+_p and $n^+_{p,s}$ where the different excitation temperatures describe the differences in population between the experimental and LTE situations.

$$b_r = 1/b(p)\ \exp(\ E_p^+/kT_{LTE} - E_p^+/kT_{i,exc}) \qquad (4.3)$$

E_p^+ is the excitation energy of the ion level and $T_{i,exc}$ the Boltzmann temperature for this level relative to the ion ground state. The non-equilibrium parameter b_r is approximately the inverse of b(p). The smaller the difference between the LTE temperature and the excitation temperature of the ion level the better the approximation. Thus, the evaluation of b_r can provide an indication of the value of b(p).

The results presented in this chapter have been previously published [75,76].

4.2 CALCULATION OF TEMPERATURE FROM ELECTRON DENSITY

As has been pointed out by Raaijmakers et al. [73] one approach to modelling the ICP is to accurately measure n_e and estimate T_e from the electron density. If the plasma is not too far from LTE, estimating the electron temperature as $T_{e,LTE}$ yields a result close to the actual electron temperature. Whether the temperature derived in this manner is actually the electron temperature or not, it will be used as the temperature

in LTE calculation for reasons discussed below.

It is possible to calculate a temperature from the measured electron density if the pressure is known, since the two quantities are coupled through a series of equations. To a first approximation the ICP can be considered to be an one element plasma, consisting only of argon gas, with only neutral (n_{Ar}) and singly ionized ($n_{Ar}+$) argon species and electrons (n_e) present. The relations then are

(1) the condition of local electrical neutrality

$$n_e = n_{Ar}+ \tag{4.4}$$

(2) Dalton's law

$$P = (n_{Ar} + n_{Ar}+ + n_e)kT \tag{4.5}$$

(3) and the Saha equation

$$n_{Ar}+n_e/n_{Ar} = 2Q_{Ar}+(T)/Q_{Ar}(T)\ (2\pi kT/h^2)^{3/2}\exp(-E_i'/kT) \tag{4.6}$$

where P is the pressure of the plasma, 1 atm in the case of the ICP. E_i' is the effective ionization potential of argon given by $E_i' = E_i - \Delta E_i$, where E_i is the unperturbed ionization energy of argon (15.755 eV) and ΔE_i is the lowering of the ionization potential ($\sim$ 0.08 eV) caused by the interaction of the atom with the surrounding charged particles [111]. $Q_{Ar}(T)$ and $Q_{Ar}+(T)$ the internal partition functions of argon atom and ion species respectively. Partition functions were taken from de Galan et al. [112]. The temperature obtained by substituting the measured electron density in these equations was labelled $T_{e,LTE}$. The

$T_{e,LTE}$ values evaluated for the corresponding n_e values are provided in Table III. Each LTE parameter is related to n_e alone because with a knowledge of pressure and n_e, temperature is defined for LTE.

The temperature calculated is an argon ionization temperature. Argon is the primary source of electrons in the plasma and it is not unreasonable to expect its ionization to control the electron temperature. If other species in the plasma, such as solvent and analyte, contribute significantly to the electron density their effect must be included in the temperature calculation. The concentration of analyte species in the plasma is so low that even if 100% ionized its contribution to total electron density is insignificant [106]. The effect of solvent, in this case water, and its dissociation products on electron density are the subject of Chapter 6. The overall contribution to electron density was minimal.

If the pressure is known, then only one of the experimental parameters of temperature or electron density can be input into the LTE equations, the other is fixed. Utilizing electron density as the defining parameter is preferred for a number of reasons. At any spatial position in the plasma for a given set of conditions the electron density is single valued whereas the temperature can assume a variety of values depending on the method, species and energy levels used to measure it [53]. For a great many types of plasmas, electrons are the species primarily responsible for excitation [38]. Because of their low mass, electrons acquire a thermal distribution very rapidly. In fact the Maxwellian electron distribution may be the single

Table III

Calculated LTE Temperature Corresponding to Measured Electron Densities

Electron Density (cm^{-3})	LTE Temperature (K)
1×10^{14}	6498
2×10^{14}	6827
3×10^{14}	7036
4×10^{14}	7192
5×10^{14}	7317
6×10^{14}	7423
7×10^{14}	7515
8×10^{14}	7596
9×10^{14}	7669
1×10^{15}	7736
2×10^{15}	8205
3×10^{15}	8506
4×10^{15}	8733
5×10^{15}	8919
6×10^{15}	9076
7×10^{15}	9212
8×10^{15}	9334
9×10^{15}	9443
1×10^{16}	9544

equilibrium expresison that has complete validity in an ICP. Although there is no experimental evidence to support this statement, Thomson scattering experiments under way in other labs may soon yield some answers [65,113].

The temperature calculated from electron density was higher than other temperatures typically measured in the ICP. Table IV lists the radially resolved electron density measured at 16 mm above the load coil for five different input powers, the calculated $T_{e,LTE}$ corresponding to the measured n_e and for comparison Fe I excitation temperatures for these conditions. The Fe I temperatures were lower than the analogous LTE temperature, but with increasing rf power the difference between the two temperatures decreased. At the higher powers, the electron density was greater and one would expect to move closer to an LTE plasma in which all the temperatures are equivalent. This relationship between the various temperatures and electron density has been observed in many physical plasmas [114-116].

The question remains as to how accurate is $T_{e,LTE}$ as an estimate of the actual T_e. There are few measurements of electron temperature in the ICP due to the difficulties in determining T_e spectroscopically in a source not in LTE [114]. Hasegawa and Haraguchi [35] obtained T_e from a measurement of the absolute continuum intensity without assuming thermal equilibrium. At an observation height of 15 mm and in the plasma center a T_e of 8400 K is measured for an n_e of 1.4×10^{15} cm^{-3}, a difference of only 300 K from $T_{e,LTE}$. In general, T_e and $T_{e,LTE}$ differ by only ± 500 K, indicating $T_{e,LTE}$ is a good estimate of the electron temperature.

Table IV

Electron density (n_e) [96], argon ionization temperature ($T_{e,LTE}$) and FeI excitation temperature [58] for rf input powers of 1.00, 1.25, 1.50, 1.75 and 2.00 kW.

Rf power	$n_e(cm^{-3})$	$T_{LTE}(K)$	$T_{exc}(K)$
1.00	7.1×10^{14}	7520	5200
1.25	1.8×10^{15}	8150	5850
1.50	2.7×10^{15}	8430	6440
1.75	3.4×10^{15}	8600	7010
2.00	4.0×10^{15}	8730	7420

4.3 CALCULATION OF LTE ION-ATOM EMISSION INTENSITY RATIO

The LTE value of the relative intensity of an ion line to an atom line has been calculated from a form of the Saha equation given by Boumans and de Boer [28]

$$(I_i/I_a)_{LTE} = 4.83 \times 10^{15}/n_e \, (g_q A_{qp}/\lambda_{qp})_i \, (\lambda_{qp}/g_q A_{qp})_a \times T^{3/2} \exp[(-E_i - E_{qi} + E_{qa})/kT] \quad (4.7)$$

where g_q and E_q(eV) are the statistical weight and excitation energy of the upper level of the transition $q \rightarrow p$, $A_{qp}(s^{-1})$ and λ_{qp}(nm) are the corresponding transition probability and wavelength, E_i (eV) the ionization energy of the species, T(K) the absolute temperature, n_e (cm^{-3}) the electron number density, and the subscripts i and a refer to ion and atom species respectively.

The spectral data necessary for this calculation for the elements studied is listed in Table V. All transition probabilities are from the tabulation of Wiese and Martin [117].

4.4 EXPERIMENTAL

In order to investigate the spatial dependence of departures from LTE and the relationship to rf input power, b_r has been determined from magnesium ion-atom ratios at a number of spatial positions for two input powers. The lateral intensities of the magnesium 285.2 nm atom line and the magnesium 280.3 nm ion line were measured at 150 spatial positions across the plasma for vertical heights of 4, 8, 12, 16 and 20 mm above the load coil at

Table V

Spectral Data of Ionic and Atomic Lines

Wavelength (λ) of emission lines, excitation energy of upper level (E_q), ionization energy of the atom (E_i), and transition probabilities (gA) for Sr, Ca, Mg, Cd and Zn.

Element		λ(nm)	E_q(eV)	E_i(eV)	$g_q A_{qp}(10^8 s^{-1})$
Sr	I	460.7	2.692	5.692	6.03
	II	407.8	3.042		5.68
Ca	I	422.7	2.936	6.111	6.54
	II	393.6	3.152		5.88
Mg	I	285.2	4.35	7.644	14.4
	II	279.5	4.43		10.4
	II	280.3	4.42		5.32
Cd	I	228.8	5.42	8.991	15.9
	II	226.5	5.47		6.0
Zn	I	213.9	5.80	9.391	21.27
	II	202.5	6.13		13.2

rf input powers of 1.25 and 1.75 kW. The lateral intensity profiles were converted to radial profiles using an Abel inversion and the ratios at each radial position were calculated.

Spatial studies of b_r were also performed utilizing the element cadmium. The lateral intensities of the cadmium 228.8 nm atom line and the cadmium 226.5 nm ion line were measured at 150 spatial positions across the plasma for vertical heights of 8, 12 and 20 mm above the load coil at rf input powers of 1.25 and 1.75 kW. The resulting lateral profiles were Abel inverted and the ratios at each radial position were calculated.

To investigate the dependence of b_r values on ionization energy, b_r was determined for a set of elements with ionization energies ranging from 5.7 to 9.4 eV. The elements chosen for this study were; Sr, Ca, Mg, Cd and Zn. Table V lists the spectral data for the relevant ion and atom lines for these elements. All gA values were taken from Wiese and Martin [117].

In order to generate the b_r value, the lateral emission intensities of the ion and atom lines for each of the elements listed in Table V were measured at 150 spatial positions across the plasma at a vertical height of 16 mm above the load coil. The resultant lateral intensity profiles were converted to radial profiles using an Abel inversion. This was done at rf input powers of 1.00, 1.25, 1.50, 1.75 and 2.00 kW. Experimental ion-atom emission intensity ratios were evaluated and compared to LTE ion-atom emission intensity calculated in the manner described in Section 4.3.

The gas flows used for all measurements were 11 l m^{-1} plasma, 0.3 l m^{-1} auxiliary and 0.9 l m^{-1} aerosol flow.

All solutions were made up in deionized water. A 50-ppm Sr solution (from $SrCl_2.6H_2O$) was used for Sr measurements, a 50-ppm Ca solution (from $CaCO_3$) for Ca measurements, a 250-ppm Mg solution (from $MgCl_2.H_2O$) for Mg measurements, a 1500-ppm Cd solution (from $CdCl_2.2H_2O$) for Cd measurements and a 1500-ppm Zn solution (from $ZnCl_2$) for Zn measurements. All lines used were checked for self absorption by performing calibration curves and only concentrations in the linear range of the curve were used.

4.5 RESULTS FOR MAGNESIUM

4.5.1 LTE ION-ATOM EMISSION INTENSITY RATIOS

LTE intensity ratios for the Mg II (280.3 nm) and Mg I (285.2 nm) pair have been evaluated using the measured n_e and calculated $T_{e,LTE}$. The values calculated in this manner are provided in Figure 16. The solid lines in Figures 16(i), 16(ii), 16(iii), 16(iv) and 16(v) represent $(I_i/I_a)_{LTE}$ for the magnesium line pair for vertical heights above the load coil of 4, 8, 12, 16 and 20 mm respectively. The curves corresponding to each power setting are identified in the figures.

The $(I_i/I_a)_{LTE}$ ratios in Figure 16 have a spatial and power dependence similar to that of electron density. This was expected since the ratios have been calculated from the measured electron densities. The $(I_i/I_a)_{LTE}$ presented are much higher than any which have been previously reported in the literature [28]. This can be attributed to the higher temperature, $T_{e,LTE}$ ranging from 7000 to 9000 K, used in the Saha equation. As discussed previously, this is really the only appropriate

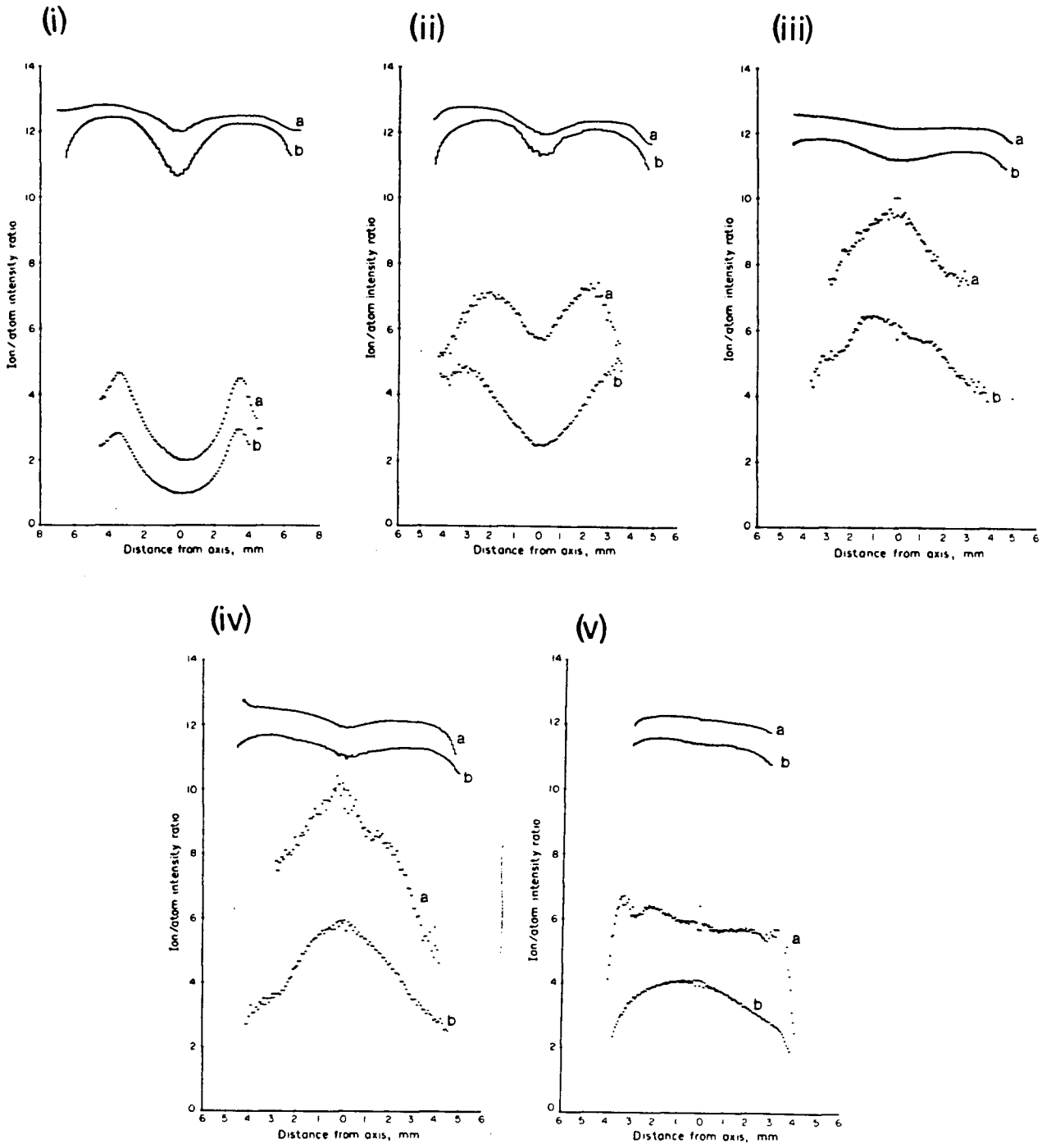

Figure 16 Spatially resolved ion-atom emission intensity ratios for magnesium for input powers of (a) 1.75 kW and (b) 1.25 kW, at vertical heights of (i) 4 mm, (ii) 8 mm, (iii) 12 mm, (iv) 16 mm and (v) 20 mm above the load coil. Solid lines represent calculated LTE values, dashed lines experimental measurements.

temperature to use for an LTE calculation.

4.5.2 EXPERIMENTAL ION-ATOM EMISSION INTENSITY RATIOS

Experimental ion-atom intensity ratios, at the same spatial positions and powers n_e was measured at, were collected for comparison with the calculated LTE ratios. The intensity ratio of the magnesium 280.3 nm ion line to the magnesium 285.2 nm atom line measured for the two input powers at five different heights above the load coil are presented in Figure 16, represented by the broken lines. Figures 16(i), 16(ii), 16(iii), 16(iv) and 16(v) are for the vertical heights 4, 8, 12, 16 and 20 mm above the load coil respectively. The curves corresponding to the different input powers are identified in the figure.

The experimental emission intensity ratios of ion line to atom line $(I_i/I_a)_{exp}$ increased with increasing power. There was a strong spatial dependence in the ratios. At 4 mm above the load coil the ratio is greatest at ± 3 mm out from the plasma center, where n_e is large, and decreased in the aerosol channel. A similar pattern is observed at 8 mm. For 12 and 16 mm $(I_i/I_a)_{exp}$ was greatest at the plasma center and decreases towards the edges. The value of the experimental intensity ratio is almost constant over the width of the plasma at 20 mm. The values of $(I_i/I_a)_{exp}$ for this Mg line pair compare favorably with previously reported results [67].

The maximum $(I_i/I_a)_{exp}$ was along the plasma central axis between 12 to 16 mm above the load coil for both power settings. This vertical height was where n_e maximizes in the central channel. As the power increased, n_e increased and the $(I_i/I_a)_{exp}$

increased. However, regions of highest n_e did not exhibit the highest $(I_i/I_a)_{exp}$ ratios. Also for a particular value of the electron density the ion-atom emission intensity ratio did not necessarily have a single value, i.e. at different spatial positions in the plasma where $n_e = 3 \times 10^{15}$ cm^{-3}, $(I_i/I_a)_{exp}$ does not have the same value. The relationship between n_e and the $(I_i/I_a)_{exp}$ ratio changes with position in the plasma and with different power setting. This implies that n_e is not the only factor determining the ion-atom emission intensity ratio.

4.5.3 DEVIATIONS FROM LTE - B_r

Examination of Figure 16 reveals that the experimental ion-atom emission intensity ratios were less than the calculated LTE ion-atom ratios. Using n_e as a basis for an LTE framework leads to a model in which experimental ion-atom ratios were within a factor of 10 of LTE values rather than orders of magnitude greater than LTE values as previously reported [28,62]. In order to examine the deviation of the plasma from LTE, plots were made of b_r - the ratio of $(I_i/I_a)_{exp}/(I_i/I_a)_{LTE}$ as discussed in Section 4.1. Figures 17(i), 17(ii), 17(iii), 17(iv) and 17(v) represent b_r for Mg II/ Mg I at vertical heights of 4, 8, 12, 16 and 20 mm above the load coil respectively. The curves corresponding to the two power settings are identified in the figure.

At LTE, b_r would be equal to one. The value of b_r was less than one in all cases; i.e. experimental ion-atom emission intensity ratios were less then LTE ion-atom emission intensity ratios at all spatial positions and powers. This finding is the

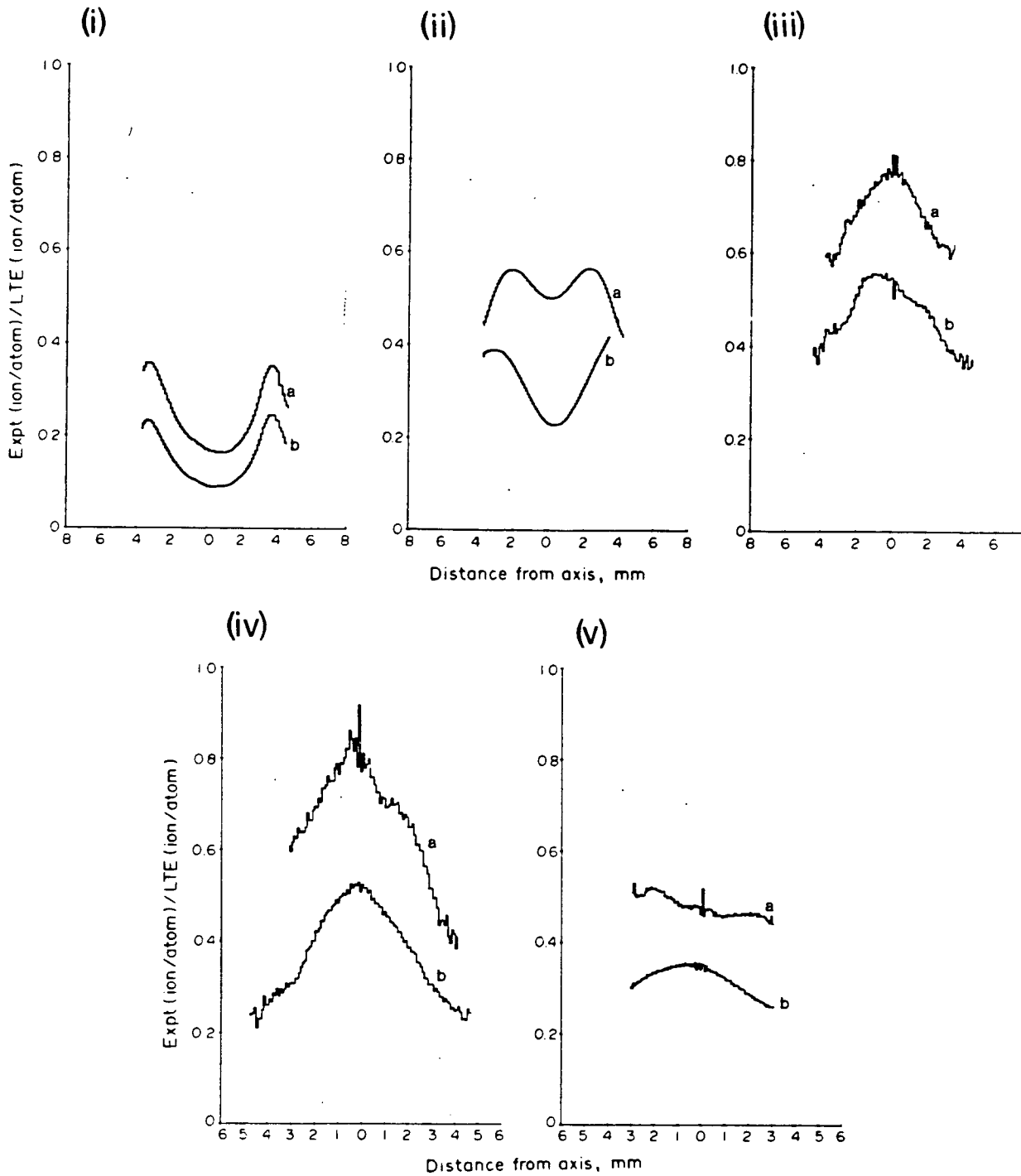

Figure 17 Spatially resolved ratio of experimental ion-atom intensity ratio to LTE ion-atom intensity ratio (b_r) for magnesium at input powers of: (a) 1.75 kW and (b) 1.25 kW, at vertical heights of (i) 4 mm, (ii) 8 mm, (iii) 12 mm, (iv) 16 mm and (v) 20 mm above the load coil.

inverse of previous reports regarding experimental and LTE ion-atom ratios [28] and can be attributed to the temperature chosen to describe LTE conditions. For the reasons discussed in Section 4.2 and in reference 73, it was felt that the temperature based on n_e used in this paper was more appropriate for the definition of LTE than the combination of a spectroscopically measured excitation temperature and n_e.

To aid in the visualization of b_r as a function of spatial position in the plasma, contour plots have been drawn for each power setting for magnesium. These plots are presented in Figures 18(i) and 18(ii), which are for input powers of 1.25 and 1.75 kW respectively. The value for b_r was lowest in the center of the plasma at low vertical heights, in the region corresponding to the aerosol channel. It increased slightly in the annular regions of the plasma just above the load coil. The maximum value of b_r appeared along the central plasma axis at a vertical height of between 12 to 16 mm. Therefore the analytical zone appears to be the region closest to LTE. Furuta [61], using the same approach to evaluate deviations from LTE with calcium as the test element, also finds the analytical zone the spatial region of the plasma closest to LTE.

The greater the electron concentration, the more likely the excitation processes in the plasma are collisionally dominated, and the plasma should be closer to LTE. Comparing the b_r values at the two power settings, this trend was followed. The highest n_e was at 1.75 kW and the b_r values were closest to one for this power setting. However, for a single power setting, spatial positions with the highest electron density did not necessarily

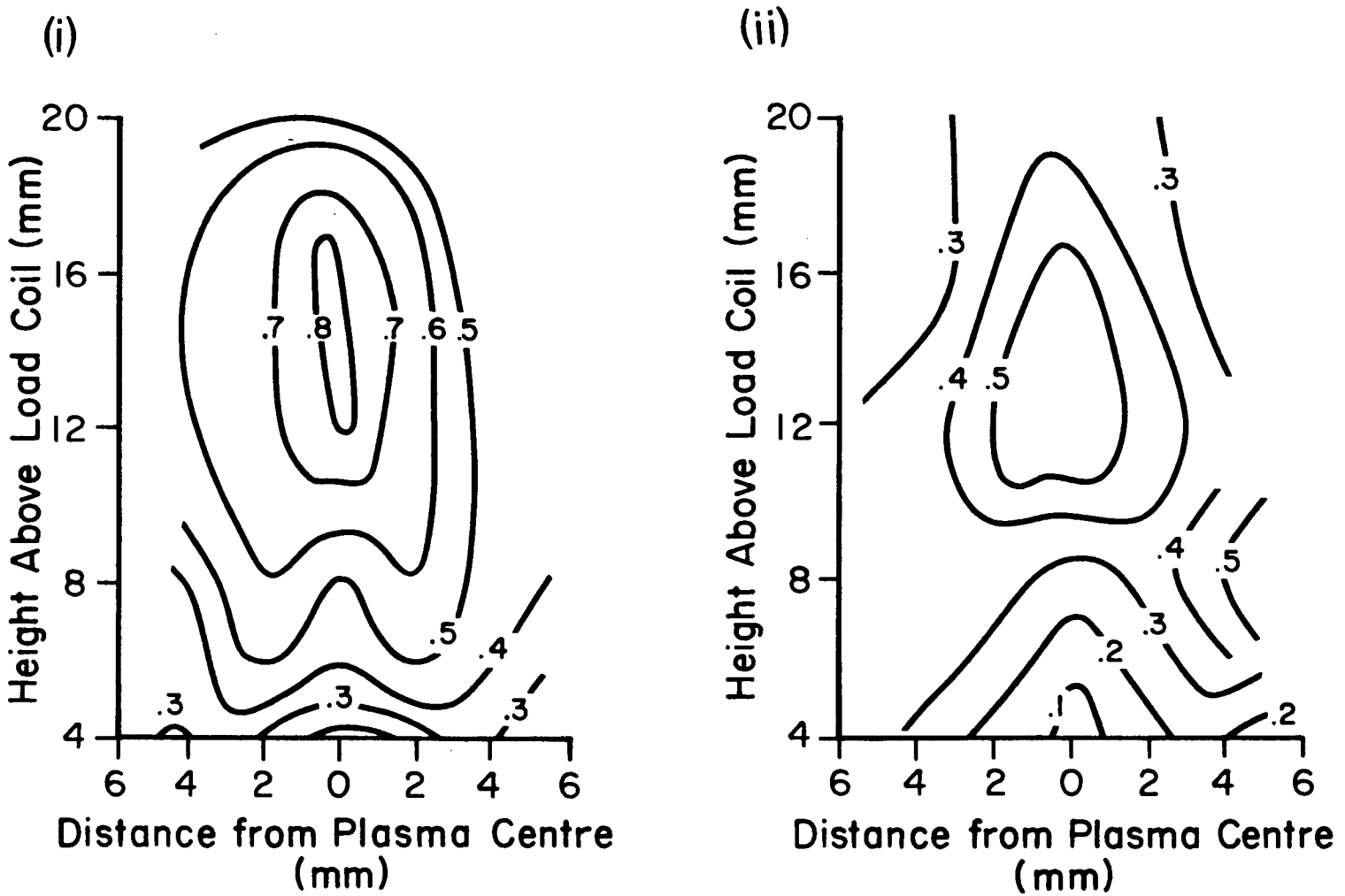

Figure 18 Isocontour plot of b_r for magnesium in the ICP at input powers of (i) 1.75 kW and (ii) 1.25 kW.

have the largest b_r value.

Since the evaluation of b_r involves a number of successive steps, propagation of error becomes important. The error associated with the evaluation of n_e is about ± 10%; the major contributions coming from the Abel inversion and the measurement of the halfwidth of the H_β profile. The uncertainty in n_e introduces an error of about ± 2% in the calculation of $T_{e,LTE}$. The error in the experimental evaluation of the ion-atom emission intensity ratio is estimated to be less than ± 10%, chiefly as a result of the Abel inversion procedure. The net propagated error in b_r is thus approximately ± 15%. This could be compounded by uncertainties in the gA values, which, for Mg, are in the range of ± 30%. However, since the calculation of $(I_i/I_a)_{LTE}$ involves the ratio of gA values, the impact of this uncertainty is reduced. Overall, even when errors were included, the same general trend was observed; b_r values were less than one for all observations.

4.6 RESULTS FOR CADMIUM

4.6.1 LTE ION-ATOM EMISSION INTENSITY RATIOS

LTE intensity ratios for the Cd II (226.5 nm) and Cd I (228.8 nm) pair have been evaluated. The calculated values are plotted in Figure 19. The solid lines in Figures 19(i), 19(ii) and 19(iii) represent $(I_i/I_a)_{LTE}$ for the cadmium line pair for vertical heights of 8, 16 and 20 mm above the load coil. The curves corresponding to each power setting have been identified in the figures.

The magnitude of these LTE values differ from those derived

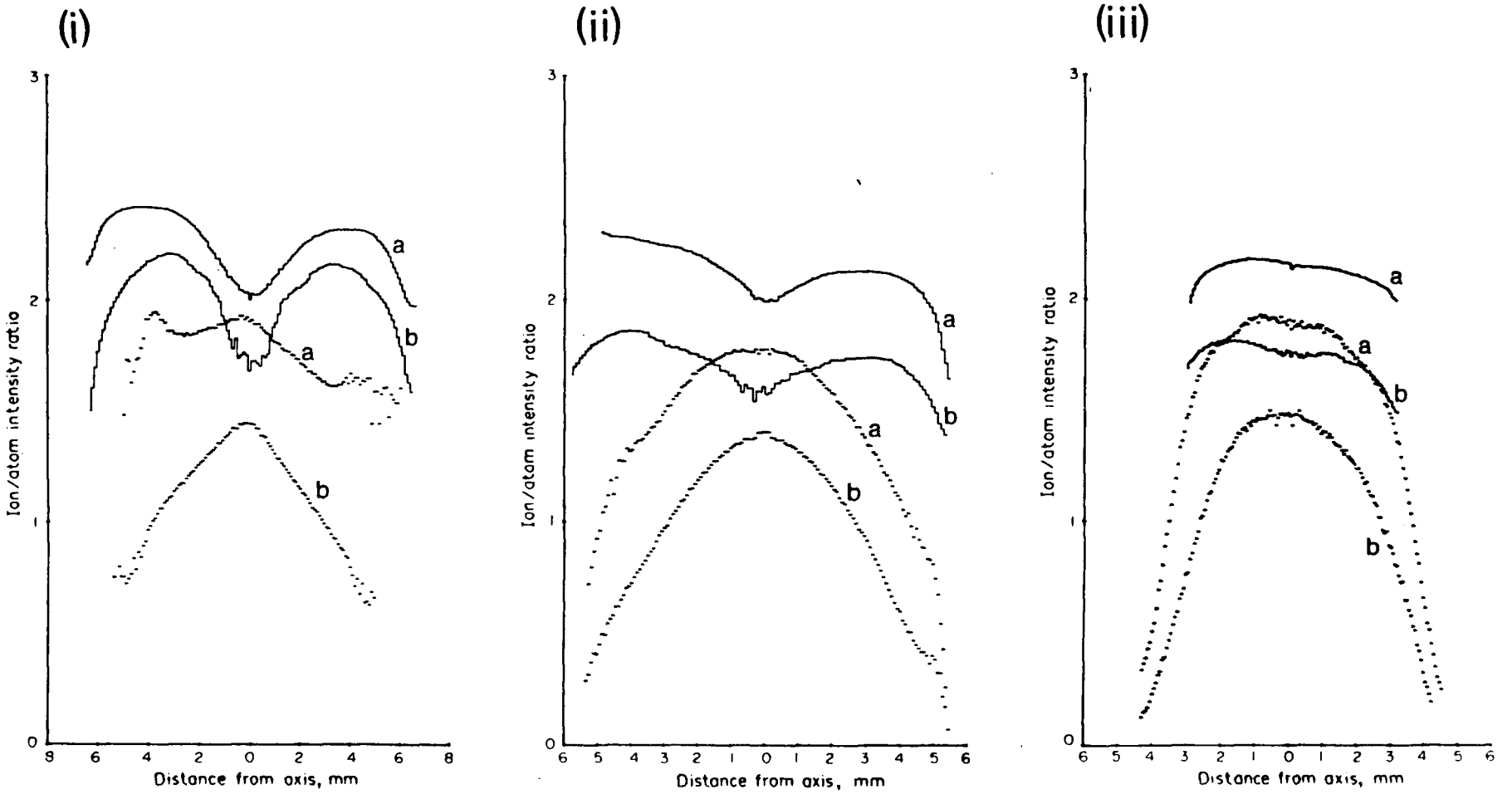

Figure 19 Spatially resolved ion-atom emission intensity ratios for cadmium for input powers of (a) 1.75 kW and (b) 1.25 kW, at vertical heights of (i) 8 mm, (ii) 12 mm and (iii) 20 mm above the load coil. Solid lines represent calculated LTE values, dashed lines experimental measurements.

for magnesium but the spatial and power dependence was the same. As both sets of values were calculated from the same electron densities and temperatures this was expected.

4.6.2 EXPERIMENTAL ION-ATOM EMISSION INTENSITY RATIOS

Experimental intensity ratios for the Cd II (226.5 nm) ion line and Cd I (228.8 nm) atom line at three heights and two input powers were made and are plotted in Figure 19. Figures 19(i), 19(ii) and 19(iii) are for the heights 8, 16 and 20 mm respectively. The curves corresponding to the different input powers are identified in the figure.

The experimental ion-atom emission intensity profiles for Cd II/ Cd I have a spatial and power dependence similar to the experimental results for magnesium. The values of $(I_i/I_a)_{exp}$ obtained compare favorably with those of other authors [28,67].

4.6.3 DEVIATIONS FROM LTE - b_r

In Figure 20, b_r is plotted for cadmium. Figures 20(i), 20(ii) and 20(iii) are for the vertical heights 8, 16 and 20 mm respectively. As with magnesium, the experimental ion-atom emission intensity ratios were less than the calculated LTE ion-atom ratios at all spatial positions and powers.

The b_r values for cadmium were generally much closer to one (LTE) than for those magnesium. Neglecting the errors in gA values, the higher ionization energy of cadmium could contribute to this. At an n_e of 3×10^{15} cm^{-3} and $T_{e,LTE}$ of 8500 K magnesium is 98% ionized and cadmium is 92% ionized. Even a small overpopulation of the magnesium atom level could produce a

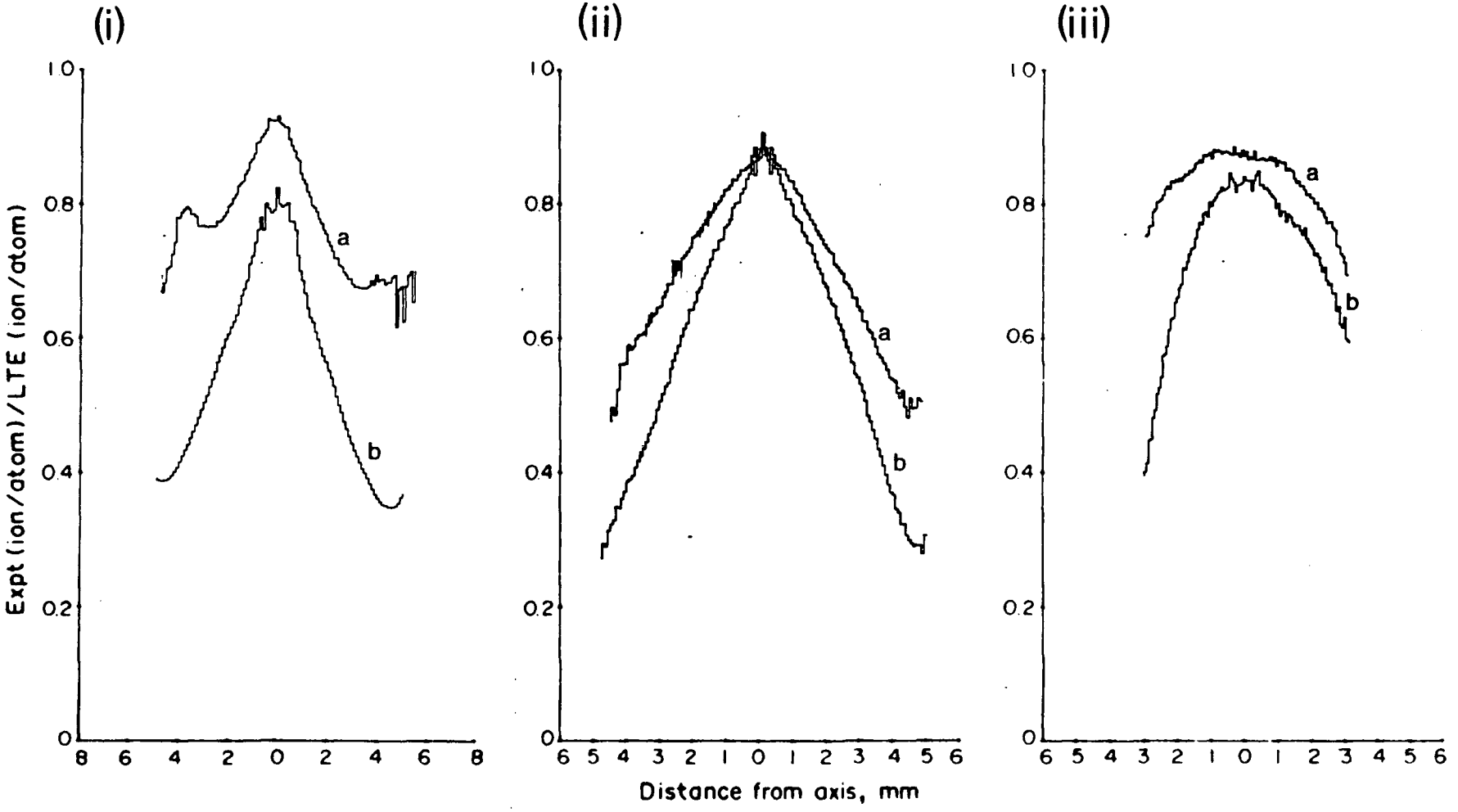

Figure 20 Spatially resolved ratio of experimental ion-atom intensity ratio to LTE ion-atom intensity ratio (b_r) for cadmium input powers of : (a) 1.75 kW and (b) 1.25 kW, at vertical heights of (i) 8 mm, (ii) 12 mm and (iii) 20 mm above the load coil.

significant lowering of the experimental ion-atom emission intensity ratio relative to the LTE ratio. If the cadmium atom level was overpopulated to the same extent, the difference between the experimental ion-atom ratio and the LTE ratio would not be as great as for Mg due to the lower degree of ionization. This is one possible interpretation for the difference in relative magnitudes of b_r, for Mg and Cd.

4.7 LTE DEVIATIONS FOR A NUMBER OF ELEMENTS

The b_r values for Mg and Cd have been found to be less than 1 under all conditions studied. The question arises whether this is a universal characteristic for all analyte species, and if so, what the underlying cause is. There are three possibilities; a non-Boltzmann population distribution of excited states and/or ionization non-equilibrium in which the relative population of atom and ion species depart from Saha equilibrium. The differing b_r values for Mg and Cd, with Cd being closer to LTE, do not indicate which process is more significant in the ICP and what critical analyte characteristic defines b_r behavior.

To investigate further the cause of non-equilibrium, b_r was evaluated at a number of rf input powers for a group of elements with ionization energies ranging from 5.7 to 9.4 eV. The elements were Sr, Ca, Mg, Cd and Zn and relevant spectral data are listed in Table V. For this series of experiments the Mg 279.5 nm ion line and Mg 285.2 nm atom line pair were used. The behavior of b_r with power at 16 mm above the load coil in the center of the plasma, the region of the ICP closest to LTE, was investigated. Table IV lists the measured electron density for

this spatial position and the corresponding temperature, $T_{e,LTE}$, derived from this measurement for the five input powers.

The experimental and LTE ion-atom emission intensity ratios, obtained for the five elements along the discharge axis, at 16 mm above the load coil, are listed in Table VI for rf input powers of 1.0, 1.25, 1.50, 1.75 and 2.0 kW. The ratios of experimental and LTE values (b_r) is plotted as a function of rf power in Figure 21. There are several interesting features apparent in this plot. All of the experimental ion-atom emission intensity ratios were within a factor of 5 of the LTE value, in other words, the measured ion-atom emission intensity ratios were near LTE. This result was consistent with the results for Cd and Mg. The values of experimental ion-atom emission intensity ratios, for the five elements, obtained compare favorably with those of other authors [28,62,67,86]. The measured electron densities are also typical for the ICP [61,87,88]. The difference between the above results and previous work on ion-atom intensity ratios [28,62] arises solely from the temperature used to evaluate LTE values.

All elements exhibited an increase in b_r as the rf power was increased, although it appeared that the response behavior of the five elements can be divided into two classes; those with a relatively low slope (Cd, Mg and Zn) and those with a higher slope (Sr and Ca). Also, following the same division, the b_r value for Cd, Mg and Zn was less than one for all rf input powers, whereas the b_r value for Ca and Sr exceeds one at higher rf input powers. Interestingly, this classification of b_r response correlates with reported vertical spatial behavior of

Table VI

Experimental and LTE ion-atom emission intensity ratios for Sr, Ca, Mg, Cd and Zn at rf powers of 1.00, 1.25, 1.50, 1.75 and 2.00 kW.

Rf power (kW)		1.00	1.25	1.50	1.75	2.00
Sr	$(I_i/I_a)_{exp}$	82.7	147.1	372	463	518
	$(I_i/I_a)_{LTE}$	423	375	358	348	342
Ca	$(I_i/I_a)_{exp}$	43.4	95.6	163	212	260
	$(I_i/I_a)_{LTE}$	249	228	221	217	213
Mg	$(I_i/I_a)_{exp}$	4.93	6.62	10.3	12.3	13.6
	$(I_i/I_a)_{LTE}$	21.8	23.6	24.4	24.9	25.2
Cd	$(I_i/I_a)_{exp}$	---	1.08	1.34	1.63	1.89
	$(I_i/I_a)_{LTE}$	1.47	1.85	2.03	2.15	2.24
Zn	$(I_i/I_a)_{exp}$	---	0.37	0.55	0.72	0.82
	$(I_i/I_a)_{LTE}$	0.90	1.23	1.40	1.51	1.59

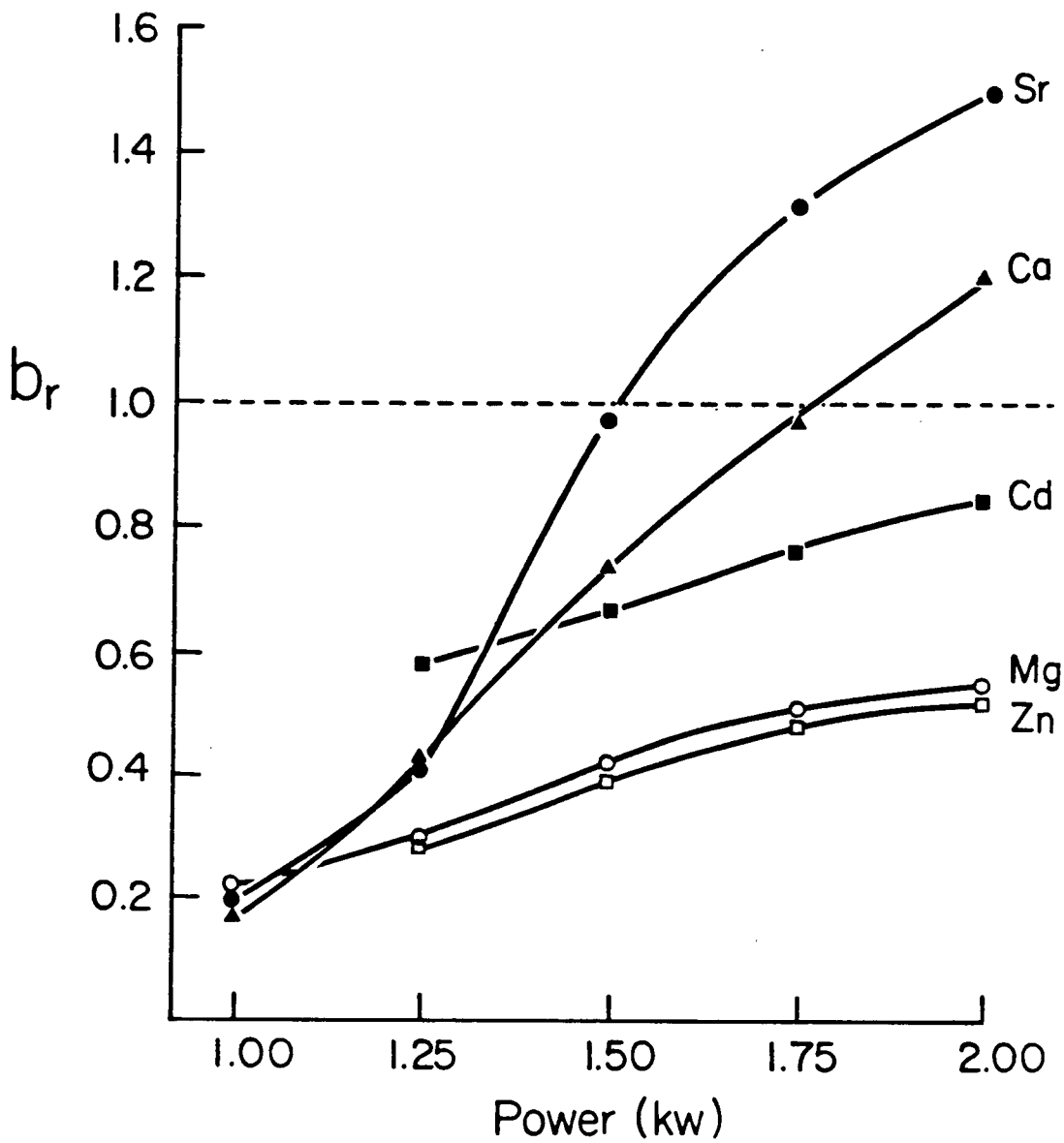

Figure 21 Deviation of experimental ion-atom emission intensity ratio from LTE ion-atom emission intensity ratio (b_r) as a function of input power.

analyte emission. Several years ago Blades and Horlick [118] noted that there appear to be two classes of analyte behavior that could be recognized by emission line response to changes in rf input power [118]. Analyte emission lines are termed hard or soft (after Boumans [119]) depending on whether the line showed a shift in the spatial position of maximum emission intensity with a change in rf power (soft) or remained relatively unchanged (hard). According to this criterion the atom lines of Sr and Ca are soft and those of Cd, Mg and Zn are hard. It is apparent that this class behavior is also reflected in the b_r plot of Figure 21. The higher slope for Sr and Ca could be interpreted in terms of a shift in the atom line spatial profile down towards the load coil as the rf power is increased. In contrast, the position of the maximum on the ion line profile for Sr and Ca would remain unchanged, as would the position for both atom and ion lines for Cd, Mg and Zn. This would act to enhance the change in ion-atom ratio for Sr and Ca as the rf power is increased. While this intuitive picture can help to rationalize the b_r data it does not help us to understand the underlying cause for the behavior depicted in Fig. 21.

4.8 DISCUSSION

The implications of the data presented here, that is, experimental ion-atom intensity ratios that are less than LTE ratios, are many. It appears that the discharge does not exhibit suprathermal ion-atom ratios; rather, ion-atom emission intensity ratios are infrathermal. It also seems that ion levels are not necessarily overpopulated with respect to LTE conditions; in

fact, the data suggests that it is the neutral levels that are overpopulated leading to b_r values that are less than one.

4.8.1 NON-LTE LEVEL POPULATIONS

These results can be understood in terms of the level populations illustrated in Figure 2. If b_r is less than one, this implies that b(p) for the atom level considered is greater than one. Therefore, the population of the neutral atom levels can be represented by curve 1. The ground state neutral atom level is the most overpopulated and as the energy of the level increases it becomes less overpopulated until close to the ionization limit of the upper neutral atom, levels are in LTE with the ground state of the ion. The ion levels are assumed to be in LTE with the ground state of the ion also.

If the population distribution of neutral atom levels is that of curve 1 in Figure 2 several statements can be made about excitation temperatures measured using a Boltzmann approach. Excitation temperatures measured from the neutral atom levels will be less than the electron temperature because low-lying neutral atom levels are overpopulated. Temperature measured from the lower energy levels will be the lowest because these levels are the most overpopulated. Higher energy levels will be less overpopulated and excitation temperatures from these levels will be greater. Levels close to the ionization limit will have populations that are close to LTE and temperature measurements on these levels will result in the highest excitation temperature. The T_{exc} from the highest energy levels will also approximate the LTE temperature. The experimental results of Alder et al. [53]

and Furuta [61] follow this pattern. Measured Fe I excitation temperatures vary with the energy levels of the lines used. The excitation temperature derived from the high energy lines is larger than T_{exc} derived from a group of medium energy lines, which in turn is greater than T_{exc} from low energy lines. The higher the energy level, the higher the measured excitation temperature. Overpopulation of the lower neutral atom levels can explain these results.

The level population data of Walker and Blades [72] and Schram et al. [23] provide further evidence for this interpretation of atom level populations. Basing LTE on the measured electron density, Walker and Blades find near LTE populations for Fe II levels and high energy Fe I levels. Low energy levels of Fe I are overpopulated with respect to the ion ground level. The lower the energy level the greater the overpopulation factor. Schram et al. observe similar results for the magnesium atom-ion system.

4.8.2 MECHANISMS RESPONSIBLE FOR DEVIATION FROM LTE POPULATIONS

The interpretation of the results presented in this chapter is contrary to previous thought in this area of fundamental studies and will have a significant effect on mechanistic studies and the understanding of non-equilibrium in the ICP. Ion-atom emission intensity ratios are very close to LTE values, not orders of magnitude larger. Thus, mechanisms responsible for non-LTE populations need only produce a relatively small deviation from LTE rather than deviations of one to two orders of magnitude indicated by previous studies. For the most part ion-

atom emission intensity ratios are infrathermal rather than suprathermal and an overpopulation of atom levels is indicated. The emphasis in fundamental studies must shift from looking for mechanisms responsible for suprathermal populations of electron and ions, such as Penning ionization, charge transfer and radiation trapping, to mechanisms causing overpopulation of the atom levels.

The ICP is optically thin for most emission lines, meaning spontaneous radiative decay is not balanced by absorption. This improper balance can lead to a non-LTE population if the rate of radiative de-excitation is significant with respect to collisional decay [40]. The competition between collisional and radiative depopulation determines the degree of deviation from LTE populations. The collisional rate is dependent on n_e and T_e, properties of the electron gas, while A_{qp} reflects atomic properties and is independent of n_e and T_e. A useful way to examine this competition is the number of de-excitation collisions that occur during one radiative lifetime. This is the parameter Ne(p) defined by van der Mullen [38] where

$$Ne(p) = n_e \, K(p) \, / \, A(p) \qquad (4.8)$$

K(p) is the total collisional de-excitation rate coefficient out of level p and A(p) the corresponding total radiative decay rate for the level. If $Ne(p) < 1$ the level is radiative and radiative processes are the dominant depopulation mechanism. If $Ne(p) > 1$ but < 10 the level is collisional and lies in the electron saturation balance regime. If $Ne(p) > 10$ the level p is in LTE with levels above it and the continuum. This is equivalent to

the definition put forward by Griem for defining a level to be in p-LTE [39].

Ne(p) has been calculated for the emission lines utilized in this study. The de-excitation rate coefficient was calculated from an expression given by Yasuda and Sekiguchi [120] where

$$K(p) = 2.37 \times 10^{-21} (\lambda_{qp})^2 [A_{qp}\langle G_{qp}\rangle / E_q (kT)^{1/2}] \qquad (4.9)$$

where E_q (eV) is the excitation energy of the upper level of the transition $q \rightarrow p$, A_{qp} (s^{-1}) and λ_{qp} (angstroms) are the corresponding transition probability and wavelength, T (K) the absolute temperature and $\langle G_{qp}\rangle$ the thermally averaged Gaunt factor. Since all emission lines used originated from the first excited state, only de-excitation to the ground state need be considered and the total rate coefficient for radiative decay was simply the transition probability to the ground state for the level, A_{qp}. Values of $\langle G_{qp}\rangle$ were obtained graphically [22]. For ion levels, $\langle G_{qp}\rangle$ equaled 0.2 and for atoms $\langle G_{qp}\rangle$ ranged from 0.027 to 0.04.

Ne(p) was calculated for both atom and ion levels under the conditions listed in Table IV representing the five different input powers at a spatial position of 16 mm above the load coil in the plasma center. The results are plotted in Figure 22. Figure 22(i) and Figure 22(ii) represent atom and ion levels respectively. As power increased, the electron density increased and the ratio increased for all elements, the higher the electron density the greater the role of collisional de-excitation. Examining Figure 22(i), the results for the atom levels, some interesting features are apparent. The behavior of the five

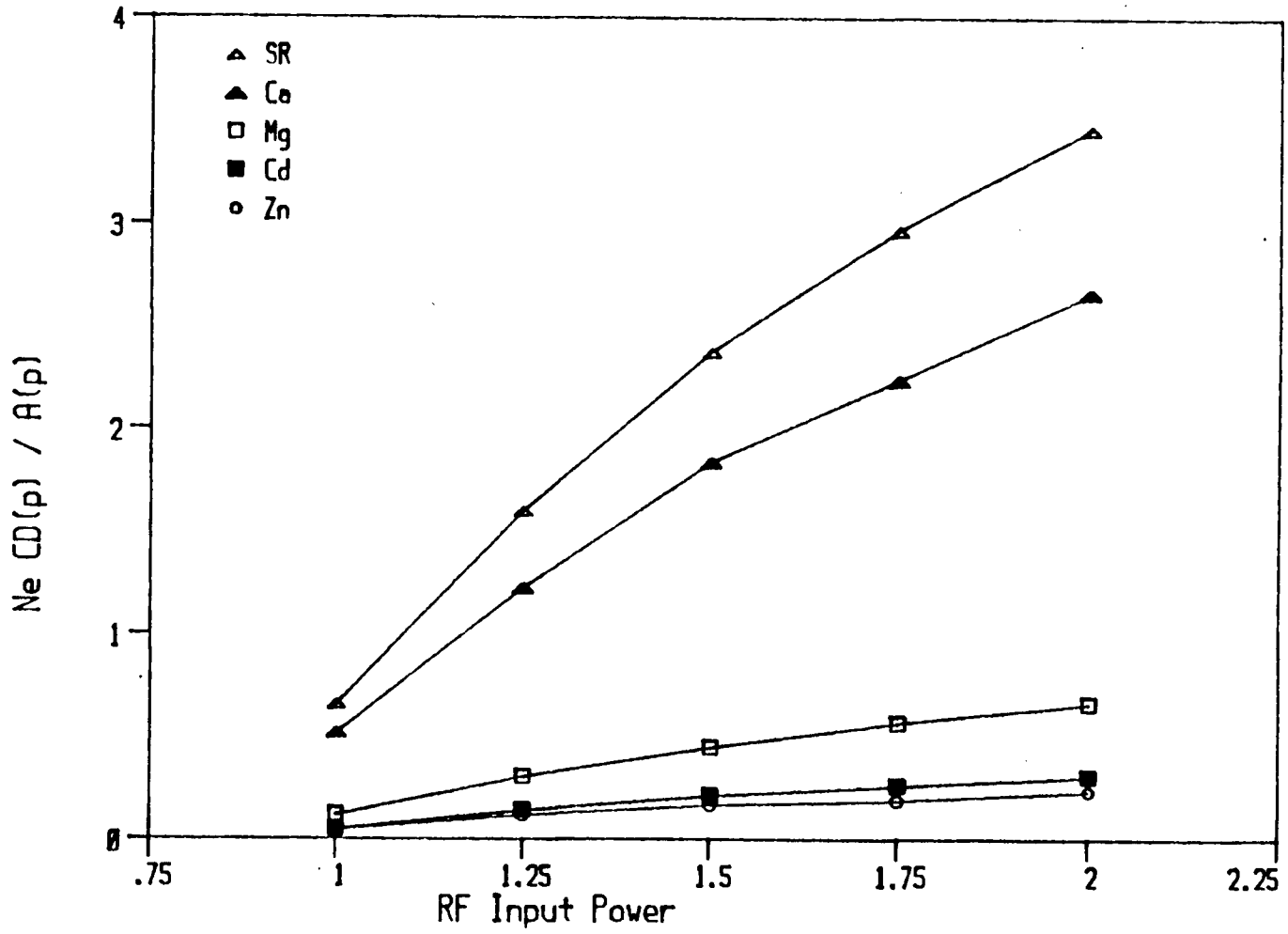

Figure 22(i) Number of de-excitation collisions per radiative lifetime for the first excited state as a function of input power for atoms levels.

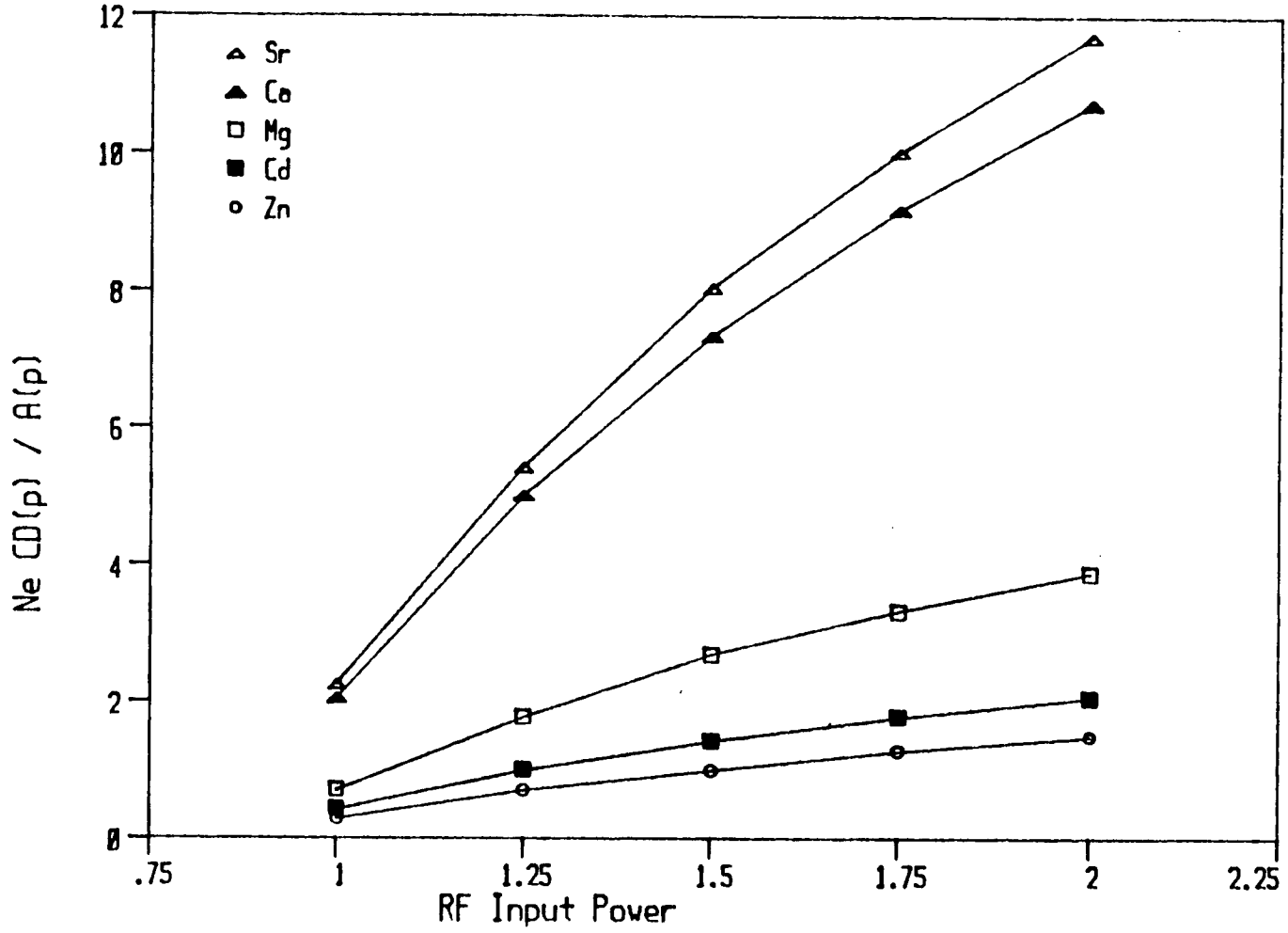

Figure 22(ii) Number of de-excitation collisions per radiative lifetime for the first excited state as a function of input power for ion levels.

elements can be divided into two classes; those with relatively low slope (Mg, Cd and Zn) and those with a higher slope (Sr and Ca). Also, following the same division, the Ne(p) values for Mg, Cd and Zn were less than one for all rf input powers whereas the Ne(p) value for Ca and Sr exceeds one at higher input powers. Mg, Cd and Zn remain in the radiative domain for all input powers. With an increase in power, Sr and Ca move into the electron saturation balance regime and radiative processes play a lesser role in depopulating the level. This classification of Ne(p) behavior correlates extremely well with b_r response reported in Figure 21. For a given power, collisional de-excitation increases in importance as excitation energy decreases for the various elements.

In Figure 22(ii) Ne(p) vs rf input power is plotted for the ion levels. The collisional de-excitation rates were larger for the ion levels than the atom levels chiefly due to the higher Gaunt factors for ion levels. This is a reflection of the higher collisional cross section for a collision between two charged particles as opposed to a collision between a charged particle and a neutral. The higher collisional de-excitation rate resulted in generally higher results for Ne(p). Ne(p) was greater than one for all elements at input powers greater than 1.25 kW. For Sr and Ca the value of Ne(p) exceeded 10 at the very highest powers. Under these conditions the levels can be considered to be in p-LTE with higher energy levels. As for the atom levels, there was a clear distinction between the behavior of Sr and Ca, elements with low excitation potentials and Mg, Cd and Zn, elements with higher excitation potentials. These

results indicate the ion levels are much more likely to be in the collisional regime than atom levels.

These very simplistic rate calculations appear to indicate radiative de-excitation as the process responsible for non-LTE populations in the ICP. In addition, the calculations imply that atom level populations are more affected by non-thermal processes than ion level populations. It will be instructive to examine the results of more complete rate model calculations to see the role radiative decay plays when all levels and processes are considered.

In a recent paper Lovett [36] presents comprehensive calculations for a rate model of the ICP based on an LTE collision-radiative system. His choice of an electron density of 3.34×10^{15} cm^{-3} and a temperature of 8200 K are close to the electron density observed and $T_{e,LTE}$ calculated in this paper for an input power of 1.75 kW. In his model, the atomic ground state of magnesium is found to be about 6% more highly populated than if collisional decay were totally dominant. Lovett finds a general tendency for low energy atomic levels to be more highly overpopulated than higher energy atomic levels. The ground state ion has an LTE population, and excited ion state levels are slightly underpopulated. These results are consistent with infrathermal ion-atom emission intensity ratios. The highly excited levels of the atom are coupled to the ion ground state and maintain a population very close to LTE values. The lower energy levels are less significantly coupled to the ion ground state and are thus overpopulated via radiative decay from the highly excited states. From this, a notion of overpopulated low

energy atomic levels, and ion ground state that have LTE population emerges. The experimental data presented here appears to support the general direction of Lovett's calculations. Lovett concludes the inductively coupled plasma occupies the regime between pure LTE and the corona model. This is exactly what the calculations of Ne(p) indicate.

The calculations of Lovett have been criticized for using an assumed electron density and temperature for the plasma that may not be realistic for the ICP [17]. Hasegawa and Haraguchi [35] measure both electron density and electron temperature then use these experimental values as a basis for their collisional radiative model. They calculate population number densities for argon atom levels. At 15 mm above the load coil in the normal analytical zone, the model calculations indicate a slight overpopulation of low lying argon atom levels caused by spontaneous emission. The results of both rate models are fundamentally the same - near LTE populations of atomic levels with slight overpopulations of the low lying atom levels caused by radiative processes.

4.8.3 B_R VALUES GREATER THAN ONE

The finding of b_r values greater than one for Ca and Sr at high rf input powers seems to contradict the above interpretations of plasma processes. The cause may be related to the role the doubly charged ion plays for these elements of low first and second ionization potential. For strontium at 2.00 kW LTE calculations indicate 83.69% of the total number density is in the form of singly charged ions, 16.22% as doubly charged ions

and only 0.08% as neutral atoms. For these same conditions calcium is 93.92% singly charged ion, 5.91% doubly charged ion and 0.17% neutral atom. Magnesium with a higher ionization potential and even greater second ionization potential has 98.53% singly charged ion, 0.09% doubly charged and 1.38% as neutral atom. A substantial fraction of to the total number density of Sr and Ca exists in the doubly ionized state. The controlling equilibrium for these systems is that between the singly and doubly charged ion levels, not the balance between the atom and singly charged ion [38]. To evaluate LTE for Ca and Sr one should consider the relationship between singly and doubly charged ion levels, the atom level plays only a minor role for these species. Slight deviations in the very small atom populations could produce misleading results as to the true nature of equilibrium in the ICP. Evidence for significant concentrations of doubly charged species is now available from ICP-MS studies [121].

The rate model of Lovett [36] also provides some evidence in this area. His calculations for barium, an element with two low ionization potentials, indicate the doubly charged state and highly excited ion levels to be reasonably well populated. Radiative decay from the highly excited barium ion levels contribute enough to the barium ion resonance level to raise its population above an LTE value. Contributions from the Ba^{+2} ion also act to elevate the ion populations. Strontium with a low ionization energy would be expected to behave much like barium and it is reasonable to observe overpopulations of the ion level relative to LTE at a similar electron density.

As well, the cause of b_r greater than one may be as simple as experimental error. The calculated $(I_i/I_a)_{LTE}$ ratios for calcium and strontium are very sensitive functions of temperature and electron density. For strontium at an input power of 2.00 kW, a 5% increase in temperature results in an $(I_i/I_a)_{LTE}$ value of 528 leading to a b_r value of less than one. The experimental ion-atom ratios were also subject to relatively large error. At the higher input powers, the ratio, $(I_i/I_a)_{exp}$, consisted of a very large ion emission intensity over a very small atom intensity. An error of ± 15% in the ratio would not be unreasonable.

4.9 SUMMARY

The method used to compare measured ion-atom emission intensity ratios with calculated LTE values is a departure from previous approaches to this problem. Measured values of electron density have been used to evaluate an LTE temperature and construct a theoretical LTE framework. Ion-atom emission intensity ratios for a number of elements calculated from this framework have been compared to experimentally measured values.

The main conclusions of this chapter are outlined below.

(a) Ion-atom emission intensities are much closer to LTE values than was previously thought. All of the experimental ion-atom emission intensity ratios were within a factor of 5 of the LTE values.

(b) In general, ion-atom emission intensity ratios appear to be infrathermal rather than suprathermal. In almost all cases the value for b_r was found to be less than one. At a single

power setting the normal analytical zone was the spatial region closest to LTE ($b_r = 1$).

(c) The experimental evidence suggests the atom levels are overpopulated with respect to the ground state of the ion. This non-equilibrium population may simply be the result of a finite contribution from radiative processes to the depopulation of atomic levels, i.e. radiative rates may be comparable, or exceed, collisional rates for some levels, particularly low energy atom lines. Analyte excitation and ionization in the ICP are primarily dominated by electrons, with radiative de-excitation influencing the analyte level populations and giving rise to the observable non-thermal effects.

Chapter 5

ANALYTE IONIZATION IN THE ICP

5.1 INTRODUCTION

The advent of inductively coupled plasma mass spectrometry (ICP-MS) as a routine elemental analysis technique has added a new dimension to fundamental studies of the ICP. This technique establishes a need for better understanding of the performance of the plasma as an ion source ultimately leading to the optimization of plasma design for this role.

The study of the ICP as an ion source with a mass spectrometer as a detector is a new field with few publications as of yet [121,122]. Interpretation of the results of these studies is complex due to possible interferences from processes occurring in the sampling orifice or mass spectrometer. In a recent publication, Gray [123] identifies two aspects of the ICP as a ion source that are poorly understood. One is the high degree of ionization found experimentally and the other, the distribution of ion species in the plasma, especially in the region close to the load coil. Both of these topics are addressed in this chapter.

The concepts developed in previous chapters were used to examine analyte ionization in the ICP and its relationship to the LTE framework based on electron density. LTE degrees of ionization were calculated and experimental degrees of ionization were determined from the ion-atom emission intensity ratio. The two values were compared and the extent of ionization non-equilibrium evaluated for a number of elements. These concepts were extended to gain better understanding of the ICP as

an ion source for mass spectrometry and the relationship between plasma input parameters such as aerosol flow and ion density.

The results presented in the chapter have been previously published [76].

5.2 CALCULATION OF THE DEGREE OF IONIZATION

The degree of ionization, α_j, of species j is defined as

$$\alpha_j = n_{ij} / (n_{ij} + n_{aj}) \qquad (5.1)$$

where n_{ij} and n_{aj} are the density of the singly-charged ion and the neutral atoms of the component j [37]. LTE degrees of ionization were evaluated from the measured electron density and calculated $T_{e,LTE}$ with the following expression

$$\alpha_j/(1-\alpha_j)\ n_e = 4.83\text{x}10^{15}\ T^{3/2}\ Q_{ij}/Q_{aj}\ \exp(-E_{ij}/kT) \qquad (5.2)$$

where E_{ij} (eV) is the ionization potential of species j and Q_{ij} and Q_{aj} are the electronic partition functions for the ion and atom species respectively. Partition functions were taken from deGalan et al. [112].

The experimental degree of ionization was calculated from the experimental ion-atom emission intensity ratio. Since the analyte is characterized by "near" LTE ion-atom emission intensity ratios, the degree of ionization can be evaluated from this intensity ratio if the plasma temperature is known. The degree of ionization, α_j, of species j is given by [37],

$$\alpha_j/(1-\alpha_j) = (I_{qp})_i/(I_{qp})_a\ (g_qA_{qp}/\lambda_{qp})_a\ (\lambda_{qp}/g_qA_{qp})_i$$

$$\text{X}\quad Q_i(T)/Q_a(T)\ \exp\ ((E_{qi} - E_{qa})/kT) \qquad (5.3)$$

where I_{qp} is the emission intensity of the q → p transition, g_q and E_q (eV) are the statistical weight and excitation energy of the upper level of the transition, A_{qp} (s^{-1}) and λ_{qp} (nm) are the transition probability and wavelength of the transition, T(K) is the temperature, and Q(T) is the partition function. The subscripts a and i refer to the atom and singly charged ion of species j. Equation 5.3 is an LTE formula and therefore it is not strictly valid to utilize it to calculate α_j from ion-atom emission intensities that have already been demonstrated to be non-LTE. However, since these ratios are "close" to LTE, the equation can be used to estimate the experimental degree of ionization with reasonable accuracy. The temperature used for these calculations was the temperature derived from the electron density, $T_{e,LTE}$.

5.3 EXPERIMENTAL

Experimental ion-atom emission intensity ratios obtained in Chapter 4 for Section 4.7 were used to generate the degree of ionization for the five elements Sr, Ca, Mg, Cd and Zn.

For Section 5.5 lateral intensities of the cadmium 228.8 nm atom line and the cadmium 226.5 nm ion line were measured at 150 spatial positions across the plasma for vertical heights of 4, 8, 12, 16 and 20 mm above the load coil at rf input power of 1.25 kW. The lateral intensity profiles were converted to radial profiles using an Abel inversion. This was done at aerosol flow rates of 0.6, 0.8 and 1.2 l m^{-1}. The plasma gas flow and auxiliary gas flow were maintained at 11 l m^{-1} and 0.3 l m^{-1}, respectively. Experimental ion-atom emission intensity ratios

were used to generate degree of ionization plots for cadmium.

5.4 DEGREE OF IONIZATION FOR A NUMBER OF ELEMENTS

An interesting feature of the data provided in chapter 4 is that the value of b_r is apparently a function of the ionization energy of the species. In general, b_r increased as the ionization energy of the atom species decreased, although Cd appears out of sequence. The relationship between ionization energy and deviation from LTE was further explored with the concept of degree of ionization.

5.4.1 RESULTS

The results of the degree of ionization calculations, in %, for Sr, Ca, Mg, Cd and Zn at rf input powers of 1.0, 1.25, 1.50, 1.75 and 2.00 kW, at 16 mm above the load coil in the center of the plasma are provided in Table VII. Experimental values were derived from the ion-atom emission intensity ratios presented in Chapter 4 and the LTE values calculated from the corresponding electron density and temperature presented in Table IV. The final column of the table is an estimate of the uncertainty in the α values. For the experimental values, error was calculated using an uncertainty in temperature of ± 2000 K to indicate the uncertainty introduced by assuming $T_{exc} = T_{e,LTE}$. The experimental error in electron density, ± 9%, was propagated through the LTE calculations to arrive at the uncertainty in LTE degree of ionization. Uncertainties in absolute gA values are in the range of ± 25%. However, since the calculation involves the ratio of gA values, the impact of this uncertainty is greatly

Table VII

Experimental (α_{exp}) and LTE (α_{LTE}) degree of ionization in per cent for Sr, Ca, Mg, Cd and Zn at input powers of 1.00, 1.25, 1.50, 1.75 and 2.00 kW.

Power (kW)		1.00	1.25	1.50	1.75	2.00	Uncertainty
Sr	α_{exp}	99.40	99.62	99.84	99.87	99.88	±0.02
	α_{LTE}	99.88	99.85	99.84	99.83	99.82	±0.04
Ca	α_{exp}	98.90	99.44	99.65	99.73	99.77	±0.03
	α_{LTE}	99.81	99.76	99.74	99.73	99.72	±0.05
Mg	α_{exp}	93.00	94.39	96.22	96.77	97.03	±0.26
	α_{LTE}	98.33	98.36	98.37	98.37	98.37	±0.42
Cd	α_{exp}	--	85.99	88.43	90.29	91.46	±0.24
	α_{LTE}	89.39	91.35	92.06	92.45	92.76	±1.35
Zn	α_{exp}	--	63.89	72.30	77.39	79.40	±3.23
	α_{LTE}	81.96	85.66	86.98	87.71	88.20	±2.12

reduced.

The trends in the LTE degrees of ionization values can be understood in terms of the relative effects of electron density and temperature. An increase in electron density (with power) acts to shift the ionization equilibrium toward the atom species. Counteracting this is the effect of temperature which, as it increases with power, tends to shift the equilibrium toward the ion species. These two opposing effects combine to produce the value listed in the table. The effect of electron density is greater for elements with low ionization energy (Sr and Ca) and so the LTE value of α decreases with increasing power. Mg is at a balance point where the two factors oppose each other equally and the LTE α is constant as a function of power, and for Cd and Zn, the effect of temperature wins out (due to the higher ionization energy) and the degree of ionization increases with rf power.

For the experimental values, two trends are evident. First, as power, and hence n_e, increased, the degree of ionization increased for all the elements. Second, the ordering of α was consistent with the ionization energy of the element; being the highest for Sr, which has the lowest ionization energy, and the lowest for Zn, which has the highest ionization energy. This ordering is the same as that recently reported by Houk and Olivares [124]. These authors also discuss the importance of the degree of ionization relative to the vertical spatial structure of analyte emission.

In Figure 23 the ratio of the experimental degree of ionization (α_{exp}) to the LTE degree of ionization (α_{LTE}) has been

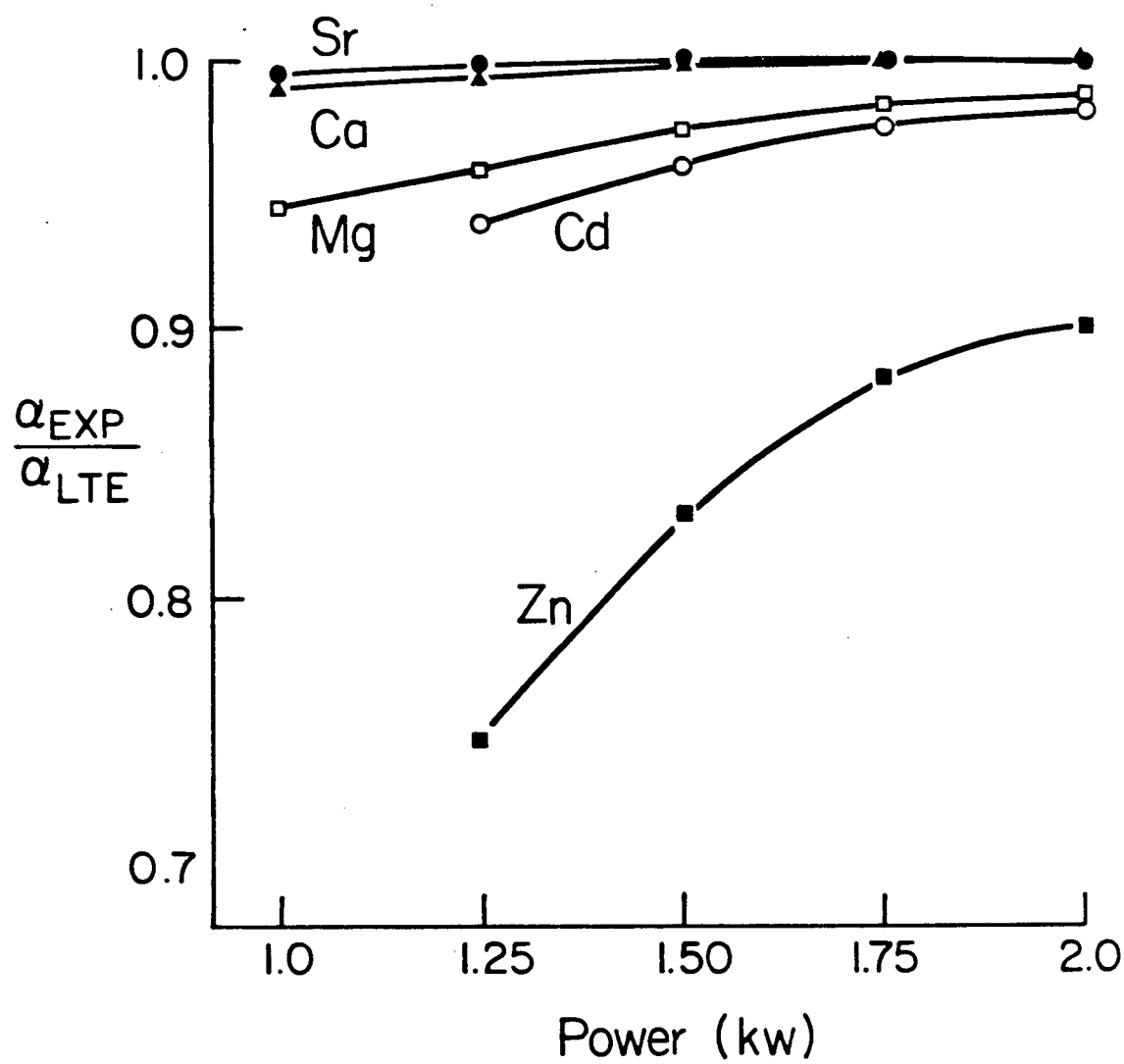

Figure 23 Ratio of experimental degree of ionization (α_{exp}) to LTE degree of ionization (α_{LTE}) as a function of power.

plotted as a function of rf input power. A ratio of one implies LTE. The departure is very small for Sr and Ca, which have low ionization energies and increases with ionization energy in the order - Mg, Cd and Zn. Deviation from LTE correlates well with ionization energy and Cd is not out of order as it was on the b_r plot in Figure 21. In general, elements were underionized relative to LTE values.

The evaluation of degree of ionization in this manner has provided some insight into the b_r plot provided in Figure 21. The value for b_r indicated that experimental ion-atom emission intensity ratio for Sr differ from LTE values by a factor of 1.5 at an input power of 2.00 kW. The experimental degree of ionization was 99.88% and the LTE value is 99.82%. Sr was only 0.06% overionized relative to LTE; this 0.06% overionization, however, led to ion-atom emission intensity ratios greater than LTE values by 50%. This occurred because of the very small atom population and large ion population, slight changes in the atom population produced large changes in the ratio. For Zn at 2.00 kW, even though the experimental degree of ionization was substantially different from the LTE case, 79.40% as compared with 88.20%, the effect on b_r was not as significant as with Sr because the relative ion and atom populations were much more equal.

The high degree of ionization in Table VII indicates that the ICP is a very effective source for ionizing analyte and one can understand why mass spectrometry is a very powerful detection method when used with an ICP source. These experiments show that for analyte with ionization energies up to 9.5 eV the degree of

ionization is greater than 60%. Figure 24 summarizes the functional dependence of the degree of ionization on analyte ionization energy for an input power of 1.25 kW. The data in Figure 24 are consistent with reports that similar ion counts are found for equimolar concentrations of elements with ionization potentials less than 8 eV [125]. Figure 24 also bears a striking resemblance to previously published figures [126,127] of signal versus ionization potential for equimolar concentrations of elements.

The small departures from LTE observed in this work and the strong correlation with ionization potential suggest it would be possible to predict with a high degree of confidence degrees of ionization for elements not studied here.

5.4.2 DISCUSSION

In the previous chapter, deviations from LTE were attributed to radiative decay and a correlation with excitation energy of the first excited state was drawn. This interpretation of non-equilibrium in the ICP did not consider radiative recombination from ion levels into atom levels. The ICP occupies the regime where both three body and radiative recombination are important [36]. Thermodynamic equilibrium is derived based on the principle of detailed balancing applying to all excitation, de-excitation, ionization and recombination processes. The ICP is optically thin so that radiative emission processes are not balanced by the respective absorption process. Therefore in order for LTE to be attained, collisional processes must dominate for both excited state depopulation and ion recombination. The

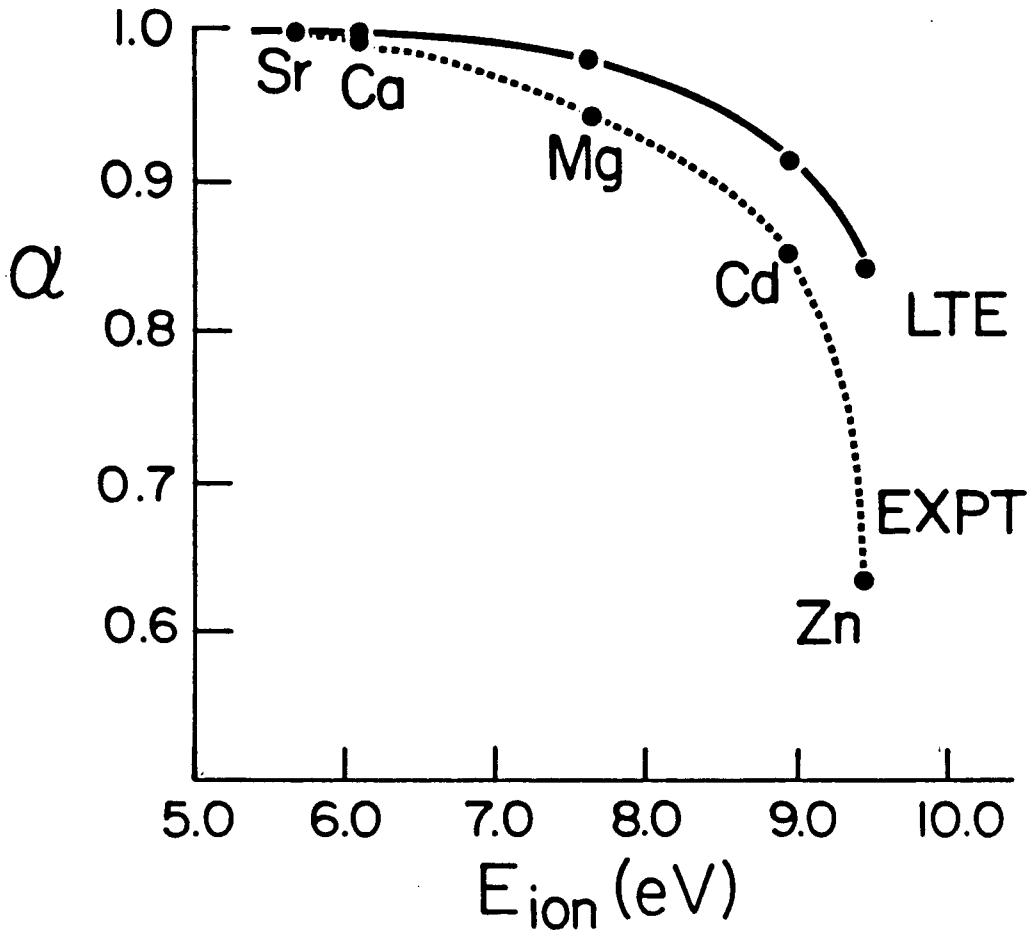

Figure 24 Degree of ionization as a function of ionization potential at 1.25 kW. Solid line represents LTE calculation, dashed line represents experimental results.

electron density must be high enough such that three-body recombination is dominant over radiative recombination, and collisional de-excitation over radiative decay. In the analytical ICP the electron density is not high enough to fulfill this condition so that analyte is underionized relative to LTE [40,73]. The degree to which a particular analyte departs from LTE will depend on the relative rates of collisional and radiative processes. Since ionization energy and excitation energies of Sr are lower than those of Zn, the depopulating processes for Sr become collisionally dominated at lower electron densities than for Zn.

The rate calculations of Lovett [36] indicate that the effect of radiative recombination not being balanced by photoionization is a general tendency to increase populations of atom levels and greatly decrease the doubly charged ion level. The result is an increase in overpopulation of low lying atom levels and for elements with a significant number of doubly charged ions an increase in the population of ion levels as well. The net result is ionization non-equilibrium. The magnitude of the effect is a function of the first and second ionization potential of the element. Radiative recombination as well as radiative decay processes contribute to the overpopulations observed for the atom levels.

5.5 IONIZATION OF CADMIUM

5.5.1 DEGREE OF IONIZATION

The development of the ICP as an ion source for mass spectrometry has added a new dimension to plasma source atomic spectrometry [13,121,123,125,128]. As with optical ICP spectrometry, optimization of the analytical signal (ion count in the case of ICP-MS) is an important exercise preceding routine use. Horlick et al. [121] identify the important plasma parameters influencing ion counts in ICP-MS as: rf input power, aerosol flow rate, and extraction height (analogous to optical viewing zone) above the load coil. It is important to understand how ions are distributed in the ICP source itself so that ICP-MS users may feel comfortable that the chosen operating parameters produce ion counts that are consistent with actual ion distributions in the aerosol channel.

In order to investigate analyte ionization in the ICP the ion-atom emission intensity ratio of cadmium was used to produce spatial maps of degree of ionization. Cadmium was chosen for this study because of the near equivalence of energies of the ion and atom levels. In Eqn 4.1 it can be seen that if the excitation energy of the ion and atom line are equal or very close the effect of temperature in determining α becomes insignificant. CdI (228.8 nm) and CdII (226.5 nm) have a difference in excitation energy of only 0.05 eV. For a given measured ion-atom emission intensity ratio, varying the temperature from 7000 to 9000 K produces only a 0.13% change in estimated degree of ionization. Thus knowledge of an accurate temperature for the α calculation is not an important factor. As

a result the actual degree of ionization of cadmium in the plasma can be measured with no knowledge about the exact plasma temperature.

Cadmium ion-atom emission intensity ratios were collected for 150 positions across the plasma at 5 heights above the load coil - 4, 8, 12, 16 and 20 mm, at three different aerosol flow rates - 0.6 l m^{-1}, 0.8 l m^{-1} and 1.2 l m^{-1}. The ratios were used to calculate degree of ionization at each spatial position and the results for each aerosol flow rate combined to produce contour maps of α. The contour maps were computer generated using a contour plotting routine [82]. Figures 25(i), 25(ii) and 25(iii) are degree of ionization plots for aerosol flow rates of 0.6, 0.8 and 1.2 l m^{-1} respectively. The numbers on the contour lines are percent degree of ionization.

At an aerosol flow rate of 0.6 l m^{-1} (Fig. 25(i)) the maximum α, 92%, occurred in the center of the plasma, 4 mm above the load coil. α decreased with both vertical height and radial distance from plasma center to a minimum of 83% at the edge of the plasma. The contour lines give the appearance of a series of stacked cones.

The contour plot for 0.8 l m^{-1} aerosol flow rate (Fig. 25(ii)) was significantly different. At 4 mm above the load coil there was a high degree of ionization off axis at $\pm$ 4 mm from the plasma center. The minimum for α actually occurred at the center of the plasma in the aerosol channel. The degree of ionization increased with increasing height up the center axis of the plasma to a maximum of 89% at 16-20 mm above the load coil. Above 8 mm, α decreased from the center to the outside edges of

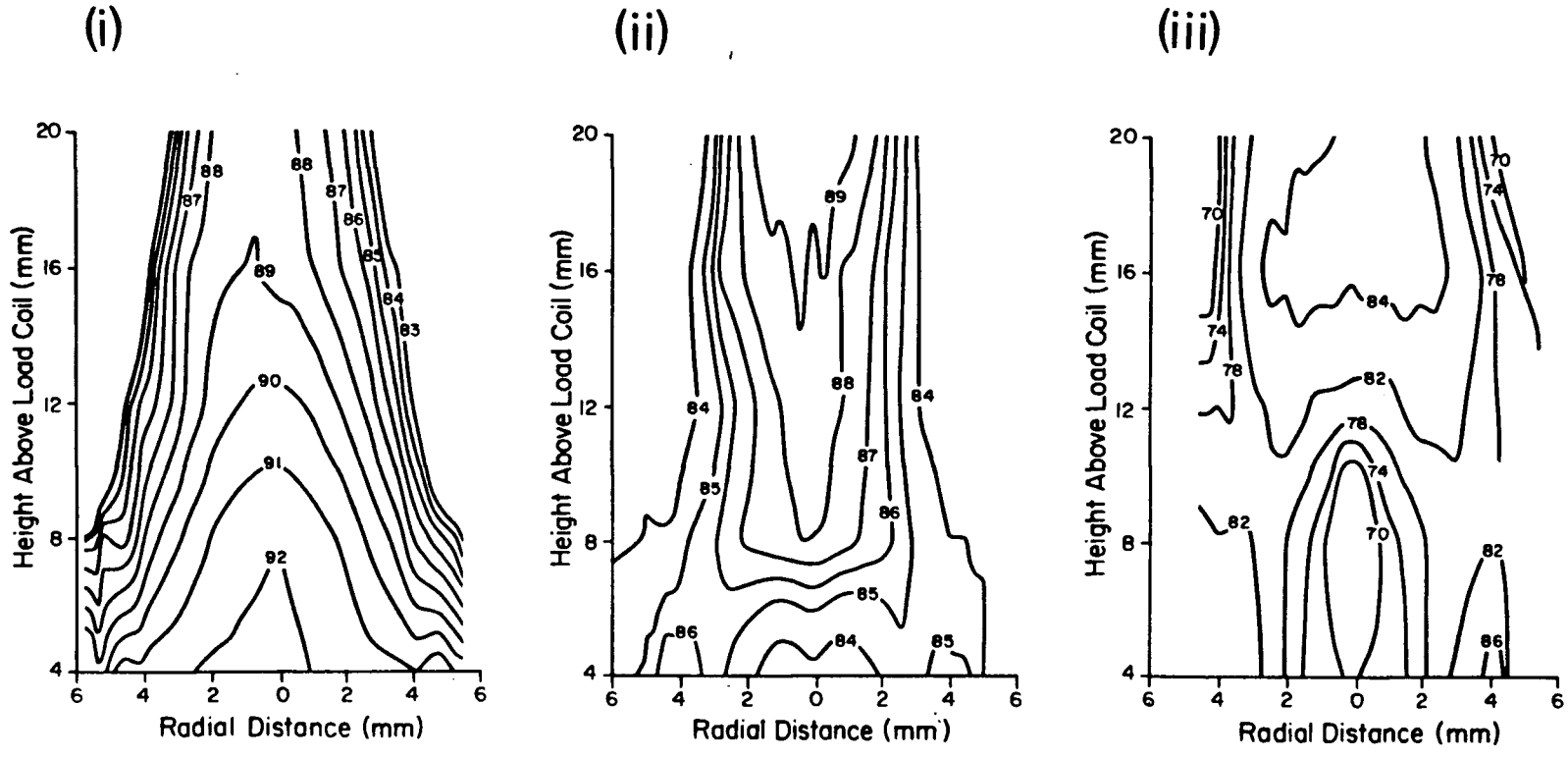

Figure 25 Isocontour plots of cadmium degree of ionization (in per cent) for 1.25 kW input power. Aerosol flow rate - (i) 0.6 l m^{-1}, (ii) 0.8 l m^{-1} and (iii) 1.2 l m^{-1}.

the plasma.

With an aerosol flow rate of 1.2 l m^{-1} (Fig. 25(iii)) the degree of ionization ranged from 70 to 84%. There was a tongue of low degree of ionization in the central channel of the plasma extending from 4 to 8 mm above the load coil. Above this tongue α increased with height to a maximum of 84% at 16-20 mm above the load coil. The tongue of low α at the 1.2 l m^{-1} aerosol flow rate can be related to the large amount of cold gas and aerosol vapor entering the aerosol channel. It takes longer to heat and ionize the analyte and so ionization takes place higher in the plasma. At 0.8 l m^{-1} less aerosol gas was being fed into the plasma so the tongue was much smaller and a higher degree of ionization occurred.

5.5.2 SPATIAL DISTRIBUTION OF NUMBER OF IONS

In ICP-MS the spatial position and operating conditions that produce maximum degree of ionization are not as important as the position and conditions for maximum number density of ions. The degree of ionization contour plots have indicated areas of high α. Areas of high ion number density will be influenced by conditions such as nebulizer efficiency for the different flow rates, sample loading, aerosol injection velocity and diffusion of analyte in the plasma as well as degree of ionization. The regions where high α is observed (off axis region) 4 mm above the load coil for 0.8 and 1.2 l m^{-1} aerosol flow rates are unlikely to contain a large number of ions because analyte will not be found there to any significant extent.

The emission intensity of an atom or ion line is

proportional to the total number of species in that ionization stage [37]. The relationship is given by:

$$I_{qp} \propto (A_{qp}g_q / \lambda_{qp} Q(T)) n_T \exp(-E_q/kT) \quad (5.4)$$

where I_{qp} is the intensity of the q → p transition, g_q and E_q (eV) are the statistical weight and excitation energy of the upper level of the transition. A_{qp} (s^{-1}) and λ_{qp} (nm) are the corresponding transition probability and wavelength, T(K) the absolute temperature, Q(T) the internal partition function, and n_T the total number of species in the ionization stage under consideration.

Using relative radial emission intensities of the cadmium ion line (226.5 nm) at various spatial positions in the plasma and the $T_{e,LTE}$ temperatures derived from the corresponding electron densities, discussed in Section 3.5.3, the relative number of cadmium ions were calculated for the three aerosol flow rates. Figures 26(i), 26(ii) and 26(iii) are contour plots of relative number of cadmium ions at an input power of 1.25 kW for flow rates of 0.6, 0.8 and 1.2 l m^{-1}, respectively. The numbers on the contour lines are relative number of ions and have been scaled so values can be directly compared between figures.

It should be recognized that these calculations involve the use of an LTE formula in a non-LTE situation. However, it has been previously shown that cadmium ion-atom ratios are very close to LTE values, thus the equation can be used to estimate relative number of cadmium ions with reasonable accuracy.

At 0.6 l m^{-1} aerosol flow rate a maximum relative number of ions of 40 was observed in the central channel 6-10 mm above the

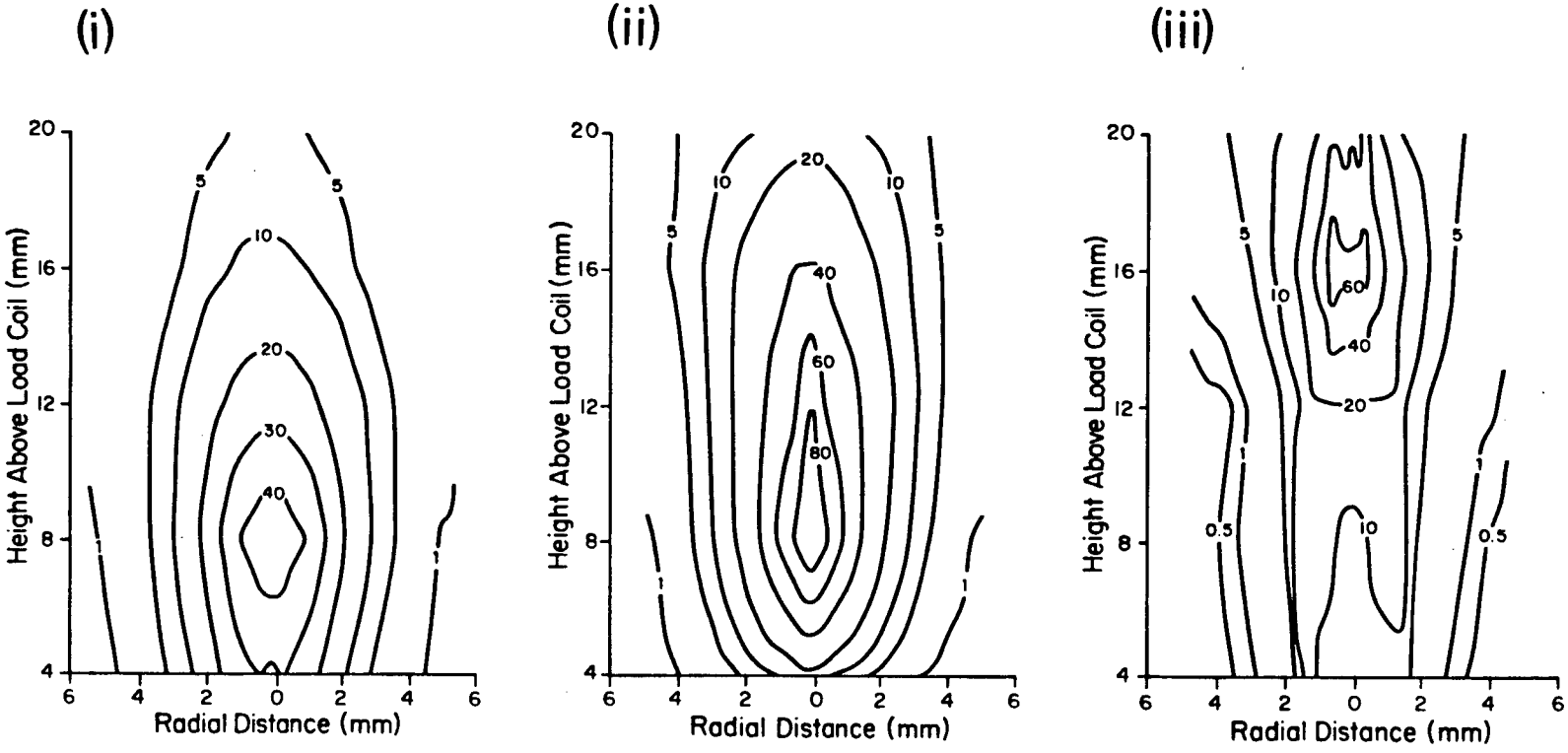

Figure 26 Isocontour plots of relative number of cadmium ions. Aerosol flow rate - (i) 0.6 l m^{-1}, (ii) 0.8 l m^{-1} and (iii) 1.2 l m^{-1}.

load coil. The number of ions decreased with increasing height and distance from the load coil. For 0.8 l m^{-1} the maximum number of ions was 80. The maximum number density was found in a narrow region along the plasma center 8-12 mm above the load coil. Ion density decreased above and below this region and towards the edge of the plasma. There was less time for lateral diffusion of the analyte at the higher aerosol flow rate so the contour lines in Fig. 26(ii) have a more elongated appearance than those in Fig. 26(i).

The contour plot of relative number of ions for 1.2 l m^{-1} aerosol flow rate was significantly different in shape compared to the others. The maximum number of ions occurred high inthe central channel of the plasma at 16 mm above the load coil. Below this and toward the aerosol channel edges ion density decreased. There was a tongue of a relatively low ion density, less than 10, in the central aerosol channel extending up to 8 mm above the load coil. The high aerosol flow rate and low electron density prevent significant ionization until fairly high up in the plasma.

The areas of maximum ion density correspond to optimum sampling position for an ICP-MS system. All the maxima occur on the central plasma axis, but at different heights for each aerosol flow rate. For increased aerosol flow rate the sampling height would have to be increased. Based on relative ion density the best conditions for ion sampling would be at 10-12 mm above the load coil with an aerosol flow rate of 0.8 l m^{-1}. At a flow rate of 1.2 l m^{-1} a sampling height of 16-18 mm would be optimum. This was not the ordering suggested by the degree of ionization

data and reflects the importance of sample loading and diffusion of analyte species in the plasma.

Optical absorption and fluorescence studies show the spatial position of ion emission intensity does not always correlate completely with spatial position of ground state ion density [79,108,129]. The reason for this is the exponential influence temperature has on excited state populations, and hence emission intensity. This is especially important at low vertical heights where analyte is chiefly confined to the central channel, a low temperature region, but off-axis high temperatures are encountered. The high off-axis temperatures lead to off-axis maxima for emission intensity. The degree of ionization profiles for Cd behave in a similar manner. In absorption studies, ion ground state density is greatest along the central axis of the plasma under most conditions [108,129]. The relative ion density calculated from the intensity measurements agrees with this. The factoring of emission intensity with an appropriate temperature, $T_{e,LTE}$, allows a reasonable estimate of number density of species. For a more accurate measure of ion distribution it would be preferable to measure the number of ions by absorption or laser studies.

The changes in relative ion density with spatial position evaluated above have been compared to published ICP-MS data that reports variance of ion count with respect to the spatial position of the sampling aperture. Gray and Date [125] operated a plasma at 1.20 kW input power with an aerosol flow rate of 0.6 l m^{-1} and plot % ion count response versus radial distance for MS sampling in the continuum mode at 4 heights above the load coil.

Figure 27 is a plot of the relative number of ions based on measured Cd ion density derived above for 1.25 kW input power at an aerosol flow rate of 0.6 l m^{-1} for vertical heights of 5, 10, 15 and 20 mm above the load coil. The curves for 10, 15 and 20 mm have a very good agreement in shape and relative intensity compared with those of Gray and Date. At 5 mm above the load coil, they observe a much greater percent response and sharper drop in response with distance from the central plasma axis than is shown in Fig. 27. If the relative number of ions for 8 mm above the load coil were plotted, instead of 5 mm, their pattern of response would have been duplicated. The small difference in response may have been due to the slight differences in equipment, cross flow vs concentric nebulizer, or diameter of aerosol injection tube. The close agreement between the two methods of measuring number of ions suggests the calculation of relative number of ions from CdII emission intensity was valid and the continuum sampling mode used by Gray and Date accurately samples ion density in the plasma.

By interpreting plasma characteristics using a model based on measured electron density and a temperature calculated from this value, emission intensity data has been reconciled with mass spectrometry data as well as absorption and fluorecsence studies. The electron density based model correctly predicted that the greatest concentration of the ion species existed in the central channel. The high off-axis emission intensity observed close to the load coil was a consequence of the very high temperature in this region compared to the central channel.

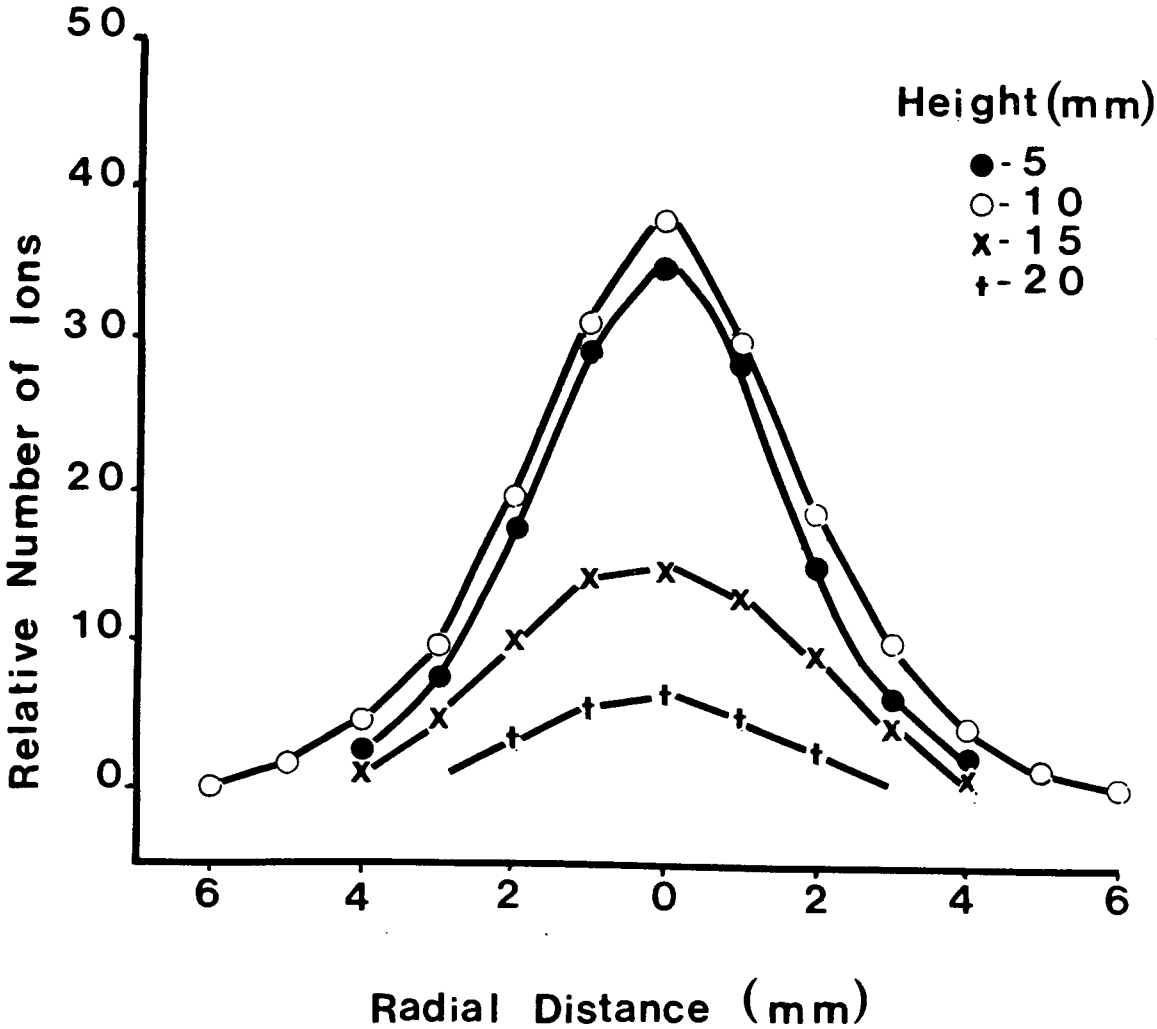

Figure 27 Relative number density of cadmium ion as a function of radial position at various heights above the load coil for an aerosol flow rate of 0.6 l m^{-1}. Height above load coil: (●) 5 mm, (○) 10 mm, (×) 15 mm and (+) 20 mm.

5.6 SUMMARY

Experimental ion-atom emission intensity ratios have been used to evaluate the degree of ionization for a number of elements. An LTE degree of ionization was calculated from the measured electron density and corresponding $T_{e,LTE}$. The results indicate that for the most part analyte is underionized relative to the LTE case. The relative degree of underionization correlates with ionization potential; the higher the ionization potential the greater the departure from LTE. The cause of this departure from LTE is believed to be due to finite contributions from radiative processes to overall depopulation rates.

The concepts of the LTE model were used to determine the relationship between spatial position, aerosol flow rate and position of maximum ion count for the ICP. The results are in agreement with ICP-MS observations. This new understanding of plasma processes has provided insight into the ICP as an ion source. The use of the above described procedures elucidates and predicts the high degree of ionization observed experimentally and the distribution of ion species in the plasma.

Chapter 6

ELECTRON DENSITY MEASUREMENTS USING Ar I LINE BROADENING

6.1 INTRODUCTION

A variety of sample introduction techniques have been developed and investigated to improve and extend the analytical capabilities of inductively coupled optical emission spectroscopy (ICP-OES). Microliter volumes of solution samples have been analyzed by electrothermal vaporization (ETV) techniques [130-134] and graphite cup, direct sample insertion methods [135,136]. Vapor introduction techniques for stable hydride-forming species, have been used successfully with the ICP to improve detection limits [137-139]. Direct solid sampling in ICP-OES has also been accomplished by external vaporization using laser [140-142] and spark [143-145] ablation. One common factor among these methods of sample introduction is that the sample is introduced into the plasma without solvent. This means that the sample entering the plasma is composed of particles of dry aerosol, unlike that produced by more conventional nebulization, where solvent accompanies the sample into the plasma. A thorough understanding of plasma excitation conditions and their relationship to solvent-plasma, vapor-plasma, and aerosol-plasma interactions will be extremely valuable in the optimization and improvement of these new sample introduction processes [146].

It is possible that the absence of solvent in the plasma could have a significant effect on the discharge characteristics. First, any solvent present will contribute to the total heat capacity of the material present inside the plasma toroid. In addition, energy will be consumed in the processes of solvent

desolvation, vaporization, and dissociation, so that when solvent loading in the plasma reaches a certain level a substantial amount of the power available will be consumed by these solvent decomposition processes. The balance between thermal conduction and power dissipation determines the plasma temperature [37]. On this basis one could expect an increase in excitation temperature and thus electron density when solvent is removed. Balancing this process is the production of electrons by the ionization of the decomposition products of the solvent, in this case water.

A number of studies have explored the interaction of organic solvents and the plasma and made some comparisons with plasmas having water as a solvent [58,147-149]. The effect of water and water vapor itself on plasma excitation is less well understood.

Electron density (n_e) is a parameter of prime importance in determining plasma excitation conditions since analyte excitation and ionization is accomplished primarily by collisions with electrons [38]. A number of recent publications [51,73,75,76] show electron density to be essential in understanding plasma excitation. Measurement of electron density with and without water vapor present in the aerosol gas should provide valuable information about plasma conditions and the effect of water in creating and maintaining these conditions. Alder et al. [53] have studied the effect of water on electron density, cadmium ionization, and iron excitation temperatures at different viewing heights in the plasma. The presence of water in the aerosol was noticeable at all heights and acted to increase electron density and ionization and excitation temperatures in the ICP. Tang and Trassy [150] also record higher excitation temperatures when

water vapor is in the aerosol channel. Long et al. [151] observed an increase in electron density with increasing water vapor in the aerosol gas flow. In these studies the electron density was measured at only a limited number of spatial positions in the plasma. Significant differences in the electron density may be occurring in other spatial regions of the plasma which are not observed due to the lack of radial resolution in these studies. A thorough understanding of the effect of water on plasma discharge characteristics requires a knowledge of changes in n_e, caused by the presence of water, at all spatial positions.

In addition, the contribution of water and its dissociation products to the total electron density has a relationship to the LTE framework and plasma model developed in the previous chapters. $T_{e,LTE}$, which is the basis of the LTE framework, was calculated assuming only argon contributes to the plasma electron density. If ionization of hydrogen and oxygen from the aspirated water provide a significant portion of the overall electron density the equations for calculating $T_{e,LTE}$ must be amended to include the Saha equation for both oxygen and hydrogen and a mass balance equation. This will result in a different value for LTE temperature.

When water vapor is present in the plasma, n_e can be readily measured from the Stark broadening of the H_β line at 486.13 nm. Elimination of water vapor from the aerosol gas removes a convenient source of hydrogen for the measurement. Hydrogen gas could be admixed with the plasma gas but even small amounts of molecular hydrogen produce dramatic changes in the plasma [88]. In Section 3.5.5 it was found that as little as

0.5% H_2 increased electron density by 30%. A better alternative is to use the Stark broadening of argon lines to measure electron density. Kalnicky et al. [67] made limited measurements of electron density from argon line broadening and obtained good agreement with results from H_β. Mermet [85] used argon line broadening to measure electron density for a number of different aerosol flow rates ranging from 0 to 2.5 l m^{-1} in a high frequency inductively coupled plasma. In this chapter argon line broadening was utilized to measure radially resolved electron densities with both wet, and dry aerosol gas to determine the influence of water vapor on the magnitude and spatial distribution of electron number density.

6.2 Calculation of Electron Density from Argon Line Broadening

Stark broadening of argon lines has not been as widely used as broadening of the H_β line to evaluate electron density. A brief discussion of the theory behind the measurement follows. The theory of Stark broadening of isolated spectral lines from heavier elements in a plasma has been discussed extensively [91-95]. The theory for multielectron atomic species is not as well developed as that for atomic hydrogen. For heavier elements somewhat larger errors in the calculated line profiles can be expected from uncertainties in the atomic matrix elements required to compute the perturbation. Comparison of experimental results with calculated half-widths suggests an accuracy of about 20% in electron density measurements from these lines [95].

For neutral atom emitters the Stark half widths (FWHM) are given approximately by [95]:

$$\Delta\lambda S_{1/2} \simeq 2[1 + 1.75\times10^{-4} n_e \alpha(1 - 0.068\ n_e^{1/6} T^{-1/2})]10^{-16}\omega n_e \quad (6.1)$$

where $\Delta\lambda S_{1/2}$ - Stark half width (nm)

ω - electron impact width (nm)

α - ion broadening parameter

n_e - electron density (cm^{-3})

T - temperature (K)

provided a number of validity criteria are met [94]. These are 1) the time dependence of the ion field can be neglected, 2)the ion broadening parameter is less than 0.5 and 3) the ratio of the mean distance between ion to Debye radius, which is a measure of ion-ion correlations and Debye shielding, is less than 0.8. Griem [94] has provided equations to determine the validity criteria and calculations show these conditions are all fulfilled for argon lines over the range of electron densities and temperatures encountered in the ICP.

The parameters α and ω are tabulated by Griem for a number of argon lines [91,92]. The numerical dependence of α and ω on electron density and temperature has already been incorporated into Eqn. 6.1 so parameters can be taken directly from the tables, without multiplication.

Line profiles of the argon lines and lines from other heavier elements are primarily determined by electron broadening which results in an approximately Lorentzian shape. The contribution of ion broadening to the widths of the argon lines can cause some asymmetry in the profiles but it is usually small. Doppler and instrumental contributions to the line profile are

both Gaussian. Thus experimental argon line profiles can be assumed to be Voigt profiles.

Calculated Stark half widths have been compared to experimental results for a number of argon lines [94]. The ratio of experimental to theoretical half widths, averaged over thirteen lines, is 0.95. However for individual lines there are deviations up to 30%. For this reason it is recommended that more than one line be used to determine electron density.

6.3 EXPERIMENTAL

For this series of experiments the 1-meter monochromator and 4096 linear photodiode array (LPDA) were used to detect the plasma radiation. The LPDA had 4096 discrete photodiodes and was mounted horizontally in the exit focal plane of the monochromator such that, when read out, it provided a simultaneous measure of the emission spectrum over a wavelength range of approximately 45.0 nm. The complete experimental system for collection of intensity data has been previously described [72]. An instrumental line profile halfwidth of 0.033 nm was observed for the photodiode array spectrometer for entrance-slit dimensions of 0.050 X 1 mm.

The gas flows used for all measurements were 11 l m^{-1} plasma gas, 0.3 l m^{-1} auxiliary gas and 0.9 l m^{-1} aerosol gas.

The method for calculating n_e spatial profiles from H_β broadening has been previously described in Section 3.3.

To obtain spatially resolved electron density values from argon line broadening, the Ar I lines at 542.14 and 549.59 nm were simultaneously sampled at 25 wavelength points across each

line profile, at 150 lateral positions across the discharge. In each case, the plasma background was subtracted by interpolating from the continuum emission on both sides of the line wings at a distance of 0.6 nm from the line center.

To obtain radially resolved electron density information, the 150-point lateral spatial profiles for each wavelength position were smoothed by a 13-point simplified least squares procedure [78] and the smoothed lateral wavelength profiles Abel inverted [74]. For each of the resulting 150 radial points the argon line profiles were reconstructed, and the radially resolved half width evaluated. Experimental Stark half-widths were deconvoluted from the experimental half-width using tabulated half-width ratios for Voigt, Gaussian and Lorentzian contributions available in reference [101]. The experimental Stark half width was then substituted into equation 6.1 and the electron density calculated.

6.4 RESULTS

6.4.1 ELECTRON DENSITY WITH WATER VAPOR IN THE AEROSOL GAS

A representative spectrum of the wavelength region from 540 to 557 nm is presented in Figure 28. The major argon emission lines are identified in the figure. The Ar I 542.135 and 549.588 nm lines were employed for electron density determinations. Among argon lines for which Stark parameters are tabulated these two lines have close to the largest electron width parameters (ω) and thus will be the broadest and most sensitive to electron density changes. They are also of sufficient intensity to allow the measurement of the half widths. The nearby 553.45 nm Ar I line

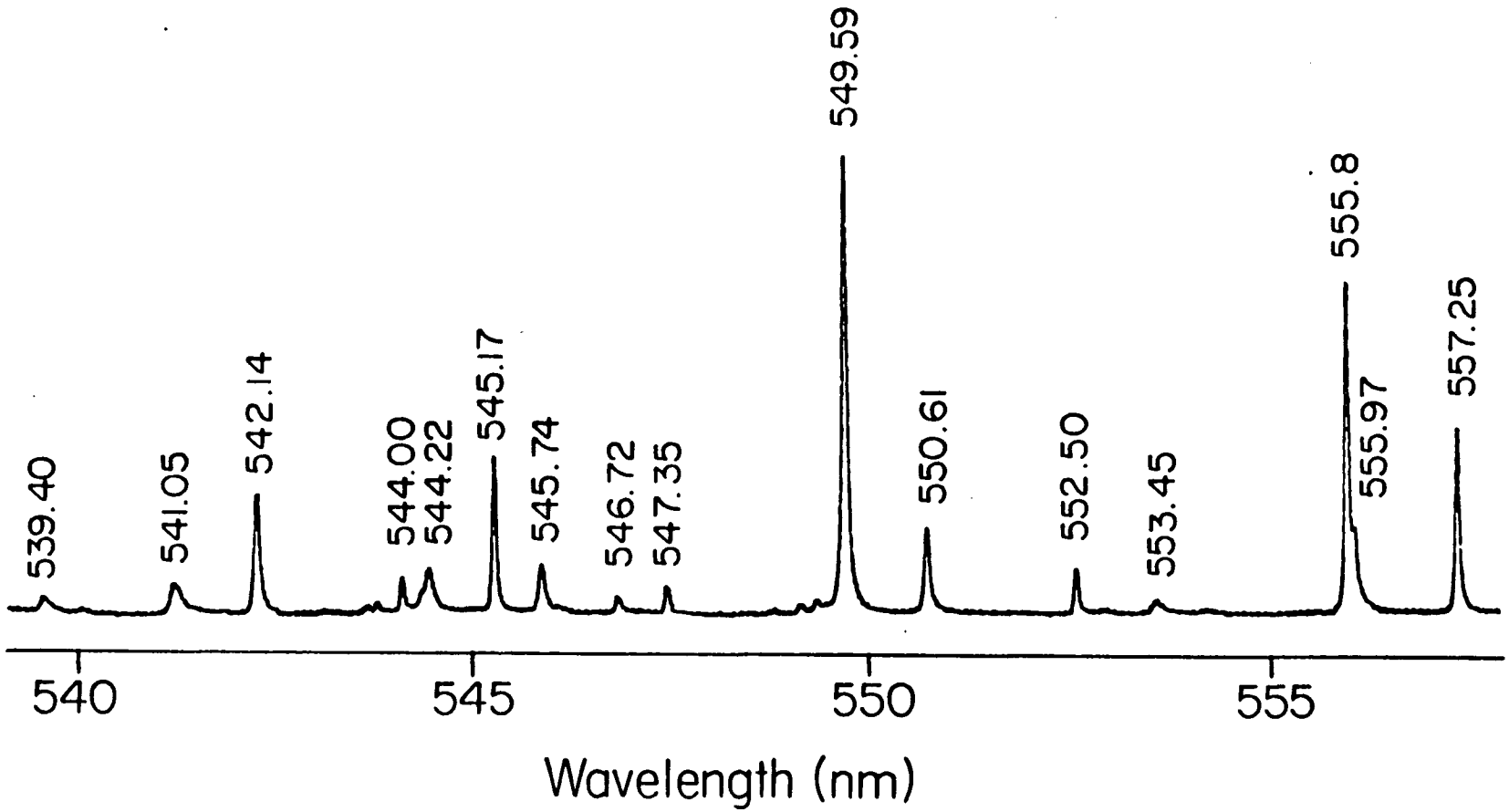

Figure 28 Argon emission spectrum from 540 to 555 nm, recorded with the 4096 photodiode array.

has a larger electron width parameter but its very low intensity prevented its use.

Stark parameters for the ArI 542.14 nm line and for the 549.59 nm line were taken from references 91 and 92 respectively.

The full half width of the Ar I 542.14 nm and Ar I 549.59 nm lines are plotted as a function of electron density in Figure 29. Data from the H_β line at 486.13 nm is included for comparison. Over the range of electron densities encountered in the ICP the Stark half width of the H_β line varies from 0.1 to 0.8 nm. The Stark half widths of the argon lines range from less than 0.04 nm to 0.3 nm. The smaller half width of Ar I lines for a given electron density means that the measurement of n_e from argon line broadening requires higher resolution and a smaller instrumental line profile than the analogous H_β electron density measurements. At 6000 K, the Doppler half width for H_β is 0.029 nm whereas the Doppler contribution to the broadening of the argon lines is of the order of 0.005 nm and has little effect on the half width. However, the instrumental line broadening half width of 0.035 nm made a significant contribution to the argon experimental half widths. It was necessary to deconvolute the instrumental half width. Its magnitude meant n_e could not be effectively measured from argon at electron densities less than $1.0 \times 10^{15} cm^{-3}$.

If Ar I lines are to be effective for the measurement of electron densities, results determined from Stark broadening of argon lines should be essentially the same as those evaluated from the H_β line. To compare the two methods, electron densities were measured under identical plasma conditions using both H_β

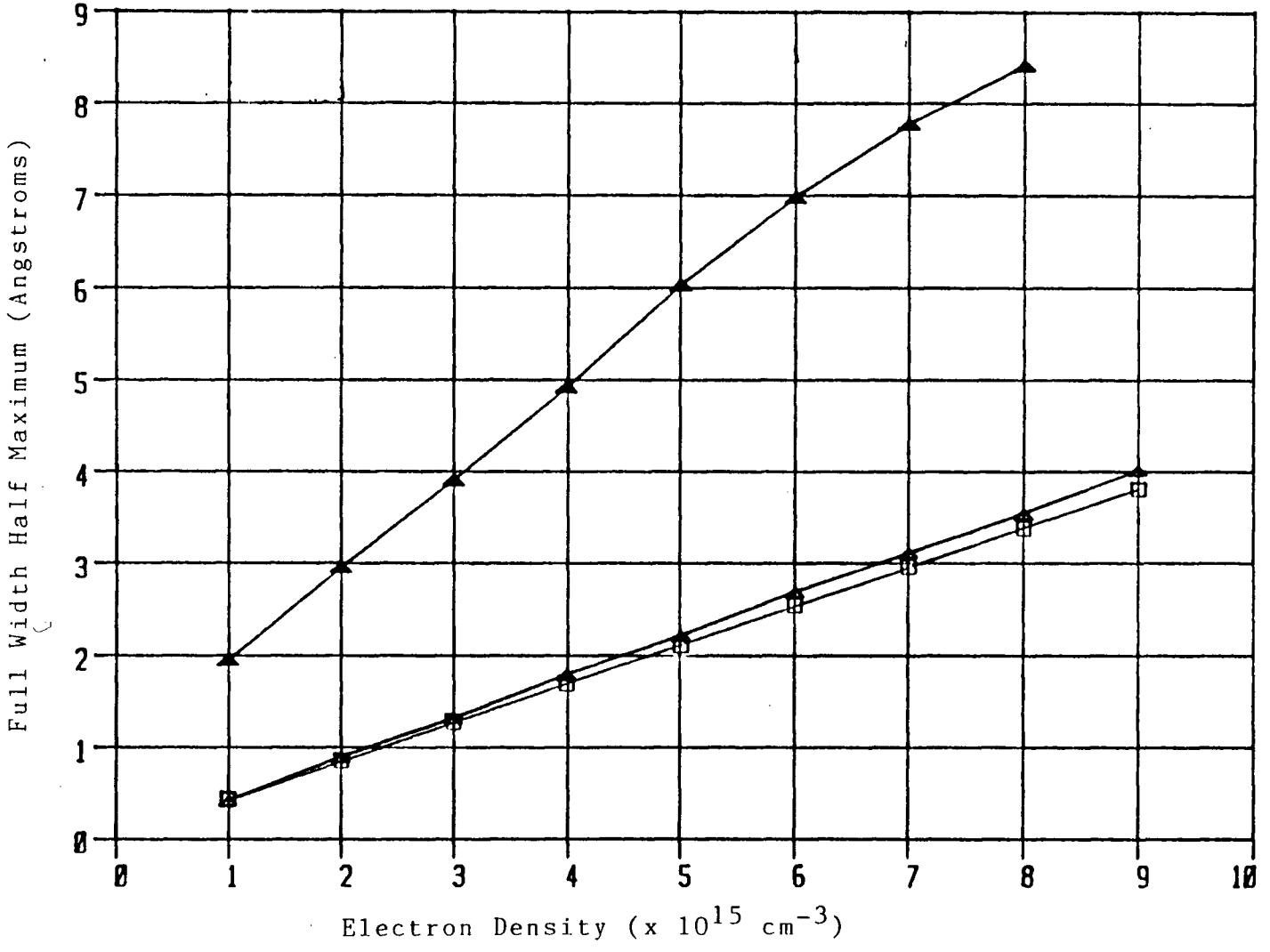

Figure 29 Calculated half-width as a function of electron density for a temperature of 6000 K : H_β 486.13 nm (▲-▲), Ar I 542.14 nm (△-△) and Ar I 549.59 nm (□-□).

broadening and argon line broadening. In Figure 30 the results for two sets of conditions are plotted. Curve a represents radially resolved n_e from H_β at 4 mm above the load coil at an rf input power of 1.75 kW. Curves b and c are radially resolved electron densities from Ar I 542.14 nm and Ar I 549.59 nm respectively, under the same conditions. Curve d is n_e from H_β at 16 mm above the load coil and an rf input power of 1.25 kW. Curves e and f are n_e values from Ar I 542.14 nm and Ar I 549.59 nm lines at the same height and power. This data indicates very good agreement between the two methods of measuring n_e. Electron density profiles from H_β were smoother than those from argon lines due to the much larger half width of the H_β line at a given electron density. However, even at electron densities as low as 1.0 to 1.5 X $10^{15} cm^{-3}$ where the argon half widths were of the order of 0.05 nm argon line broadening gave essentially the same result as H_β. It was not possible to use argon lines to evaluate n_e in the central channel at low heights above the load coil. The combination of low electron density, low argon emission intensity and errors in the Abel inversion caused a lack of precision in the values of n_e. No substantial differences exist between electron densities determined from the two different argon lines.

As a further check on agreement between the two methods, radially resolved electron density was evaluated from Stark broadening of the argon lines at vertical heights of 4, 8, 12, 16 and 20 mm above the load coil for rf powers of 1.25 kW and 1.75 kW. Argon lines were used to measure n_e at these same heights and powers. At each spatial position and power the electron

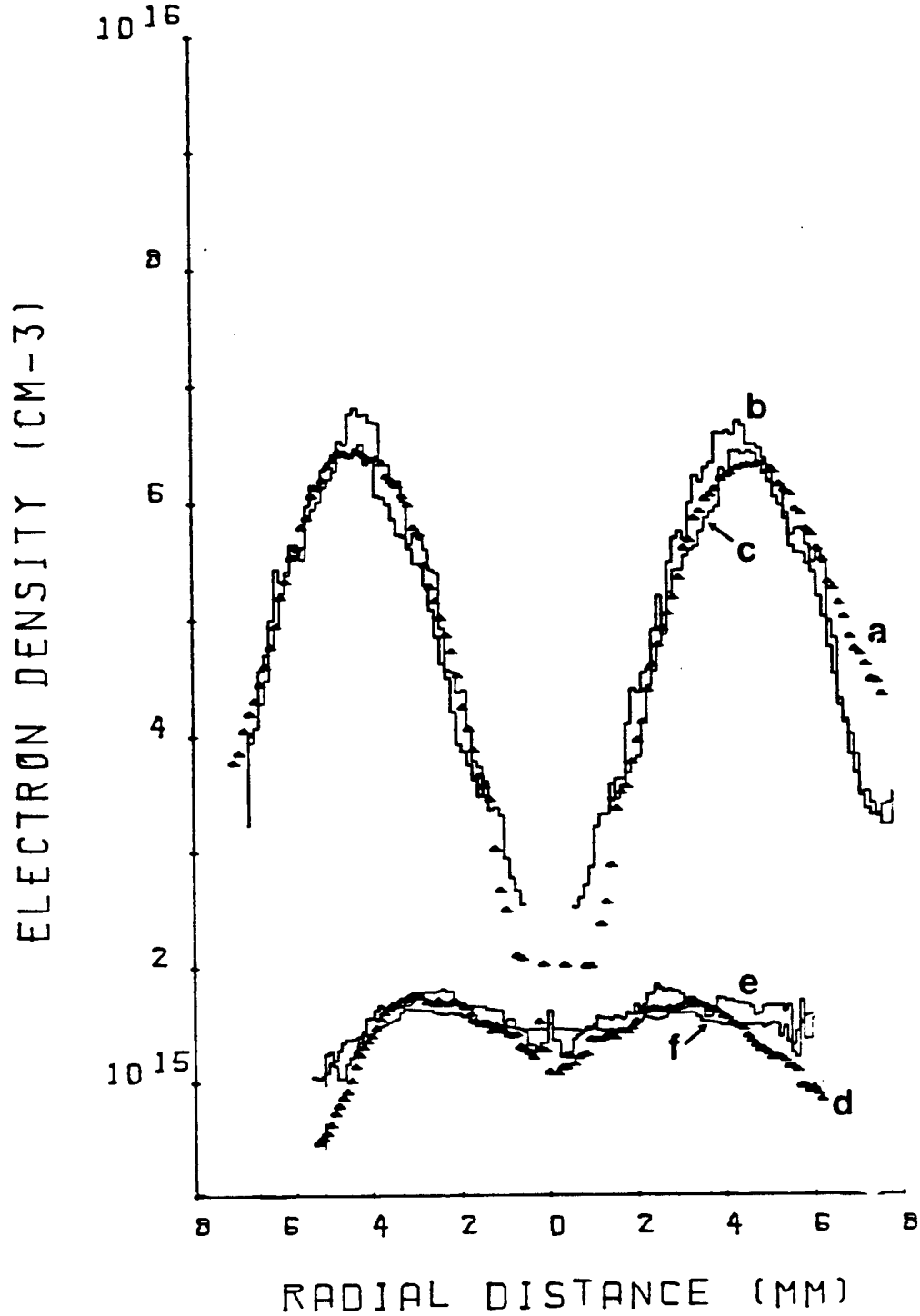

Figure 30 Spatially resolved electron density plot. Curves a-c for 4 mm above the load coil, rf input power 1.75 kW. Curve a - Hβ 486.13 nm, curve b - Ar I 542.12 nm and curve c - Ar I 549.59 nm. Curves d-f for 16 mm above the load coil, rf input power 1.25 kW. Curve d - Hβ 486.13 nm, curve e - Ar I 542.14 nm and curve f - Ar I 549.59 nm.

densities from argon 542.14 nm and 549.59 nm lines were averaged. The average electron densities were combined to produce the isocontour plots in Figure 31. Figure 31(i) is for an input power of 1.25 kW and figure 31(ii) for an input power of 1.75 kW.

These results can be compared to electron densities measured under identical conditions using H_β. Figure 11 and Figure 12(iii) are the corresponding figures for n_e from H_β for the input powers of 1.25 kW and 1.75 kW respectively. For a given input power the pairs of contour plots are virtually identical indicating excellent agreement between the two methods of determining n_e. In addition, the electron density distribution and magnitude are similar to measurements previously published [35,87,88,96,75,76].

The excellent agreement obtained in the spatial distribution of electron density between H_β and argon indicates argon line broadening can be used to give an accurate picture of electron density when no water vapor is present in the ICP.

6.4.2 ELECTRON DENSITY WITH NO WATER VAPOR IN THE AEROSOL GAS

Under the identical conditions used for the previous section, argon lines were used to measure the spatial distribution of electron density with no water vapor present in the aerosol channel. The spray chamber was dried and the sample uptake tube pinched off while all gas flows remained the same. Radially resolved electron densities were measured at vertical heights of 4, 8, 12, 16 and 20 mm above the load coil for rf input powers of 1.25 kW and 1.75 kW. For each power setting, iso-contour plots of electron density were produced from the

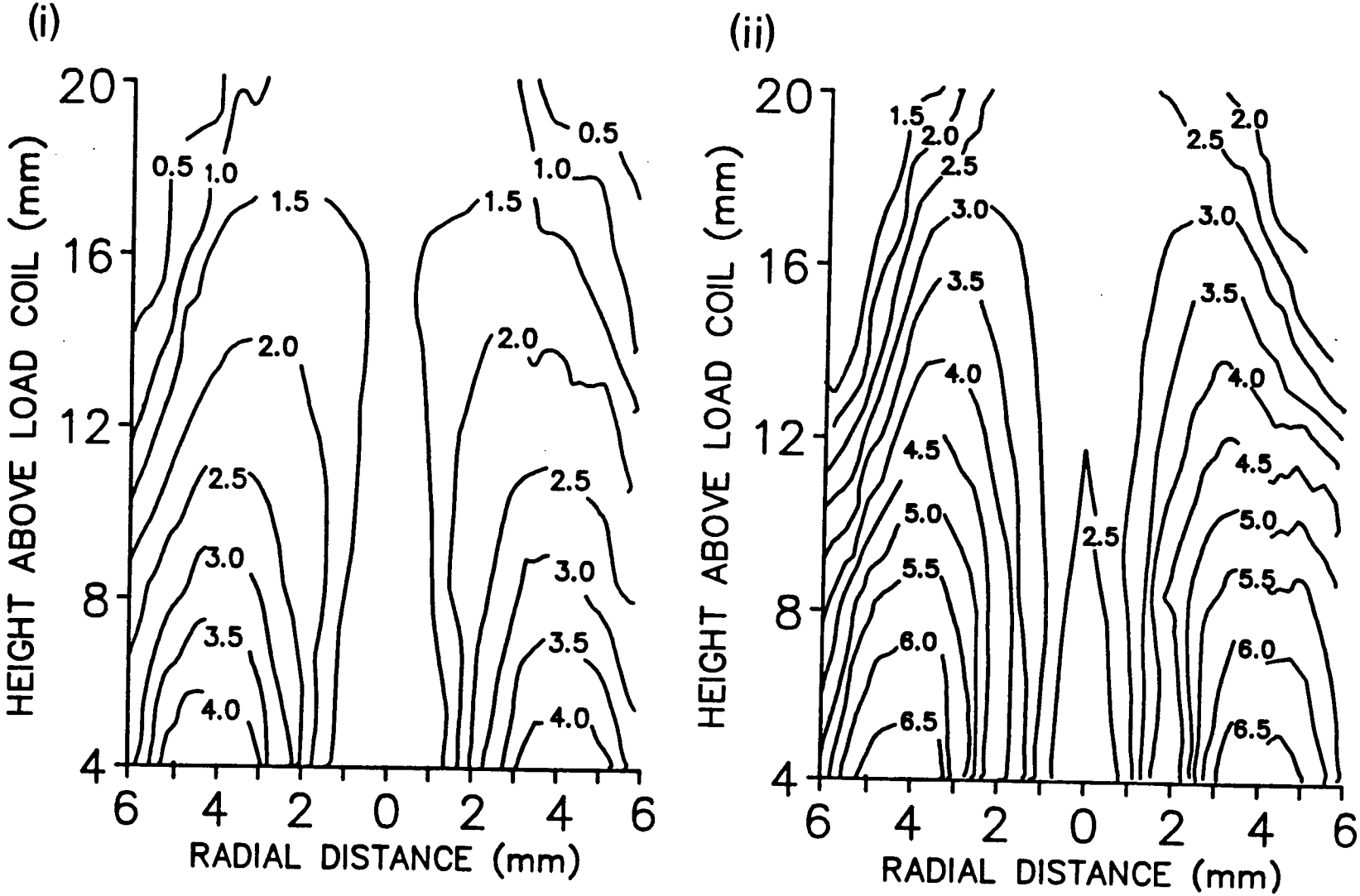

Figure 31 Electron density distribution in the ICP determined from Stark broadening of Ar I with water vapor in the aerosol gas. Rf input power (i) 1.25 kW and (ii) 1.75 kW. Electron number density in units of x $10^{15} cm^{-3}$.

average electron density obtained from the two argon lines. Figure 32(i) is n_e at 1.25 kW input power and 32(ii) n_e is at 1.75 kW input power.

A comparison of these figures with Figure 31 (n_e from argon line broadening with water vapor present) shows the effect of water on electron density distribution in the ICP. In general, the spatial distribution of electron density remained the same; the regions of high and low electron density were in essentially the same spatial positions for both cases. The maximum electron concentration occurred 4 mm above the load coil in the annular region of the discharge and dropped with increasing distance away from the load coil. The central channel was a region of lower electron density. The difference between wet and dry aerosol gas flow into the plasma was that there was an overall decrease in electron density when no water vapor was present. The greatest change in n_e was observed at 4 mm above the load coil in the annular region. At 1.25 kW, the electron density changed from $4.5 \times 10^{15} cm^{-3}$ to $3.8 \times 10^{15} cm^{-3}$ when water vapor was removed. At 1.75 kW there was a decrease from $6.8 \times 10^{15} cm^{-3}$ to $5.8 \times 10^{15} cm^{-3}$ when water vapor was removed. With increasing height above the load coil the differences in n_e with and without water became less significant. At 16 mm above the load coil the change in electron density was of the order of $0.2 \times 10^{15} cm^{-3}$ for 1.25 kW and $0.5 \times 10^{15} cm^{-3}$ for rf power of 1.75 kW. These small differences are below the precision of the measurement from argon line broadening, however there does appear to be a trend to lower electron densities in this region when water vapor is absent. Differences in electron density between wet and dry aerosol flow

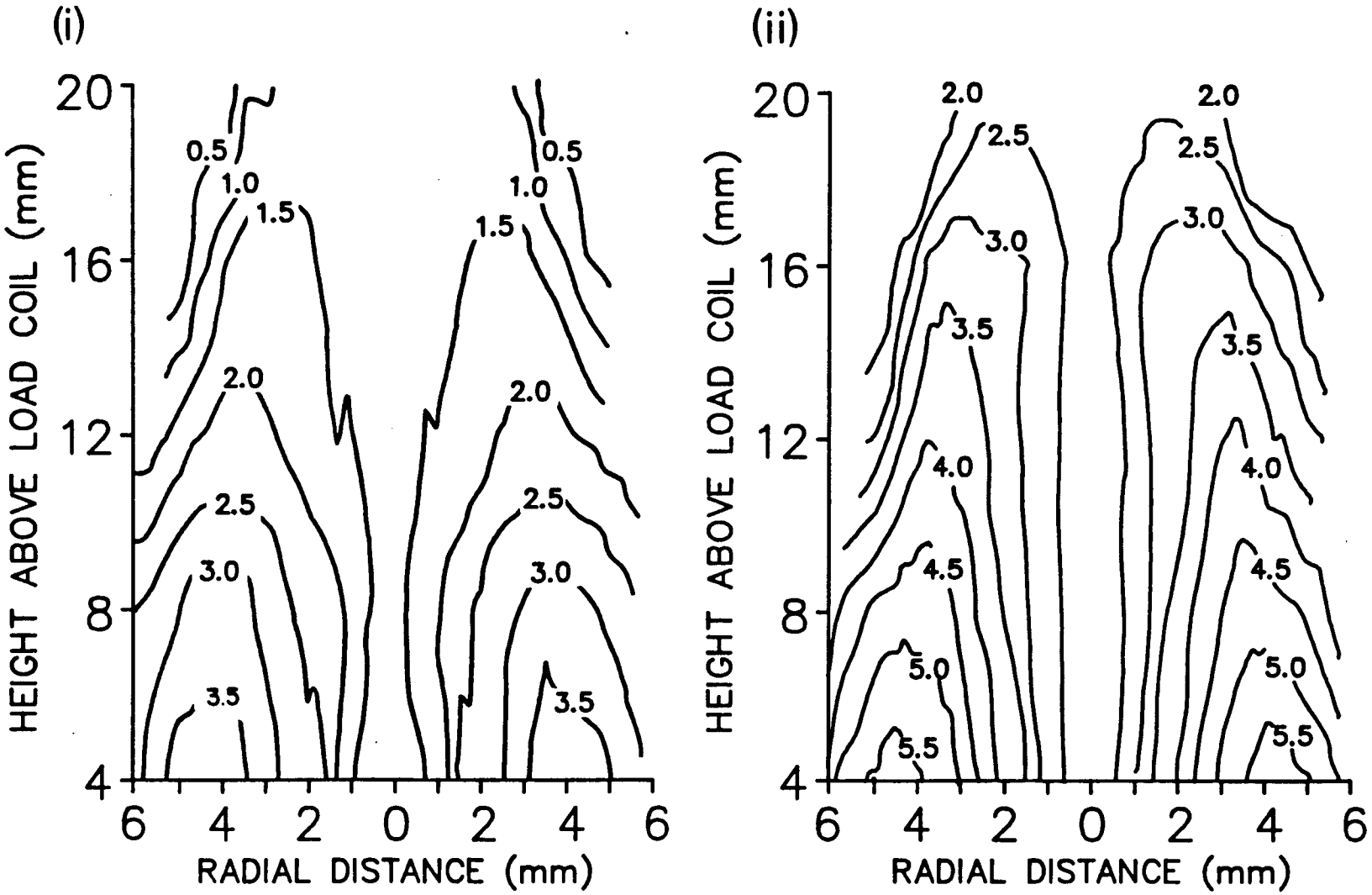

Figure 32 Electron density distribution in the ICP determined from Stark broadening of Ar I without water vapor in the aerosol gas. Rf input powers of (i) 1.25 kW and (ii) 1.75 kW. Electron number density in units of x 10^{15} cm^{-3}.

for the central channel (± 2 mm from the central axis) below 12 mm above the load coil could not be evaluated because of the difficulties mentioned previously in the measurement of argon line broadening in this region.

Alder et al. [53] and Long et al. [151] both report a decrease in electron density of about 0.4 X $10^{15} cm^{-3}$ when water vapor is removed from the plasma. The small changes in n_e observed at 10 mm above the load coil and greater agreed with their observations. The ionization of hydrogen from the decomposition of water is a possible source of electrons and is likely responsible for this small contribution to the electron density.

The much larger changes in n_e observed off axis at low heights above the load coil have not previously been reported. This is not a region where changes in water vapor loading of the aerosol gas would be expected to produce changes in electron density. It is unlikely that there is significant migration of solvent from the aerosol stream into this region of the plasma. Also, the magnitude of the decrease in electron density means the difference probably does not come from the ionization of hydrogen. Calculations of the amount of hydrogen, from water, present in the plasma and the likely degree of ionization of this hydrogen imply ionization of hydrogen was not solely responsible for this difference.

Observation of the plasma gave a clue to the possible source of this difference. When water was excluded from the aerosol channel, the plasma appears to move down so the bottom of the discharge was closer to the top of the torch. Turning down the

auxiliary gas flow achieves a similar effect. Water undergoes a substantial increase in molar volume with the transition from liquid to gas phase. This volume increase acts to lift the plasma off the top of the sample and intermediate torch tubes, thus the volume of plasma between the top of the torch and the load coil is reduced. The difference between electron density with and without water may be attributed to this. The same number of electrons are created whether water is present or not, but when water is present they occupy a smaller volume and thus there is a higher electron density. This volume expansion could also be responsible for the somewhat narrower aerosol channel observed when water vapor is not present in the plasma.

The changes in excitation conditions experienced by an analyte under dry aerosol sample introduction conditions are not immediately obvious from this data. At first glance, the electron density in the normal analytical zone (12-16 mm above the load coil) is essentially the same under both conditions so excitation conditions should remain very similar. Thus, one would expect the same degree of ionization of analyte and similar relative populations of the energy levels within an ionization stage for either wet or dry aerosol sample introduction. However, the effect of the larger change in n_e experienced in the annular region of the plasma is not currently well understood. Changes in electron density in this region could affect excitation conditionsthroughout the plasma. Complete spatial maps of excitation temperature and ion/atom ratios should clarify this.

These results imply the ionization of the dissociation

products of water need not be considered when calculating $T_{e,LTE}$. In the normal analytical zone the difference between wet and dry aerosol is less than the error in the measurement. The larger differences observed low in the annular region of the plasma seem to be the consequence of physical effects rather than the ionization of hydrogen and water.

6.4.3 ELECTRON DENSITIES WITH NO AEROSOL GAS FLOW

The Stark broadening of argon lines was used to measure electron density with no aerosol gas flow into the plasma. The plasma and auxiliary gas flow rates were maintained at the same values as in the previous section and the aerosol gas turned off. Radially resolved electron number density profiles were measured at vertical heights of 4, 8, 12, 16 and 20 mm above the load coil for rf input powers of 1.25 kW and 1.75 kW. The electron densities from the argon 542.14 nm and 549.59 nm lines were averaged and contour plots of electron density distribution produced. Figure 33(i) is n_e at 1.25 kW and 33(ii) is n_e at 1.75 kW.

Dramatic changes in electron number density and its spatial distribution occurred when aerosol gas was not present. The central channel was no longer a region of low electron density. Electron density decreased with both height above the load coil and distance from the plasma center. The maximum electron density was found at 4 mm above the load coil, at a distance of 1 to 2 mm from the plasma center. With an aerosol gas flow present the maximum was at this height but 3 to 5 mm from the plasma center.

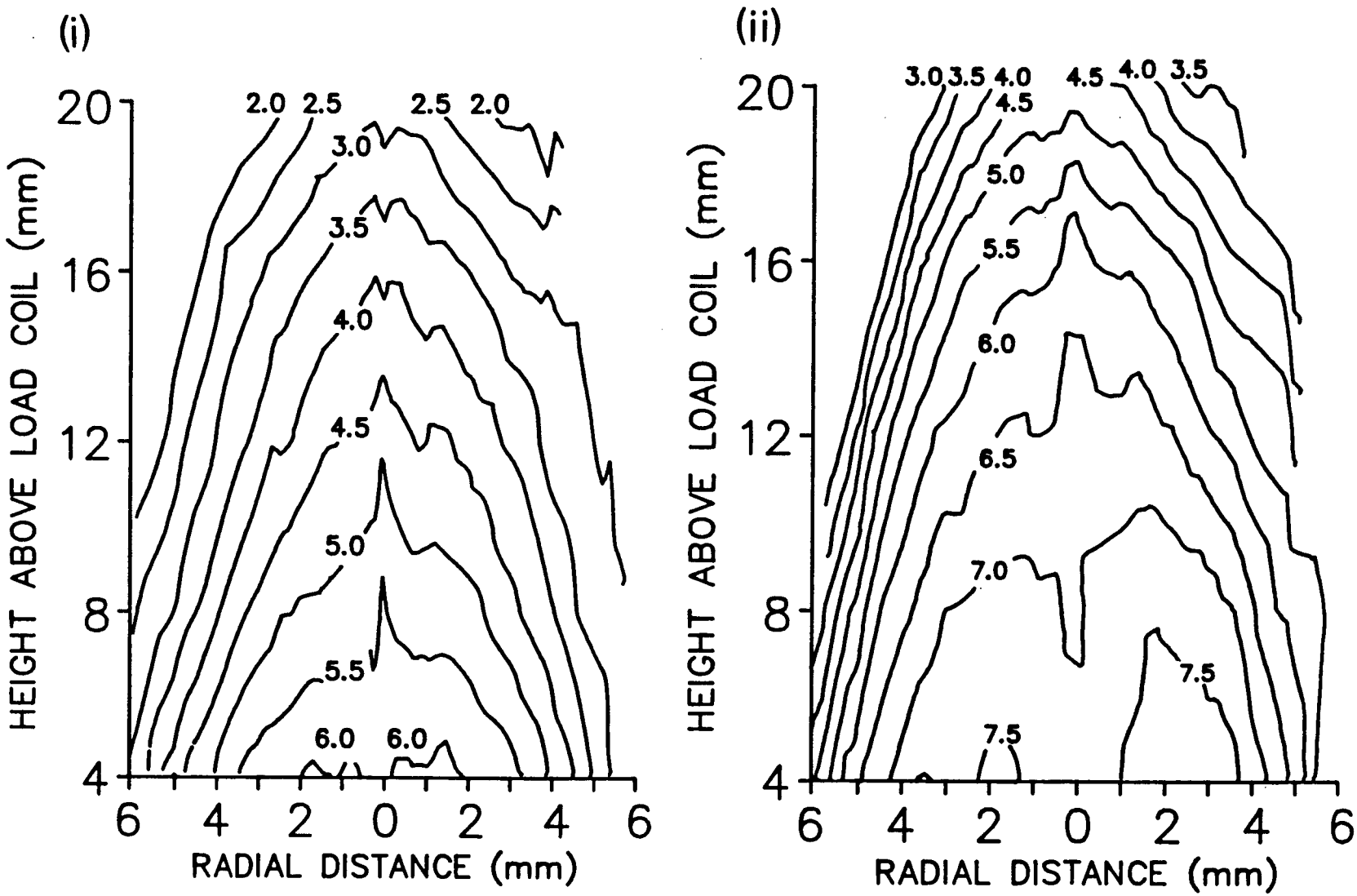

Figure 33 Electron density distribution in the ICP determined from Stark broadening of Ar I with no aerosol gas flow. Rf input powers of (i) 1.25 kW and (ii) 1.75 kW. Electron number density in units of x 10^{15} cm^{-3}.

There was a significant increase in n_e without any aerosol gas. At 1.25 kW input power the maximum n_e observed was $6.0 \times 10^{15} cm^{-3}$ compared to $4.0 \times 10^{15} cm^{-3}$ with an aerosol gas flow. For 1.75 kW the maximum without aerosol gas was $7.5 \times 10^{15} cm^{-3}$, an increase of $1.0 \times 10^{15} cm^{-3}$. In addition to the increases in the maximum electron density observed, most spatial regions of the plasma exhibited higher electron density. The entire spatial region from about 4 mm on either side of the plasma center up to 14 mm above the load coil had electron densities that exceeded the maximum observed with aerosol gas.

Figure 33(i) is an interesting companion to Figures 13(i), 13(ii) and 13(iii) in which electron density contour plots are presented as a function of aerosol flow rate at an rf power of 1.25 kW. It was found that as aerosol flow rate was decreased the area of maximum n_e moved closer to the central channel of the plasma and electron density increased. These results are in agreement with those of Mermet [85]. Variations in aerosol flow rate substantially affect the electron density in the central channel but have little influence on n_e in other spatial regions of the plasma. Mermet observes a difference of $8.0 \times 10^{15} cm^{-3}$ in central channel electron density between aerosol flow rates of 2.5 l m^{-1} and 0.0 l m^{-1}.

The heating of the cold aerosol gas causes a substantial reduction in observed electron density. The overall effect of aerosol flow rate on electron density is much greater than the presence of water vapor.

6.5 SUMMARY

Stark broadening of argon lines provides a useful alternative to the Stark broadening of H_β for the measurement of electron density in the ICP. There is excellent agreement between the results obtained by the two methods. Argon line broadening has the advantage that it can be employed in situations where measurement of electron density from hydrogen is not possible. This is the case when water vapor is eliminated from the aerosol gas flow.

The elimination of water from the aerosol flow decreases the overall electron density. At 16 mm above the load coil the changes are small. However, at heights low in the plasma decreases of the order of $1.0 \times 10^{15} cm^{-3}$ in electron density were observed. The results indicate the ionization of the dissociation products of water need not be considered when calculating $T_{e,LTE}$.

Chapter 7

CONCLUSIONS

In the introduction to this thesis the object of an excitation model for the ICP was described as characterization of level populations for analyte species and identification of the plasma processes important in establishing this distribution. The experimental observations presented in this work and the interpretation put forth provide the basis for such a model. When electron density is used to evaluate an LTE temperature and construct a theoretical LTE framework a new understanding of the ICP is gained.

Spatially resolved electron densities were measured under a variety of plasma operating conditions. Measured electron density and the plasma pressure were used to evaluate an LTE temperature and expected LTE values of other parameters. Experimental ion-atom emission intensities were within an order of magnitude of LTE ratios and in general the experimental values were less than the LTE values. Experimental degrees of ionization were also less than calculated LTE values. Deviations from LTE decreased as electron density increased and, for a series of elements, increased with the excitation energy and ionization potential.

These observations of experimental ion-atom ratios less than LTE values and underionized analyte are contrary to previous findings and result solely from the temperature used in the LTE calculations. The observed underexcitation and underionization is attributed to overpopulation of atom levels relative to ground state ion level populations. The atom levels are

overpopulated due to the dominance of radiative depopulating processes over collisional depopulating processes. Since the ICP is an optically thin plasma, collisional de-excitation must be much more frequent than radiative decay for LTE to be established and maintained.

In a publication reviewing plasma excitation mechanisms De Galan has stated that the validity of an excitation model for the ICP is determined by its ability to explain three observations [17]. These observations are

"(1) The observed concentrations of electrons, and hence of argon ions ranging from $10^{14}cm^{-3}$ to $10^{16}cm^{-3}$ cannot be reconciled with spectroscopically measured excitation temperatures using the two-line or many-line technique.

(2) The values found for such excitation temperatures increase with the upper energy of the transitions considered or, in other words, the relative overpopulations of an energy level increases with its excitation energy.

(3) The intensity ratio of an ion line and an atom line of the same element is again significantly higher than expected from LTE expressions using excitation temperatures."

The ideas presented in this thesis have led to a new understanding of the ICP level populations and the processes controlling them. This particular conception of the plasma allows the interpretation of all these spectroscopic observations within one self-consistent model.

With regard to the first point, the electron density, argon

ion number density and analyte ion density values are all consistent equilibrium values for an argon plasma at 1 atm. The atom levels are not in equilibrium and are overpopulated relative to the ion densities due to radiative processes. Attempts to use the Boltzmann distribution to derive a temperature, T_{exc}, from the atom levels will result in a temperature less than the temperature describing the ionization equilibrium because the neutral atom levels are overpopulated. Excitation temperatures and electron concentrations can be reconciled if the atom levels are considered to be overpopulated relative to the grounds state ion level population.

The second observation is also explained by overpopulation of atom levels. The change in excitation temperatures with energy level is a result of the differences in overpopulation factors for the various levels. Overpopulation of levels is a consequence of radiative decay rates being comparable or even larger than collisional de-excitation rates. Since spontaneous transition probabilities decrease with increasing principal quantum number, whereas the collisional rates increase, the overpopulation of levels thus decreases with increasing energy levels. Temperature measured from the lower energy levels will be the lowest because these levels are the most overpopulated. Higher energy levels will be less overpopulated and excitation temperatures from these levels will be greater. Levels close to the ionization limit will have populations close to LTE values and temperature measurements on these levels will result in the highest excitation temperature.

Whether it is the upper or lower levels that are

overpopulated is actually just a matter of viewpoint. One approach considers the higher energy atom levels to be overpopulated relative to the ground state atom population and an excitation temperature measured from low energy levels. This viewpoint requires a process to overpopulate the upper energy atom levels, ion levels and produce a suprathermal electron density. To date, researchers have not been successful in identifying such a process in the ICP. The viewpoint taken here considers the low energy atom levels to be overpopulated with respect to the upper energy atom levels and the ion ground state. It has the advantage of conceptualizing the plasma in terms of a p-LTE scheme for the upper energy levels with lower energy levels overpopulated due to radiative decay and radiative recombination rates not being exceeded by collisional de-excitation rates.

Point three, the question of ion-atom emission intensity ratios, was the subject of Chapter 4. If measured electron density and a temperature derived from electron density are used to calculate LTE values the result is LTE ion-atom intensity ratios that are very close to experimental values. In general experimental ion-atom emission intensity ratios are less than LTE expressions predict. The ratios are less because atom levels are overpopulated.

These analyte level populations can be understood in terms of a partial LTE model. The electron density, ground state ion and upper atomic energy levels are in Saha equilibrium. Lower atomic energy levels are overpopulated with respect to this equilibrium due to radiative processes. Collisional de-excitation is balanced by collisional excitation but spontaneous

radiative decay and radiative recombination are not balanced by absorption processes. For low lying atomic levels where radiative processes make significant contributions to the total depopulation rates this improper balance causes deviations from LTE populations. The atom ground state is the most overpopulated level and overpopulation decreases with increasing energy of the level until p-LTE is reached for the upper atomic levels.

One of the causes of p-LTE is a two temperature plasma. Collisions between electrons and heavy particles are not very efficient at transferring energy due to the large mass difference and so the two types of particles do not achieve the same kinetic temperature. The electrons have one Maxwellian distribution and the heavy particles have another lower temperature Maxwellian distribution. Measurements in the ICP indicate the electron temperature and gas temperature differ by at least 1500 K and up to 5000 K [35,66]. For levels near the ionization limit where energy differences between levels are small, the electrons, ion ground state and atomic levels achieve Saha equilibrium. The upper atomic levels are distributed according to the electron temperature. For lower atomic levels, where energy differences become greater and the rates of radiative processes increase, Saha equilibrium between the atomic level, the ion ground state, and free electrons cannot be maintained. These levels have a temperature somewhere between the electron temperature and the gas temperature.

The level at which Saha equilibrium is achieved and the particular distribution in the lower part of the atomic energy levels depends of the atomic properties of the analyte species as

well as the electron temperature and density. The competition between collisional and radiative depopulation determines the degree of deviation from LTE populations. The collisional rate is dependent on n_e and T_e, properties of the plasma, while the transition probability is an atomic property and is independent of n_e and T_e. An increase in temperature or electron density increases the collision rates and causes the system to move closer to LTE. Transition probabilities and atomic energy level structure vary from element to element resulting in differences in the departures from LTE for each element.

The exact nature of the overpopulation of atom levels is not known at this time. The observed electron density in the ICP is too large for a purely radiatively dominated distribution but not high enough for the plasma to be totally collisionally dominated. At this intermediate electron density the ICP is in the electron saturation balance regime. In the atomic energy level scheme there will be boundaries dividing the energy levels into the three regimes [38,45]. The radiative regime will be applicable for the lowest energy levels, the electron saturation balance for intermediate energy levels and p-LTE for the uppermost energy levels. The particular energy levels which mark the boundaries between these three regimes are not known as of yet.

This model indicates the Boltzmann equilibrium is lost in the ICP but Saha equilibrium is maintained at least for a few high energy levels. The reasons for this can be understood in terms of the difference between the Saha and Boltzmann distributions. Boltzmann equilibrium describes the balance between forward and backward processes between levels. In p-LTE,

it is a relationship between excited states and in LTE a relationship between excited states and the ground state. Saha equilibrium originates from the balance of the processes between a bound level on one side and the ion state and free electrons on the other side. This relates level population with ion ground state and continuum and provides more information than the Boltzmann distribution. If two levels are populated according to the Saha equilibrium their population densities are also related according to Boltzmann distribution. The opposite is not necessarily valid, a Boltzmann distribution does not necessarily mean the Saha equilibrium is also adhered to. The Boltzmann relation cannot be assumed to be valid. In general the Saha equilibrium will not be valid either, especially for low lying levels. However, close to the ionization limit levels exist with such a small energy separations from the ion ground state that ionization and three body recombination occur more frequently than radiative balance disturbing processes. The upper part of the atomic system is in p-LTE and levels are populated according to Saha.

A tremendous difference also exists between the atom ground state and ion ground state. The ground state atom is isolated from the rest of the system by the large energy gap between it and the first excited state. It is relatively easy for it to become decoupled from the rest of the atomic system. On the other hand, the ion state is approached infinitely closely by the upper part of the atomic system and an equilibrium balance is established. Thus the upper part of the system is in equilibrium and deviations from equilibrium manifest themselves in the lower

part of the system. This implies excited state atom populations are connected to the ion ground state rather than the atom ground state. Experimental observations appear to confirm this. Horlick [152] observes a correlation between neutral atom emission behavior and ion density. Hieftje et al. [31] find a correlation between the calcium atom emission and the product of calcium ion ground state and n_e. No correlation exists between atom emission and the product of calcium ground state and n_e.

The data presented here are not conclusive evidence of p-LTE for analyte level populations. However, when the experimental data are considered, in conjunction with available studies of level populations in the ICP and a basic understanding of plasma processes, the interpretation of p-LTE is more than just plausible.

The model developed for plasma excitation explains observed plasma emission characteristics and the values of spectroscopically measured parameters. It also has the ability to predict plasma behavior and aid in the development of the ICP as an analytical tool. The simple application in Chapter 5 has illustrated the utility of the concept in predicting ion behavior in the ICP. The departures from LTE followed a consistent pattern with plasma electron density and analyte ionization energy. Ion-atom emission intensity ratios and degrees of ionization can be predicted with some confidence for other analyte species not studied. Much broader and more ambitious applications can be imagined and are being investigated.

The prediction of spectra under various conditions now seems

a reasonable goal given adequate transition probabilities for each analyte. Prediction of spectra would be valuable in the ICP in order to select the best emission line for analysis and determine which elements will cause spectral interferences. A great deal of effort has been devoted to the tabulation of spectral interference tables and atlases of wavelengths [153-156]. Even the best of these tabulations are limited because they are obtained under one particular set of ICP operating conditions. Changes in ICP input parameters such as gas flow rates, input power, observation height, can drastically alter the relative intensity of emission lines.

Given a model that predicts ICP spectra one can envision a much more general approach to the problem of identifying spectral overlaps. A computer program could be developed that uses atomic data on the elements, instrument resolution and then given a few plasma parameters, such as input power and aerosol flow rate, is able to use the model of analyte behavior to predict total ICP spectra under the exact set of operating conditions and sample composition. Preliminary investigations by Burton and Blades [157] into this approach have met with some success.

A major limitation of the above plan results from the availability of transition probabilities. The data in this area is by no means complete, data for elements with atomic numbers greater than Ca is scarce, and for the other elements many transitions are not listed plus errors of 25% - 50% are not uncommon. Accurate transition probabilities are also necessary for many plasma diagnostic studies such as temperature measurements from emission intensity, rate calculations and the

evaluation of level populations. If the exact nature of the level population distribution in the ICP is understood there exists a possibility to use it to evaluate relative values of transition probabilities. For this purpose the discharge does not have to be in LTE, it is only necessary that the nature of the distribution of level populations be understood. Brault and Faires [158] have already started studies on utilizing a ICP Fourier transform spectrometer system to determine lifetimes of certain molybdenum levels. The level populations vary in a smooth and systematic way so populations for levels with unknown lifetimes are interpolated. The emission intensity of the level, interpolated population and known lifetime of other levels are used to determine transition probabilities. It is somewhat ironic that in Reed's first papers on atmospheric inductively coupled plasmas [1,2] he mentions the possibility of the source being used to determine gA values rather than its analytical potential. Now, twenty years later, because of the development of the ICP as an analytical tool and the extensive study it received as a result of its analytical applications it is being used for this very purpose.

The basics of a p-LTE model for analyte level populations have been put forward but a great deal of work remains to be done to refine it. Level populations for a larger series of elements must be evaluated to determine how universally valid the model is. Ground state atom and ion populations also need to be determined, these are pivotal populations for the model and in this work were only estimated from the emission intensity of the first excited state. The exact nature of the atomic level

population distribution needs to be determined and correlated with atomic properties. Initial results suggest the atomic levels are divided into three balance regimes - radiative, electron saturation and p-LTE. The energy levels that divide the atomic levels into the three regions and the manner in which they vary with electron density must be identified. A combination of experimental results and theoretical calculations should accomplish this.

The objectives of this thesis have been accomplished. An excitation model for the ICP describing analyte level populations and the processes responsible for this distribution has been proposed and supported by experimental evidence.

This thesis contributes significantly to the ICP literature in two respects:

1) Comprehensive, detailed spatial maps of electron density under a variety of plasma conditions have been presented.

2) A consistent model for rationalizing and predicting analyte emission behavior in the inductively coupled plasma has been described.

LIST OF REFERENCES

1 T.B.Reed, J. Appl. Phys. 32, 821 (1961).

2 T.B.Reed, J. Appl. Phys. 34, 2266 (1963).

3 S.Greenfield, I.L.Jones and C.T.Berry, Analyst 89, 713 (1964).

4 R.H.Wendt and V.A.Fassel, Anal. Chem. 37, 920 (1965).

5 G.Dickinson and V.A.Fassel, Anal. Chem. 41, 1021 (1969).

6 P.W.J.M.Boumans and F.J.deBoer, Spectrochim. Acta 27B, 391 (1973).

7 V.A.Fassel and R.N.Kniseley, Anal. Chem. 46, 1110A (1974).

8 V.A.Fassel and R.N.Kniseley, Anal. Chem. 46, 1155A (1974).

9 S.Greenfield, H.McD.McGeachin and P.B.Smith, Talanta 23, 1 (1976).

10 R.M.Barnes, Trends in Anal.Chem. 1, 51 (1981).

11 V.A.Fassel, Spectrochim. Acta 40B, 1281 (1985).

12 A.Montaser and V.A.Fassel, Anal. Chem. 48, 1490 (1976).

13 R.S.Houk, V.A.Fassel, G.D.Flesch, H.J.Svec, A.L.Gray and C.E.Taylor, Anal. Chem. 52, 2283 (1980).

14 R.Koirtyohann, J.S.Jones and D.A.Yates, Anal. Chem. 52, 1965 (1980).

15 R.M.Barnes, CRC Critical Rev. in Chem.,Sept., 203 (1978).

16 M.J.Thompson and J.N.Walsh, "A Handbook of ICP Spectrometry." Chapman and Hall, New York (1983).

17 L.deGalan, Spectrochim. Acta 39B, 537 (1984).

18 P.A.M.Ripson and L.deGalan, Spectrochim. Acta 38B, 707 (1983).

19 J.Mostaghimi, P.Proulx, M.I.Boulos, and R.M.Barnes, Spectrochim. Acta 40B, 153 (1985).

20 J.B.Hasted, "Physics of Atomic Collisions," 2nd ed. American Elsevier Publishing Co., New York (1972).

21 D.R.Bates, ed., "Atomic and Molecular Processes." Academic Press, New York (1962).

22 R.C.Elton, Atomic,Processes. In "Methods of Experimental Physics - Plasma Physics" (H.R.Griem and R.H.Lovberg, eds.), Vol 9A, p.115. Academic Press, New York (1972).

23 D.C.Schram, I.J.M.M.Raaymakers, B. van der Sijde, H.J.Schenkelaars and P.W.J.M.Boumans, Spectrochim. Acta 38B, 1545 (1983).

24 A.Goldwasser, and J.M.Mermet, Spectrochim. Acta 41B, 00 (1986).

25 H.Uchida, K.Tanabe, Y.Nojiri, H.Haraguchi and K.Fuwa, Spectrochim. Acta 36B, 711 (1981).

26 T.Hasegawa, K.Fuwa and H.Haraguchi, Chemistry Letters, 2027 (1984).

27 P.W.J.M.Boumans, Spectrochim. Acta 37B, 75 (1982).

28 P.W.J.M.Boumans and F.J.deBoer, Spectrochim. Acta 32B, 365 (1977).

29 J.W.Mills and G.M.Hieftje, Spectrochim. Acta 39B, 859 (1984).

30 M.W.Blades and G.M.Hieftje, Spectrochim. Acta 37B, 191 (1982).

31 G.M.Hieftje, G.D.Rayson and J.W.Olesik, Spectrochim. Acta 40B, 167 (1985).

32 D.R.Bates, A.E.Kingston and R.W.P.McWhirter, Proc.Roy.Soc. A257, 297 (1962).

33 D.R.Bates, A.E.Kingston and R.W.P.McWhirter, Proc.Roy.Soc. A270, 155 (1962).

34 R.W.P.McWhirter, Spectral Intensities. In "Plasma Diagnostic Techniques" (R.H.Huddlestone and S.L.Leonard, eds.), p.201. Academic Press, New York (1965).

35 T.Hasegawa and H.Haraguchi, Spectrochim. Acta 40B, 1505 (1985).

36 R.J.Lovett, Spectrochim. Acta 37B, 969 (1982).

37 P.W.J.M.Boumans, "Theory of Spectrochemical Excitation." Hilger and Watts, London (1966).

38 J.J.A.M. van der Mullen, Ph.D. thesis Eindhoven University of Technology, (1986).

39 H.R.Griem, Phys. Rev. 131, 1170 (1963).

40 H.W.Drawin, High Pressures-High Temperatures,2, 359 (1970).

41 M.J.Seaton, Month. Not. Roy. Astr. S 119, 90 (1959).

42 T.Fujimoto, J. Phys. Soc. Jpn. 47, 265 (1979).

43 T.Fujimoto, J. Phys. Soc. Jpn. 47, 273 (1979).

44 T.Fujimoto, J. Phys. Soc. Jpn. 49, 1561 (1980).

45 T.Fujimoto, J. Phys. Soc. Jpn. 49, 1569 (1980).

46 K.Tachibana and K.Fukuda, Japan. J. Appl. Phys. 12, 895 (1973).

47 J.J.A.M. van der Mullen, B. van der Sijde and D.C.Schram, Phys. Letters 79A, 51 (1980).

48 I.Reif, V.A.Fassel and R.N.Kniseley, Spectrochim. Acta 28B, 105 (1973).

49 I.Reif, V.A.Fassel and R.N.Kniseley, Spectrochim. Acta 31B, 377 (1976).

50 R.Mavreodineanu and H.Boiteux, "Flame Spectroscopy." John Wiley and Sons, New York (1965).

51 R.W.Porter and T.P.Anderson, J.Q.S.R.T. 3, 279 (1963).

52 G.R.Kornblum and L.deGalan, Spectrochim. Acta 32B, 71 (1977).

53 J.F.Alder, R.M.Bombelka and G.F.Kirkbright, Spectrochim. Acta 35B, 163 (1980).

54 D.J.Kalnicky, R.N.Kniseley and V.A.Fassel, Spectrochim. Acta 30B, 511 (1975).

55 J.Jarosz, J.M.Mermet and J.P.Robin, Spectrochim. Acta 33B, 55 (1978).

56 M.H.Abdallah and J.M.Mermet, Spectrochim. Acta 37B, 391 (1982).

57 A.Batal, J.Jarosz and J.M.Mermet, Spectrochim. Acta 36B, 983 (1981), 37B, 511 (1982).

58 M.W.Blades and B.L.Caughlin, Spectrochim. Acta 40B, 579 (1985).

59 L.M.Faires, B.A.Palmer, R.Engleman Jr and T.M.Niemczyk, Spectrochim. Acta 39B, 819 (1984).

60 L.M.Faires, B.A.Palmer and J.W.Brault, Spectrochim. Acta 40B, 135 (1985).

61 N.Furuta, Spectrochim. Acta 40B, 1013 (1985).

62 N.Furuta and G.Horlick, Spectrochim. Acta 37B, 53 (1982).

63 W.H.Gunter, K.Visser and P.B.Zeeman, Spectrochim. Acta 38B, 949 (1983).

64 T.Hasegawa and H.Haraguchi, Spectrochim. Acta 40B, 123 (1985).

65 M.Huang, K.A.Marshall and G.M.Hieftje, Anal. Chem. 58, 207 (1986).

66 H.G.C.Human and R.H.Scott, Spectrochim. Acta 31B, 459 (1976).

67 D.J.Kalnicky, V.A.Fassel and R.N.Kniseley, Appl. Spectrosc. 31, 137 (1977).

68 H.Kawaguchi, T.Ito and A.Mizuike, Spectrochim. Acta 36B, 615 (1981).

69 G.R.Kornblum and L.deGalan, Spectrochim. Acta 29B, 249 (1974).

70 Y.Nojiri, K.Tanabe, H.Uchida, H.Haraguchi, H.Fuwa and J.D.Winefordner, Spectrochim. Acta 38B, 61 (1983).

71 G.R.Kornblum and J.Smeyers-Verbeke, Spectrochim. Acta 37B, 83 (1982).

72 Z.Walker and M.W.Blades, Spectrochim. Acta 41B, 000 (1986).

73 I.J.M.M.Raaijmakers, P.W.J.M.Boumans, B. van der Sijde and D.C.Schram, Spectrochim. Acta 38B, 697 (1983).

74 M.W.Blades, Appl. Spectrosc. 37, 371 (1983).

75 B.L.Caughlin and M.W.Blades, Spectrochim. Acta 39B, 1583 (1984).

76 B.L.Caughlin and M.W.Blades, Spectrochim. Acta 40B, 1539 (1985).

77 John Hillborm, ed. "Science and Engineering Programs, AppleII Edition." Osborne/McGraw Hill, Berkeley (1981).

78 A.Savitzky and M.J.E.Golay, Anal. Chem 36, 1627 (1964).

79 O.H.Nestor and H.N.Olsen, SIAM Rev. 2, 200 (1960).

80 C.J.Cremers and R.C.Birkebak, Applied Optics 5, 1057 (1966).

81 J.D.Algeo and M.B.Denton, Appl. Spectrosc. 35, 35 (1981).

82 S.L.Simons,Jr., Byte Magazine (Nov.) 487 (1983).

83 A.Montaser, V.A.Fassel and G.Larsen, Appl. Spectrocs. 35, 385 (1981).

84 A.Montaser, and V.A.Fassel, Appl. Spectrosc. 36, 613 (1982).

85 J.M.Mermet, Spectrochim. Acta 30B, 383 (1975).

86 N.Furuta, Y.Nojiri and K.Fuwa, Spectrochim. Acta 40B, 423 (1985).

87 E.H.Choot and G.Horlick, Spectrochim. Acta 41B, 000 (1986).

88 P.E.Walters, W.H.Gunter and P.B.Zeeman, Spectrochim. Acta 41B, 133 (1986).

89 C.R.Vidal, J.Q.S.R.T. 6, 575 (1966).

90 C.R.Vidal, J.Q.S.R.T. 6, 461 (1966).

91 H.R.Griem, "Plasma Spectroscopy." McGraw-Hill, New York (1964).

92 H.R.Griem, "Spectral Line Broadening By Plasmas." Academic Press, New York (1974).

93 H.R.Griem, M.Baranger, A.C.Kolb and G.K.Oertel, Phys. Rev. 125, 177 (1962).

94 H.R.Griem, Phys. Rev. 128, 515 (1962).

95 W.L.Wiese, Line Broadening. In "Plasma Diagnostic Techniques" (R.H.Huddlestone and S.L.Leonard, eds.), p.265. Academic Press, New York (1965).

96 B.L.Caughlin and M.W.Blades, Spectrochim. Acta 40B, 987 (1985).

97 H.R.Griem, A.C.Kolb and K.Y.Shen, Phys. Rev. 116, 4 (1959).

98 P.Kepple and H.R.Griem, Phys. Rev. 173, 317 (1968).

99 C.R.Vidal, J.Cooper and E.W.Smith, J.Q.S.R.T. 11, 263 (1971).

100 M.Baranger, Spectral Line Broadening in Plasmas. In "Atomic and Molecular Processes" (D.R.Bates, ed.), Academic Press, New York (1962).

101 J.T.Davies and J.M.Vaughan, Astrophys. J. 137, 1302 (1963).

102 W.L.Wiese, D.E.Kelleher and D.R.Paquette, Phys. Rev. A 6, 1132 (1972).

103 C.R.Vidal, J.Cooper and E.W.Smith, Astrophys. J. Suppl. Series 25, 37 (1973).

104 M.W.Blades and G.Horlick, Spectrochim. Acta 36B, 881 (1981).

105 F.Aeschbach, Spectrochim. Acta 37B, 987 (1982).

106 W.K.Gunter, K.Visser and P.B.Zeeman, Spectrochim. Acta 37B, 571 (1982).

107 L.M.Faires, C.T.Apel and T.M.Niemczyk, Appl. Spectrosc. 36, 558 (1983).

108 J.P.Rybarczyk, C.P.Jester, D.A.Yates and S.R.Koirtyohann, Anal. Chem. 54, 2162 (1982).

109 L.J.Prell, C.Monning, R.E.Harris and S.R.Koirtyohann, Spectrochim. Acta 40B, 1401 (1985).

110 B.Capelle, J.M.Mermet and J.Robin, Appl. Spectrosc. 36, 102 (1982).

111 H.R.Griem, Phys. Rev. 128, 997 (1962).

112 L.DeGalan, R.Smith and J.D.Winefordner, Spectrochim. Acta 23B, 521 (1968).

113 M.Huang and G.M.Hieftje, Spectrochim. Acta 40B, 1387 (1985).

114 T.L.Eddy, J.Q.S.R.T. 33, 197 (1985).

115 K.P.Nick, J.Richter and V.Helbig, J.Q.S.R.T. 32, 1 (1984).

116 H.Kafrouni, Physica 98C, 100 (1979).

117 W.L.Wiese and G.A.Martin, "Wavelengths and Transition Probabilities for Atoms and Atomic Ions." Part II, NSRDS-NBS 68, Washington (1980).

118 M.W.Blades and G.Horlick, Spectrochim. Acta 36B, 861 (1981).

119 P.W.J.M.Boumans, ICP Information Newsletter 4, 89 (1978).

120 H.Yasuda and T.Sekiguchi, Jpn. J. Appl. Phys. 18, 2245 (1979).

121 G.Horlick, S.H.Tan, M.A.Vaughan and C.A.Rose, Spectrochim. Acta 40B, 1555 (1985).

122 J.A.Olivares and R.S.Houk, Anal. Chem. 58, 20 (1986).

123 A.L.Gray, Spectrochim. Acta 40B, 1525 (1985).

124 R.S.Houk and J.A.Olivares, Spectrochim. Acta 39B, 575 (1984).

125 A.L.Gray and A.R.Date, Analyst 108, 1033 (1983).

126 A.R.Date and A.L.Gray, Analyst 108, 159 (1983).

127 D.J.Douglas, E.S.K.Quan and G.Smith, Spectrochim. Acta 38B, 39 (1983).

128 A.R.Date and A.L.Gray, Spectrochim. Acta. 38B, 29 (1983).

129 X.Huang, K.S.Yeah and J.D.Winefordner, Spectrochim. Acta 40B, 1379 (1985).

130 D.E.Nixon, V.A.Fassel and R.N.Kniseley, Anal. Chem. 46, 210 (1974).

131 A.M.Gunn, D.L.Millard and G.F.Kirkbright, Analyst 103, 1066 (1978).

132 A.Aziz, J.A.C.Broekaert and F.Leis, Spectrochim. Acta 37B, 369 (1982).

133 H.Matusiewicz, and R.M.Barnes, Spectrochim. Acta 40B, 29 (1985).

134 K.C.Ng and J.A.Caruso, Appl. Spectrosc. 39, 719 (1985).

135 M.Abdullah, K.Fuwa and H.Haraguchi, Spectrochim. Acta 39B, 1129 (1984).

136 E.D.Salin and G.Horlick, Anal. Chem. 51, 2284 (1979).

137 T.Nakahara, Prog. Anal. Atom. Spect. 6, 163 (1983).

138 M.H.Hahn, K.A.Wolnik, F.L.Fricke and J.A.Caruso, Anal. Chem. 54, 1048 (1982).

139 T.Nakahara and N.Kikui, Spectrochim. Acta 40B, 21 (1985).

140 M.Thompson, J.E.Goulter and F.Sieper, Analyst 106, 32 (1981).

141 J.W.Carr and G.Horlick, Spectrochim. Acta 37B, 1 (1982).

142 T.Ishizuka and Y.Uwamino, Spectrochim. Acta 38B, 519 (1983).

143 H.G.C.Human, R.H.Scott, A.R.Oakes and C.D.West, The Analyst 101, 265 (1976).

144 R.H.Scott, Spectrochim. Acta 33B, 123 (1978).

145 A.Aziz, J.A.C.Broekaert, K.Laqua and F.Leis, Spectrochim. Acta 39B, 1091 (1984).

146 R.F.Browner and A.W.Boorn, Anal. Chem. 56, 786A (1984).

147 P.W.J.M.Boumans and M.Chu.Lux-Steiner, Spectrochim. Acta 37B, 97 (1982).

148 A.W.Boorn and R.F.Browner, Anal. Chem. 54, 1402 (1982).

149 F.J.M.J.Maessen, G.Kreunling and J.Balke, Spectrochim. Acta 41B, 3 (1986).

150 Y.Q.Tang and C.Trassy, Spectrochim. Acta 41B, 143 (1986).

151 S.E.Long, R.D.Snook and R.F.Browner, Spectrochim. Acta 40B, 553 (1985).

152 G.Horlick, 1986 Winter Conference on Plasma Spectrochemistry, Kailua-Kona, Paper No. 106 (1986).

153 P.W.J.M.Boumans, "Line Coincidence Tables for Inductively Coupled Plasma Atomic Emission Spectrometry." Pergamon Press, Oxford (1980).

154 P.W.J.M.Boumans,"Line Coincidence Tables for Inductively Coupled Plasma Atomic Emission Spectrometry." 2nd revised edn. Pergamon Press, Oxford (1984).

155 R.K.Winge, V.A.Fassel, V.J.Peterson and M.A.Floyd, Appl. Spectrosc. 36, 210 (1982).

156 R.K.Winge, V.A.Fassel, V.J.Peterson and M.A.Floyd, "Inductively Coupled Plasma Atomic Emission Spectroscopy. An Atlas of Spectral Information." Elsevier, Amsterdam (1984).

157 L.L.Burton and M.W.Blades, Spectrochim. Acta 41B, 000 (1986).

158 J.W.Brault and L.M.Faires, 1986 Winter Conference on Plasma Spectrochemistry, Kailua-Kona, Paper No. 147 (1986).